

**A POSSIBLE OBSERVATION OF Λ NN CONTINUUM STRUCTURES
AND A BOUND Σ NN STATE USING THE $(e, e' K^+)$ REACTION**

A Dissertation

by

BISHNU DATT PANDEY

Submitted to the Graduate College of Hampton University in
partial fulfillment of the requirements for the degree of

DOCTOR OF PHILOSOPHY

May 2021

This dissertation submitted by Bishnu Datt Pandey in partial fulfillment of the requirements for the degree of Doctor of Philosophy at Hampton University, Hampton, Virginia is hereby approved by the committee under whom the work has been completed.

Liguang Tang, Ph.D.
Committee Chair

José L. Goity, Ph.D.

Michael Kohl, Ph.D.

Joerg Reinhold, Ph.D.

Michelle Penn-Marshall, Ph.D.
Dean, The Graduate College

Date

Copyright by
BISHNU DATT PANDEY
2021

ABSTRACT

A Possible Observation of Λ n Continuum Structures and a Bound Σ NN State

Using the $(e, e'K^+)$ Reaction

(May 2021)

Bishnu Datt Pandey, M.S., Tribhuvan University, Kathmandu, Nepal;

Ph.D. Hampton University

Chair of Advisory Committee: Dr. Liguang Tang

The E12-17-003 ($e, e'K^+$) experiment was carried out in the experimental Hall A facility of Jefferson Lab in November 2018. The experiment aimed at providing the experimental data for the unknown Λ n interaction by measuring the bound state or the resonance state as indicated by the HypHI experiment. The so obtained Λ n interaction was assumed to solve the existing charge symmetry breaking problem in the case of Λ N interaction.

The experiment used Hall A high resolution spectrometers (both left and right spectrometers) positioned symmetrically at constant angle 13.2° each. A 25 cm long aluminum cylinder filled with 3H gas was used as a production target. The major calibration data were taken with the H target contained in an identical aluminum cylinder. The electroproduction of Λ and Σ^0 via $p(e, e'K^+)\Lambda, \Sigma^0$ reactions was used to calibrate the absolute energy scale with the known masses of the Λ and Σ^0 . Then by using the $(e, e'K^+)$ reaction, two possible Λ n resonance states and one Σ NN bound state were observed. The observed states have the energy resolution about 1.6 MeV (FWHM), however, greater statistics are required to solidly confirm the observed states. The $A = 3$ and 4 Σ bound states have been predicted long ago but only the $A = 4$ Σ hypernucleus, that is ${}^4_\Sigma\text{He}$, was found in the (K^-, π^-) reaction.

A careful Monte Carlo study was conducted to study the A (nuclear mass number) dependence on the missing mass resolution by using the identical experimental conditions. The simulated and experimentally obtained Λ and Σ^0 channels agreed within 100 keV in σ , where σ is the standard deviation. The intrinsic missing mass resolution of $A = 3$ ($^3_\Lambda n$) resonance was predicted about $\sigma = 0.67$ MeV with a natural width of about 0.6 MeV. However, due to the low statistics the precision does not permit sufficient constrain on the determination of the Λn interaction. The reason of having such low statistics is due to the use of unoptimized Hall A system which was definitely feasible but not ideal for this experiment. In addition, the cross section was found to be much smaller than expected.

Dedicated to my parents, my wife and my sons Siddartha and Sarwin.

ACKNOWLEDGEMENTS

There are large number of individuals who played a significant role in completing this step of my life. First of all, I would like to express my deepest gratitude to my advisor Prof. Liguang Tang for providing me an opportunity to work under his excellent supervision. I really appreciate him for the support, guidance and encouragement over the past 6 years. During my graduate studies, he allow me to attend various seminars and workshops to extend my physics knowledge. I also got the opportunity to work on a hardware project, which is not part of this thesis, but it gave me good hardware experience. I would like to thank the Hampton University, Physics Department for helping me throughout the journey. I would like to acknowledge my thesis committee, Prof. Jose Goity, Prof. Michael Kohl and Prof. Joerg Reinhold for their valuable guidance.

Beside my supervisor, I got supervision from Dr. Toshiyuki Gogami. I am immensely grateful to him for guiding me through various analyses as well as the simulation projects. Without his help, I couldn't have been able to complete the whole analysis in the short period of time. His knowledge, encouragement and patience are extensive and I feel lucky to work with him closely. I also would like to thank his students, especially, Kazuki Suzuki for the Geant4 simulation.

I couldn't stop myself from thanking the Tohoku University group, namely, Prof. Satoshi N Nakamura, Dr. Sho Nagao, Dr. Masishi Kaneta, Kosuke Itabashi, Yuichi Toyama and Keita Ushera for providing continuous support through their constructive discussions. I would like to thank the whole hypernuclear collaboration for the frequent discussions and comments.

The E12-17-003 was the last experiment in the tritium run group experiments. A lot of students and post docs had significantly contributed during the preparation of the experimental hall. I really like to thank the whole tritium family, especially,

Douglas, Florian, Evan, Marco, Zhihong, Nathaly, Tyler K., Tyler H., Johnathan, Rey, Tong, Hanjie, Shujie, Mike, Jason, Dien, Jesicca, Scott and Sheren. I must thank the MCC group for delivering the nice beam during the whole run period and the JLab target group especially Dave Meekins for his unforgettable contributions. I am also thankful to Ole Hansen and Alex Camsonne for their effort for taking care of the DAQ and the analysis software.

I cannot forget to thank all the nice people around me, mentioning, Thir Gautam, Shankar Adhikari, Bishnu Karki, Carlos Yero, Hem Bhatt, Deepak Bhetuwal, Devilal Adhikari, Nathaniel Lashley-Colthirst and Abhishek Karki for their help and continuous encouragement.

I am very grateful to my parents for supporting and encouraging me to pursue my professional goals in the United States. Finally, I wish to express my deepest gratitude to my better half, Jyoti Bhandari Pandey for her love, care and support. Her continuous encouragement and motivation played a vital role in achieving my goal.

TABLE OF CONTENTS

| Chapter | Page |
|--|------|
| ABSTRACT | iv |
| DEDICATION | vi |
| ACKNOWLEDGEMENTS | vii |
| TABLE OF CONTENTS | ix |
| LIST OF TABLES | xiv |
| LIST OF FIGURES | xvi |
| 1 INTRODUCTION | 1 |
| 1.1 Hyperons and Hypernuclei | 1 |
| 1.2 Historical Overview of Hypernuclear Physics | 4 |
| 1.3 Production of Λ Hypernuclei | 4 |
| 1.3.1 The (K^-, π^-) Reaction | 5 |
| 1.3.2 The (π^+, K^+) Reaction | 7 |
| 1.3.3 The $(e, e'K^+)$ Reaction | 8 |
| 1.4 Weak Decay of Λ Hypernuclei | 10 |
| 1.5 Elementary Process of the $(e, e'K^+)$ Reactions | 11 |
| 1.6 Hyperon (Y) Nucleon (N) Interaction | 13 |
| 1.7 The Purpose of the Present Study | 14 |
| 1.7.1 Physics Motivation | 14 |
| 1.7.2 Charge Symmetry Breaking | 15 |
| 1.7.3 Approach to ΛN Interaction | 16 |

| Chapter | Page |
|--|-----------|
| 1.7.4 Theoretical Investigation on the Ann Resonance | 17 |
| 1.7.5 Available System for the E12-17-003 Experiment | 18 |
| 2 The E12-17-003 Apparatus | 20 |
| 2.1 Overview | 20 |
| 2.2 CEBAF | 21 |
| 2.3 Hall A Overview | 22 |
| 2.4 Kinematic Setting | 23 |
| 2.5 Hall A Beam Line Instrumentation | 24 |
| 2.5.1 Hall A Arc Energy Measurement | 25 |
| 2.5.2 Beam Energy Stability | 27 |
| Fast Feedback System | 27 |
| Synchrotron Light Interferometer | 28 |
| 2.5.3 Beam Current Monitor | 28 |
| 2.5.4 Raster | 30 |
| 2.5.5 Beam Position Monitor | 31 |
| 2.6 Target System | 32 |
| 2.6.1 Overview | 32 |
| 2.6.2 Target Cell Design | 33 |
| 2.6.3 Tritium Target Safety System | 34 |
| 2.6.4 Target Scattering Chamber | 35 |
| 2.7 Sieve Slit and Collimator | 37 |
| 2.8 Hall A High Resolution Spectrometer System | 38 |
| 2.8.1 Overview | 38 |
| 2.8.2 HRS Design and Characteristics | 39 |
| 2.9 HRS Detector Package | 41 |

| Chapter | Page |
|--|-----------|
| 2.9.1 Overview | 41 |
| 2.9.2 Vertical Drift Chambers | 41 |
| 2.9.3 Scintillation Detectors | 44 |
| 2.9.4 Gas Cherenkov Detector | 46 |
| 2.9.5 Aerogel Cherenkov Detector | 48 |
| 2.9.6 Calorimeters | 50 |
| 2.10 Data Acquisition System | 51 |
| 2.11 Triggers | 52 |
| 3 Data Analysis and System Optimization | 55 |
| 3.1 Data Collected | 55 |
| 3.2 Data Analysis Overview | 55 |
| 3.3 Coordinate System | 57 |
| 3.3.1 Hall Coordinate System | 57 |
| 3.3.2 Target Coordinate System | 57 |
| 3.3.3 Detector Coordinate System | 59 |
| 3.3.4 Transport Coordinate System | 59 |
| 3.3.5 Focal Plane Coordinate System | 59 |
| 3.4 K^+ Identification | 61 |
| 3.5 Electron Identification | 63 |
| 3.6 Coincidence Time | 64 |
| 3.7 Background Source | 66 |
| 3.8 The Cuts Related to the Z -Vertex | 68 |
| Cuts Used for the Z -Vertex Optimization | 68 |
| Average Z -Vertex Cut | 68 |
| The Z -Vertex Correlation Cut | 69 |

| Chapter | Page |
|---|------------|
| | 69 |
| | 70 |
| Aluminum Gate Cuts | 69 |
| Cuts for Estimation of the Accidental Background | 70 |
| 3.9 System Optimization | 71 |
| 3.9.1 Overview | 71 |
| 3.9.2 BCM Calibration | 71 |
| 3.9.3 BPM Calibration | 71 |
| 3.9.4 Raster Calibration | 71 |
| 3.9.5 <i>Z</i> -Vertex Optimization | 73 |
| Backward Transfer Matrix | 73 |
| Backward Transfer Matrix Optimization | 73 |
| <i>Z</i> -Vertex with the Optimized Matrix | 75 |
| 3.9.6 Transformation Matrices for HRS Angle and Momentum | 76 |
| 3.9.7 HRS Angle Optimization | 77 |
| 3.9.8 Missing Mass | 79 |
| 3.9.9 Energy Loss Correction | 82 |
| 3.9.10 Kinematic Space for the ($e, e'K^+$) Experiment | 86 |
| 3.9.11 Momentum Optimizations | 88 |
| 3.9.12 Time Jitter Correction | 89 |
| 3.9.13 Dependence on the Residual Angular Uncertainties | 90 |
| 3.9.14 Monte Carlo Simulation for Missing Mass Resolution | 92 |
| 3.9.15 Al Data Involved in the Matrix Optimization | 97 |
| 4 Result and Discussion | 104 |
| 4.1 Reconstructed Λ and Σ^0 Missing Masses | 104 |
| 4.2 Systematic Uncertainty | 105 |
| 4.3 H Contamination | 106 |

| Chapter | Page |
|--|------------|
| 4.4 Mass Spectroscopy Obtained from the T Target | 108 |
| Accidental Background Analysis | 110 |
| 4.5 Possible Observation of the Ann Continuum Structures (Resonances) | 111 |
| 4.6 Possible Observation of a Bound ΣNN Hypernuclear State | 113 |
| 4.7 Statistical Significance | 115 |
| 4.8 Cross Section | 116 |
| 5 Summary and Conclusion | 120 |
| 5.1 Future Suggestions | 121 |
| REFERENCES | 124 |
| VITA | 130 |

LIST OF TABLES

| Table | Page |
|--|------|
| 1.1 Basic characteristics of hyperons [1]. Here, I is the isospin and J^P is the spin parity. | 2 |
| 1.2 The basic characteristics of (K^-, π^-) , (π^+, K^+) , and $(e, e' K^+)$ reactions. | 10 |
| 2.1 The basic kinematics used for the E12-17-003 experiment. | 23 |
| 2.2 The list of targets used in the E12-17-003 experiment. | 33 |
| 2.3 The main characteristics of the A1 and A2 detectors with their threshold momentum. | 49 |
| 2.4 The A1 and A2 detector response when hadrons pass through them. Here, 1 means fired and 0 means not fired. | 49 |
| 2.5 Summary of E12-17-003 triggers. The symbol “&” represents the logical “AND” gate. | 54 |
| 3.1 The MPV values for the different window thicknesses for the beam electron. | 83 |
| 3.2 The Δp parameters for different cell thicknesses for the K^+ s momentum loss correction. | 85 |
| 3.3 The Δp parameters for different cell thicknesses for the e' s momentum loss correction. | 85 |
| 3.4 The details about the uncertainties used in the Monte Carlo simulation. | 96 |
| 3.5 The comparison between the experiment and simulation. | 98 |
| 4.1 Summary of the obtained masses of Λ and Σ^0 , and their separation in comparison to the values from Ref. [1]. | 105 |
| 4.2 The statistical significance for all three observed peaks within the region of $\pm 2.5\sigma$ from the mean. | 116 |

| Table | Page |
|--|------|
| 4.3 The cross section for the observed peaks. The uncertainty include the systematic and statistical uncertainty. | 119 |

LIST OF FIGURES

| Figure | Page |
|--|------|
| 1.1 Combinations of three u , d , and s quarks form (a) baryon octet with spin $1/2$ particles and (b) baryon decuplet with $S(\text{spin}) = 3/2$ particles. | 1 |
| 1.2 Experimentally studied Λ hypernuclei chart. Figure is taken from [2]. | 3 |
| 1.3 Schematic of hypernuclear production via (K^-, π^-) (left) and (π^+, K^+) (right) reaction. | 6 |
| 1.4 Hyperon recoil momentum as a function of projectile momentum. | 7 |
| 1.5 Schematic of hypernuclear production via $(e, e'K^+)$ reaction. | 9 |
| 1.6 One-pion exchange, one-kaon exchange, and contact contributions to the transition. The solid circle represents the weak interaction vertex. | 11 |
| 1.7 Schematic drawing for the kinematics of the $(e, e'K^+)$ reaction. | 12 |
| 1.8 Two-pion-exchane and one kaon exchahnge in the ΛN interaction. | 14 |
| 1.9 Schematic illustration of mirror pair of $A = 3$ nuclei (a) and $A = 4$ isospin mirror pair of Λ hypernuclei (b). A significant CSB can be seen in case of ΛN interaction with an unknown origin. | 16 |
| 1.10 Result of the HypHI [3] experiment at GSI. (a1) and (a2) represent the invariant mass distributions from the $d + \pi^-$ decay and (b1) and (b2) represent the same from $t + \pi^-$ decay. | 17 |
| 1.11 The complex energy eigenvalue spectrum. Four different trajectories of the resonance pole with the Λn interaction. These curves were obtained using four different theoretical models (Mod D, Chiral, NSC97f, and Julich04). Each model fitted the effective range parameters of nn and Λp interactions from the existing data. | 19 |
| 2.1 Schematic view of the experimental Hall A showing two high resolution spectrometers. | 22 |

| Figure | Page |
|--|------|
| 2.2 Production of hypernuclei via the $(e, e'K^+)$ reaction. | 24 |
| 2.3 A schematic layout of the beam line components [4]. | 25 |
| 2.4 Schematic for the Hall A arc energy measurement. | 26 |
| 2.5 Schematic of the Hall A beam current measurement. | 30 |
| 2.6 Rastered beam y vs beam x. | 31 |
| 2.7 Schematic of the Hall A BPMs and harps. | 32 |
| 2.8 Schematic of the gas cell design (left). Side view of the cell where the bright green region represents the gas volume (right). | 34 |
| 2.9 (Left) Schematic of the target ladder with the yellow mark shows the gas targets, the red mark shows the carbon multi-foil target, and blue mark shows other solid targets. (Right) Front view of solid targets [5]. | 36 |
| 2.10 Schematic of the SS plate installed in one of the spectrometers. . . | 38 |
| 2.11 Schematic of the Hall A HRS system illustrating the beam electron, LHRS, and RHRS with the corresponding detector huts. | 39 |
| 2.12 Schematic of the Hall A HRS system showing the magnetic particle transport system. | 40 |
| 2.13 Schematic of a complete detector package for the E12-17-003 experiment. | 42 |
| 2.14 Schematic layout of a pair of VDCs used in the Hall A HRS detector package. | 43 |
| 2.15 Schematic of a typical nominal track in the wire planes. | 44 |
| 2.16 Schematic of the two scintillator planes S0 and S2 [6]. | 45 |
| 2.17 Top view of the two Aerogel detectors A1 and A2 in the detector stack. | 48 |
| 2.18 Schematic of the calorimeters for LHRS (left) and RHRS (right) [7]. | 50 |
| 2.19 Schematic of the single arm (LHRS) trigger setup [8]. | 53 |
| 3.1 Schematic of the flow chart of the E12-17-003 data analysis. . . . | 56 |

| Figure | Page |
|--|------|
| 3.2 Schematic of the Hall Coordinate System (top view). | 57 |
| 3.3 Schematic of the Target Coordinate System. L represents the distance from the hall center to the sieve plane. D is the horizontal displacement of the spectrometer axis from the ideal position. | 58 |
| 3.4 Schematic of (a) top view of the Detector Coordinate System and (b) side view of the Detector Coordinate System. | 59 |
| 3.5 Schematic of side view of the Transport Coordinate System. . . . | 60 |
| 3.6 Schematic of the focal plane (rotated) coordinate system. | 60 |
| 3.7 Schematic of the Aerogel A1 ADC sum (left) and the Aerogel A2 ADC sum (right). | 62 |
| 3.8 Correlation between the coincidence time(ns) and the A2 Aerogel ADC sum. The background is seen because of the inefficiency of the Aerogel detector. | 63 |
| 3.9 The LHRS Gas Cherenkov ADC sum. | 64 |
| 3.10 The coincidence time between LHRS (e') and RHRS (K^+). | 66 |
| 3.11 The correlation between the LHRS z -vertex and RHRS z -vertex. The events along the diagonal line corresponds to the real events from the gas region. | 69 |
| 3.12 The difference between two z -vertexes (z -LHRS and z -RHRS). . . | 70 |
| 3.13 The schematic of the raster current along the horizontal direction. | 72 |
| 3.14 Schematic of flow chart of the backward matrix optimization process. | 74 |
| 3.15 The LHRS optimized z -vertex with the carbon multi-foil target. . | 75 |
| 3.16 Average z -vertex with the H target which was obtained by taking the average of two separately reconstructed z 's from LHRS and RHRS. | 76 |
| 3.17 The LHRS θ and ϕ correlation in terms of the sieve slit hole locations. | 78 |
| 3.18 The RHRS θ and ϕ correlation. Each spot represents a SS hole. . | 79 |
| 3.19 (a) The e' momentum loss vs x' ($= dx/dz$) correlation for the cell thickness of 400 μm . Here, (b) is the projection of the momentum loss. | |

| Figure | Page |
|---|------|
| The upper cluster (or the large peak) corresponds to the region of z -average < 8.0 cm and the lower cluster (or the small peak) corresponds to the region of z -average > 8.0 cm. | 84 |
| 3.20 (a) The e' momentum loss vs x' ($= dx/dz$) correlation with the angular dependence corrected. Here, (b) is the projection of the momentum loss. | 86 |
| 3.21 Illustration of the kinematic space for the $(e, e'K^+)$ experiment. | 87 |
| 3.22 RHRs raw TDC spectrum before the time jitter correction. The blue spectrum represents the RHRs single arm trigger mode and red spectrum represents the coincidence trigger mode. | 90 |
| 3.23 RHRs raw TDC spectrum after the time jitter correction. The blue spectrum represents the RHRs single arm trigger mode and red spectrum represents the coincidence trigger mode. The coincidence time spectrum was scaled up by 2.8 to make the comparison. | 91 |
| 3.24 The correlation between the resolution and nuclear mass number (A) when the beam energy is smeared at different level of uncertainties. | 92 |
| 3.25 The correlation between the resolution and nuclear mass number (A) when the LHRs momentum is smeared at different level of uncertainties. | 93 |
| 3.26 The correlation between the resolution and nuclear mass number (A) when the RHRs momentum is smeared at different level of uncertainties. | 94 |
| 3.27 The correlation between the resolution and nuclear mass number (A) when the e' scattering angle ($\theta_{ee'}$) is smeared at different level of uncertainties. | 95 |
| 3.28 The correlation between the resolution and nuclear mass number (A) when the K^+ reaction angle (θ_{eK^+}) is smeared at different level of uncertainties. | 96 |
| 3.29 The correlation between the resolution and nuclear mass number (A) when the reaction plane angle ($\Delta\phi$) is smeared at different level of uncertainties. | 97 |
| 3.30 The two dimensional correlation between the nuclear mass number (A) and simulated resolution (σ). | 98 |

| Figure | Page |
|---|------|
| 3.31 The $^{27}_{\Lambda}\text{Mg}$ spectrum before the Al data involved in the matrix tune. The events from the beam entrance and beam exit aluminum windows were selected and combined together to produce the $^{27}_{\Lambda}\text{Mg}$ hypernuclei. To calculate the missing mass in terms of binding energy (B_{Λ}), the missing mass of the $^{27}_{\Lambda}\text{Mg}$ is calculated first and then the rest mass of the $^{27}_{\Lambda}\text{Mg}$ is subtracted. The distribution formed by the green crosses represents the accidental background shape. The distribution above the accidental distribution is the quasi-free distribution. | 99 |
| 3.32 The $^{27}_{\Lambda}\text{Mg}$ spectrum after the initial tune. Four structures are appeared in the $^{27}_{\Lambda}\text{Mg}$ hypernuclei. The three at the higher excitation continuum states are much narrower than expected. The four peaks I, II, II and IV are landed at -3.33 MeV, 6.17 MeV, 20.6 MeV, and 30.8 MeV, respectively. The distribution formed by the green crosses represents the accidental background distribution. | 101 |
| 3.33 $^{27}_{\Lambda}\text{Mg}$ spectrum after involving the Al data in the matrix tune. The missing mass of $^{27}_{\Lambda}\text{Mg}$ is calculate in terms if binding energy. To calculate the binding energy, the missing mass of $^{27}_{\Lambda}\text{Mg}$ is calculated first and then the rest mass of the $^{27}_{\Lambda}\text{Mg}$ is subtracted. Here, I and II are the two peak structures obtained after the momentum optimization. The mean of the peak I and II are landed at - 3.84 MeV and 30.2 MeV, respectively. The distribution formed by the green crosses represents the accidental background shape. The distribution above the accidental background distribution is the quasi-free distribution. | 102 |
| 3.34 To make a clear observation of the observed states, the $^{27}_{\Lambda}\text{Mg}$ is plotted with reduced x-axis plotting range. The missing mass is calculated in terms of binding energy. To calculate the binding energy, the missing mass of $^{27}_{\Lambda}\text{Mg}$ calculated and then the rest ass of the $^{27}_{\Lambda}\text{Mg}$ is subtracted from the calculated missing mass. | 103 |
| 4.1 The missing mass spectroscopy of the free Λ and Σ^0 obtained by analyzing the H data in the H kinematics. | 104 |
| 4.2 The missing mass spectroscopy of the free Λ obtained by analyzing the H data in the T kinematics. | 105 |
| 4.3 Tritium data is analyzed with H kinematics. To calculate the missing mass in terms of binding energy, the missing mass is calculated first by considering the proton as target instead of tritium and then the Λ mass is subtracted from the calculated missing mass. The distribution formed by the green crosses represents the accidental background shape. | |

| Figure | Page |
|---|------|
| The distribution above the accidental background distribution is the tritium quasi-free distribution under the wrong kinematics. Because of the wrong target mass, the quasi-free has a broad distribution. The clear peak on the top of the quasi-free distribution (at $B_\Lambda = 0$ MeV) shows the presence of H in the tritium gas. The blue-dashed Gaussian curve gives the free Λ from hydrogen contamination. | 107 |
| 4.4 The binding energy spectrum obtained by analyzing the H/T data by considering the tritium as target mass and Ann as a recoil mass. To calculate the binding energy, the missing mass is calculated by considering the tritium as target instead of H and then the rest mass of the Ann system is subtracted. Because of the wrong target mass, the spectrum is broadened by about 5 times. | 108 |
| 4.5 The mass spectroscopy of $^3_\Lambda n$ hypernuclei in terms of binding energy after involving the aluminum data in the matrix tune. The distribution formed by the green crosses represents the accidental background shape. The red curves gives the simulated Λ and Σ quasi-free distributions and blue-dotted curve is the free Λ from H contamination (kinematically broadened). For the first peak (I) the χ^2/NDF is 0.83 and for the second peak (II) it is 0.99. | 109 |
| 4.6 The accidental background distribution fitted with a 6 th order polynomial. To minimize the statistical fluctuation in the accidental background shape, the events were selected from 38 small accidental peaks from the coincidence time spectrum (see Fig. 3.10) and then the obtained missing mass distribution was scaled down by 38. | 111 |
| 4.7 The mass spectroscopy of $^3_\Lambda n$ hypernuclei plotted with a larger bin size (2.5 MeV/bin) in terms of binding energy B_Λ . The spectrum is plotted with the system optimized with involving the aluminum data in the matrix tune. The magenta-dotted curve shows the fit for the bound state of ΣNN hypernucleus. The ΣNN peak is fitted over a known QF shape with $\chi^2/NDF = 0.55$ | 114 |

CHAPTER 1

INTRODUCTION

1.1 Hyperons and Hypernuclei

According to the standard model of particle physics, baryons are the composite particles made of three quark valence structure [9]. The common examples of baryons are the proton and the neutron containing the uud and udd quark level configurations, respectively. When at least one quark (either u or d or both) is replaced by a strange quark, the baryon is then called hyperon. Therefore, the hyperons are the baryons composed of at least one strange valence quark. Four hyperon families have been discovered which are Lambda (Λ), Sigma(Σ), Xi (Ξ), and Omega (Ω). Out of these hyperons the Λ is the lightest hyperon having one strange quark with a quark combination of uds . The different combinations of these three quarks (uds) form the flavor $SU(3)$ baryon octet with $S(\text{spin}) = 1/2$ (see Fig. 1.1 (a)) and baryon decuplet with $S(\text{spin}) = 3/2$ (see Fig. 1.1 (b)).

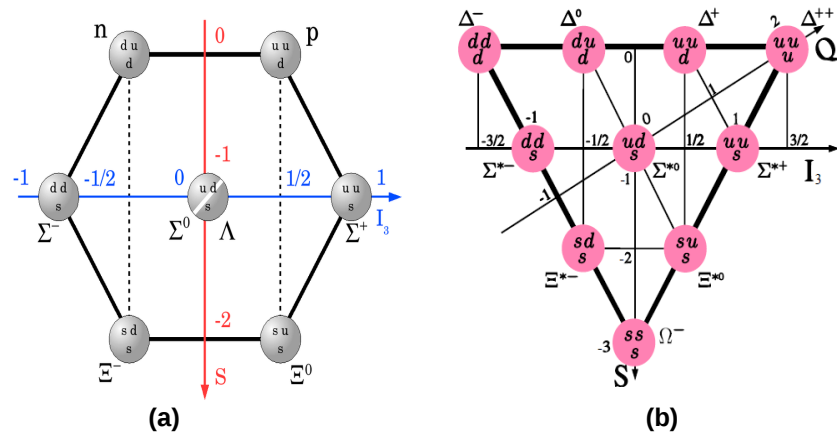


Figure 1.1. Combinations of three u , d , and s quarks form (a) baryon octet with spin $1/2$ particles and (b) baryon decuplet with $S(\text{spin}) = 3/2$ particles.

Among the observed hyperons, most of the experimental observations were made with the Λ hyperon as it has a larger lifetime than the rest of the hyperons [1]. The higher lifetime of Λ hyperon allows it to bind within a nucleons and provide us with a laboratory to explore the ΛN interaction. Some basic characteristics of the hyperons are presented in Table 1.1.

Table 1.1

Basic characteristics of hyperons [1]. Here, I is the isospin and J^P is the spin parity.

| Name | Mass [MeV/c^2] | Quarks | $I(J^P)$ | Lifetime [sec] |
|------------|--------------------|--------|------------------------------|-------------------------|
| Λ | 1115.683 | uds | $0(\frac{1}{2}^+)$ | 2.632×10^{-10} |
| Σ^- | 1197.449 | dds | $1(\frac{1}{2}^+)$ | 1.479×10^{-10} |
| Σ^0 | 1192.642 | uds | $1(\frac{1}{2}^+)$ | 7.4×10^{-20} |
| Σ^+ | 1189.37 | uus | $1(\frac{1}{2}^+)$ | 0.801×10^{-10} |
| Ξ^0 | 1314.83 | uss | $\frac{1}{2}(\frac{1}{2}^+)$ | 2.90×10^{-10} |
| Ξ^- | 1321.31 | dss | $\frac{1}{2}(\frac{1}{2}^+)$ | 1.639×10^{-10} |
| Ω^- | 1672.45 | sss | $0(\frac{3}{2}^+)$ | 0.821×10^{-10} |

In general, a nucleus contains proton(s) and neutron(s) held together by the strong nuclear force of attraction. If at least one of the nucleons in the nucleus is replaced by a hyperon, the nucleus is then called a hypernucleus. Therefore, a hypernucleus is a many body system consisting of nucleons and at least one hyperon. Since the strange quark is involved, hypernuclear physics is also called strangeness nuclear physics. Conventionally, a hypernucleus is represented by ${}^A_Y Z$, where A is the total number of baryons in the nuclear system, Z corresponds to the number of protons and Y is the hyperon.

A hyperon, for example, Λ in a nucleus acts as an impurity changing the nuclear structure such as nuclear size, nuclear shape, cluster structure, nuclear Fermi motion etc. [10, 11] and providing opportunities to study the properties of baryons in the nuclear medium as well as the structure of nuclei as a baryonic many body system. The YN interactions have been studied primarily via measurements of energy levels and transitions of hypernuclei as the lifetime of hypernuclei is very small, about 200 ps [12]. The first hypernuclear event was observed in 1952 by following the interaction of high energy cosmic rays in a stack of photographic emulsion [13]. So far up to now, about 40 species of Λ hypernuclei up to mass number $A = 209$ have been observed. For most of the observed hypernuclei, their masses have been experimentally measured. The experimentally studied hypernuclei are summarized in Fig. 1.2.

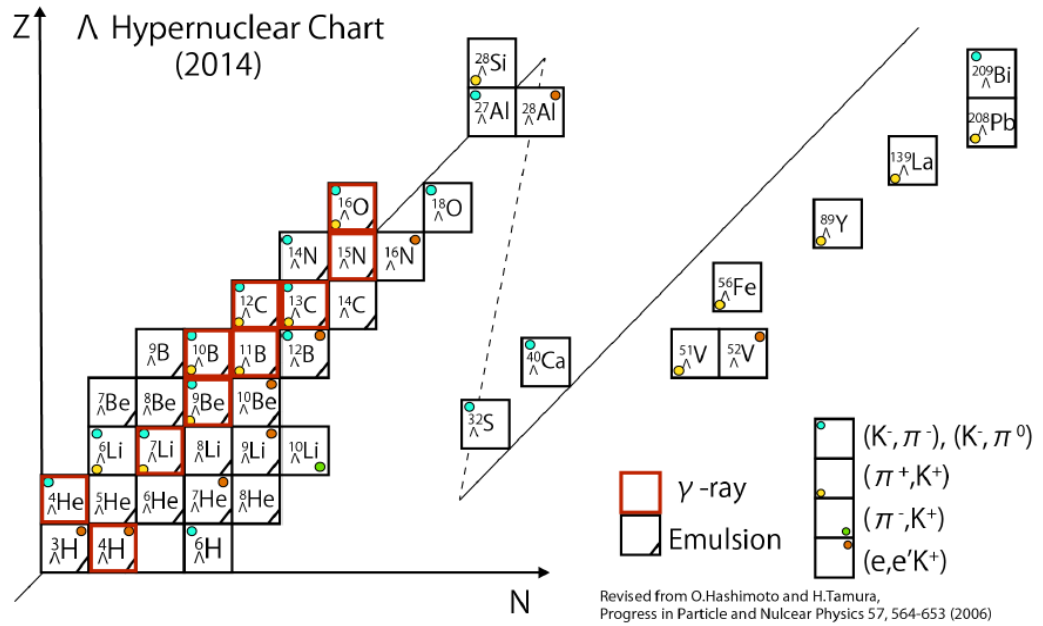


Figure 1.2. Experimentally studied Λ hypernuclei chart. Figure is taken from [2].

1.2 Historical Overview of Hypernuclear Physics

The hypernuclear physics journey started after the first hypernucleus identified in 1952 through the decay in the nuclear emulsion. Up to now a significant contribution has been made to the understanding of hypernuclear physics through various experimental observations. The hypernuclear experiments have evolved through the following four stages [14]:

1. The emulsion and bubble chamber experiments by using the (K^-, π^-) reaction at CERN and AGS (Brookhaven National Laboratory) in the 1960's.
2. The counter experiments by using the (K^-, π^-) reaction at CERN and AGS-BNL from the early 1970's.
3. The counter experiments by using the (π^+, K^+) reaction at AGS-BNL and 12 GeV Proton Synchrotron (PS) of the High Energy Accelerator Organization (KEK, Japan) from the mid 1980's to the 1990's.
4. The counter experiments by using the $(e, e' K^+)$ reaction at Thomas Jefferson National Laboratory Accelerator Facility (JLab) in the 2000's.

Some more details about the Λ hypernuclear production reactions will be discussed in the following section.

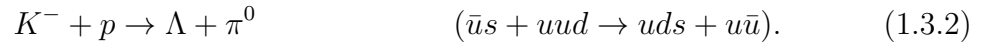
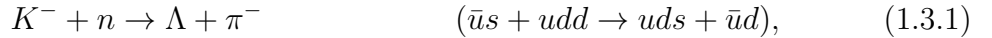
1.3 Production of Λ Hypernuclei

It is obvious that in order to produce a hypernucleus, a hyperon needs to be inserted into a nucleus. Once a hyperon is bound with a nucleus, it has its own potential well and maximum Fermi momentum surface [15]. To bind a hyperon to the nuclear medium, the recoil momentum should be comparable to the Fermi momentum (~ 270 MeV/c). If the recoil momentum is much larger than the threshold momentum

(Fermi momentum), the produced hyperon will have a higher probability of escaping the target nucleus without sticking to it. On the other hand, if the recoil momentum is too small in comparison to the threshold momentum, the produced hyperon will stay at the same orbital as the original nucleon. Besides that, the kinematics also play a significant role which can affect the hypernuclear production. By considering all of these factors, different methods have been developed to study the Λ hypernuclei which are discussed in the coming section.

1.3.1 The (K^-, π^-) Reaction

The production and study of hypernuclei begun with emulsion techniques at CERN and BNL in the 1960's in which the K^- beam was used to produce the Λ hypernucleus. In the (K^-, π^-) reaction the s quark from the projectile meson is transferred to the target nucleon (neutron) converting it into the Λ hyperon according to the following reaction:



The Feynman diagram for the reaction is shown in Fig. 1.3. Some major characteristics of the (K^-, π^-) reaction are as follows:

- The K^- beam was used to produce the Λ hypernuclei.
- A neutron is converted into a Λ .
- The (K^-, π^-) reaction is the strangeness exchange reaction.
- At the early time, the (K_{stop}^-, π^-) reaction was used in which Kaon was not measured. In this reaction, a K^- is absorbed by the target nucleus even at rest as the reaction is exothermic. The reaction was given specific name (K_{stop}^-, π^-) reaction.
- The (K_{stop}^-, π^-) was taken over by in-flight (K^-, π^-) reaction in which recoil of various Λ hypernucleus was almost negligible.

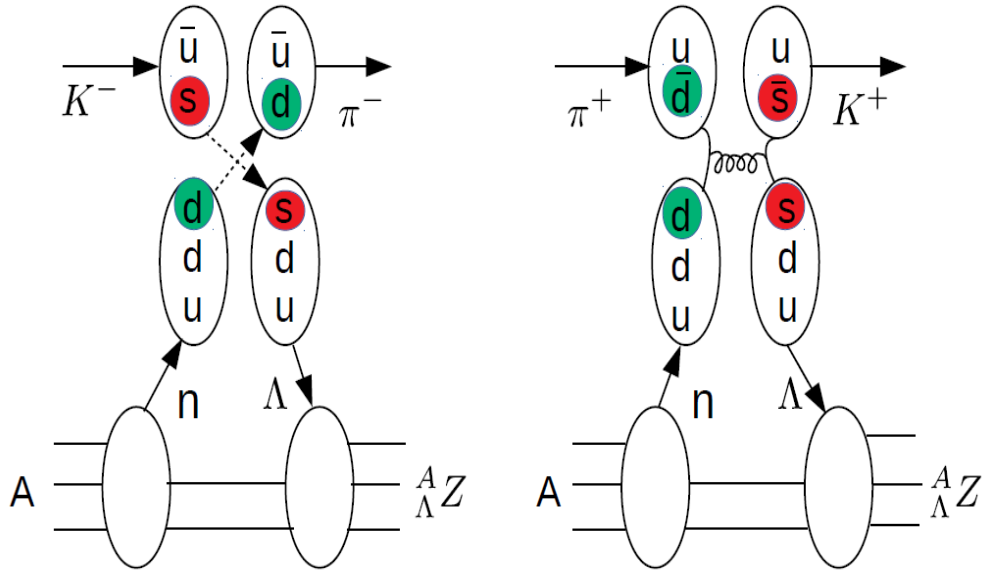


Figure 1.3. Schematic of hypernuclear production via (K^-, π^-) (left) and (π^+, K^+) (right) reaction.

- From the (K^-, π^-) reaction it is difficult to study the deeply bound state of Λ hypernucleus as the kaon reacts with an outer shell nucleon.

Figure 1.4 shows the momentum transfer to Λ by the (K^-, π^-) reaction as a function of beam momentum with three different scattering angles [16]. From the figure it is clear that the Λ recoil momentum depends on the beam momentum and the scattering angles. The larger the beam momentum, the larger the Λ recoil momentum and vice versa. Similarly, the larger the scattering angle, the larger the recoil momentum. The figure depicts that for a beam momentum of about 1200 MeV/c and scattering angle up to 10° , the recoil momentum is less than 250 MeV/c. The incoming K^- has relatively small momentum, most probably it will interact with the outer shell nucleons. Under such condition, the produced hyperon has higher probability of staying in the same orbit as that of the original nucleon resulting in a large cross section. Therefore, the (K^-, π^-) is considered as a powerful tool to study the p shell hypernuclei.

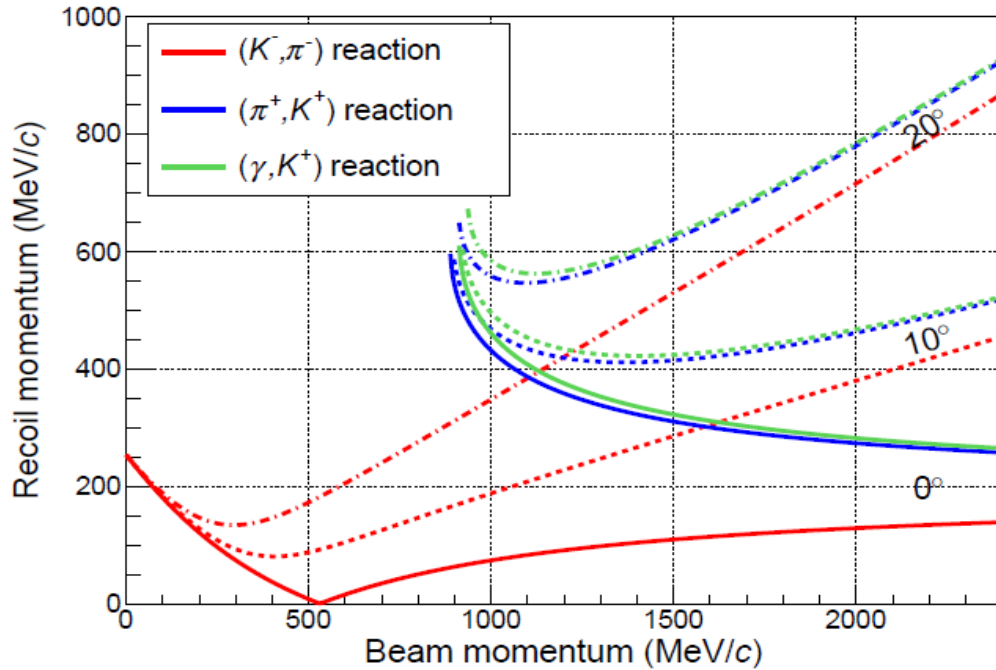
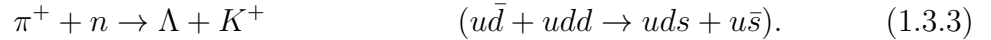


Figure 1.4. Hyperon recoil momentum as a function of projectile momentum.

1.3.2 The (π^+, K^+) Reaction

Another method, the (π^+, K^+) reaction, was developed in the mid 1980's to study the Λ hypernuclei at AGS-BNL [17] and later at KEK [18, 19]. In this method a π^+ beam was used to produce the Λ hypernuclei. The (π^+, K^+) reaction produces a quark-anti quark ($s\bar{s}$) pair according to the following reaction:



The production mechanism via the (π^+, K^+) reaction is also shown in Fig. 1.3. Some major characteristics of the (π^+, K^+) are as follows:

- A π^+ beam converts a neutron to a Λ particle.
- In the (π^+, K^+) reaction a $(s\bar{s})$ strangeness pair is produced.
- The production cross-section is smaller ($\sim 10 \mu\text{b}/\text{sr}$) in comparison to the (K^-, π^-) reaction, but compensated by higher beam intensity.

- The recoil momentum is larger than that observed in the (K^-, π^-) reaction.
- This method is very successful for studying the deeply bound states with a better resolution about 1.5 to 2 MeV (FWHM).

Figure 1.4 shows the momentum transfer to Λ by the (π^+, K^+) reaction as a function of beam momentum with three different scattering angles. The momentum transfer is larger than that of the (K^-, π^-) reaction, and the hyperon has higher probability to escape the nucleus without sticking it. This results in the small value of cross section for the (π^+, K^+) reaction. To compensate the hypernuclear yield, a higher intensity beam is required. However, the higher momentum transfer allows the Λ to make an orbital transition to a lower level. Therefore, this reaction can explore the deeply bound hypernuclear states.

1.3.3 The $(e, e' K^+)$ Reaction

The study of hypernuclei by means of missing mass spectroscopy using the $(e, e' K^+)$ reaction started in the year 2000 at Thomas Jefferson National Accelerator facility (JLab) [20, 21]. A high quality electron beam was used to create the quark-antiquark ($s\bar{s}$) pair via the electromagnetic reaction,

$$e + p \rightarrow e' + \Lambda + K^+. \quad (1.3.4)$$

This is a two step process. In the first step a virtual photon is emitted [22] as the electron scatters from a target proton. Then the virtual photon interacts with the proton according to the reaction given by Eq. 1.3.4 [23] and resulting in a Λ particle along with a K^+ ,

$$\gamma + p \rightarrow \Lambda + K^+ \quad (udd \rightarrow uds + u\bar{s}). \quad (1.3.5)$$

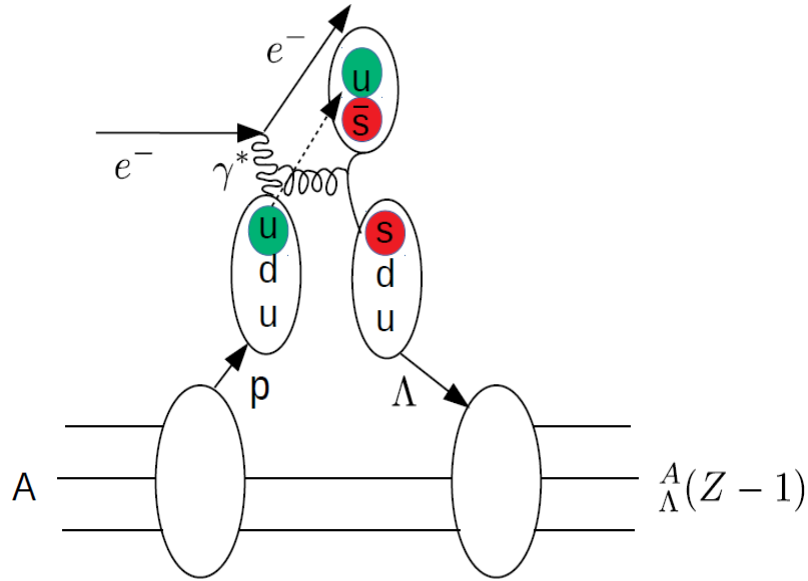


Figure 1.5. Schematic of hypernuclear production via $(e, e' K^+)$ reaction.

The hypernuclear production mechanism via the $(e, e' K^+)$ reaction is shown in Fig. 1.5. The main characteristics of the $(e, e' K^+)$ reaction are as follows:

- Electron beam is used to produce the hypernuclei by producing the $(s\bar{s})$ pair.
- A proton is converted into Λ producing neutron rich hypernuclei. The produced hyperon has large recoil momentum producing the deeply bound hypernuclei.
- The electron beam allow to use the thinner target which minimizes the energy straggling of particles in the target, thus resulting in improved energy resolution.
- In the $(e, e' K^+)$ experiments an absolute energy scale is calibrated by using the Λ and Σ^0 events from the target (H nucleus) and making possible to achieve a sub MeV (FWHM) energy resolution.
- The hypernuclear formation cross-section is much smaller than those of (K^-, π^-) and (π^+, K^+) reactions but compensated by a much higher beam intensity.
- Because of the electron beam there is probability of having high background, however, it can be minimized by considering the experimental design such as tilt method [24, 25] and using the high quality of particle identification detectors.
- The $(e, e' K^+)$ reaction produces a Λ from a proton in the target nucleus resulting in Λ hypernuclei. The produced hypernuclei have mirror states to those produced by the hadronic reactions. For instance, in case of the ^{12}C target, $^{12}_\Lambda B$ and $^{12}_\Lambda C$ are produced from the $(e, e' K^+)$ reaction and (K^-, π^-) , (π^+, K^+) reactions, respectively.

The main characteristics of all three reactions (K^-, π^-), (π^+, K^+), and ($e, e'K^+$) are summarized in Table 1.2.

Table 1.2

The basic characteristics of (K^-, π^-), (π^+, K^+), and ($e, e'K^+$) reactions.

| Reaction | Reaction type | Cross section [$\mu b/sr$] | Incident energy [GeV/c] | Recoil momentum [MeV/c] |
|----------------------------|----------------|------------------------------|-------------------------|-------------------------|
| in-flight (K^-, π^-) | n to Λ | 10^3 | 0.8 | $a < 100$ |
| stopped (K^-, π^-) | n to Λ | 10^2 | 0 | $q = 250$ |
| (π^+, K^+) | n to Λ | 10 | 1.0 | $q > 300$ |
| ($e, e'K^+$) | p to Λ | 10^{-1} | > 1.5 | $q > 300$ |

1.4 Weak Decay of Λ Hypernuclei

The life time of Λ hypernuclei is about 190 ps [3] which is much smaller than that of free Λ particle (~ 260 ps). The hyperons decay weakly with a mean free path $\approx c\tau = O(10cm)$ [26]. A free Λ particle dominantly decays through the mesonic weak decay (MWD) mode as:

$$\Lambda \rightarrow N + \pi \quad (p_N \sim 100 \text{ MeV}/c). \quad (1.4.1)$$

In this mode, Λ decays to give proton and π^- with a probability of $\sim 60\%$ and it decays to give a neutron and π^0 with a probability of $\sim 40\%$. However, the MWD is strongly suppressed by Pauli principle when the hyperon is bound in the nucleus because the momentum of out going nucleon is (~ 100 MeV/c) smaller than the Fermi momentum in the nucleus (~ 270 MeV/c) [27]. An experiment at GSI used MWD channel to measure an invariant mass of hypernuclei and an indication of the nn Λ bound state was reported in the invariant mass spectroscopy. When the Λ particle is

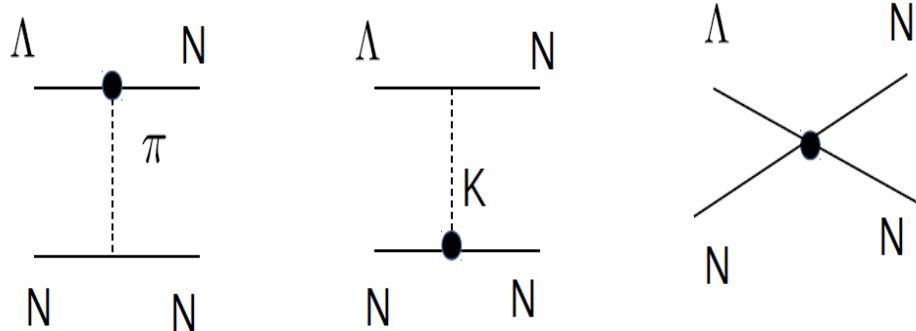


Figure 1.6. One-pion exchange, one-kaon exchange, and contact contributions to the transition. The solid circle represents the weak interaction vertex.

surrounded by one or more nucleons, it decays through non-mesonic decay modes as:

$$\Lambda + N \rightarrow N + N \quad (p_N \sim 420 \text{ MeV}/c), \quad (1.4.2)$$

$$\Lambda + N + N \rightarrow N + N + N \quad (p_N \sim 340 \text{ MeV}/c). \quad (1.4.3)$$

The Feynman diagram of one meson exchange model of non mesonic weak decay is shown in Fig. 1.6 [28].

1.5 Elementary Process of the $(e, e' K^+)$ Reactions

The elementary process of the electroproduction can be described with the help of the following equation:

$$e + p \rightarrow e' + \Lambda + K^+. \quad (1.5.1)$$

The kinematics of the $(e, e' K^+)$ reaction is shown in Fig. 1.7. The complete reaction process takes place in two different planes. The first plane is the electron

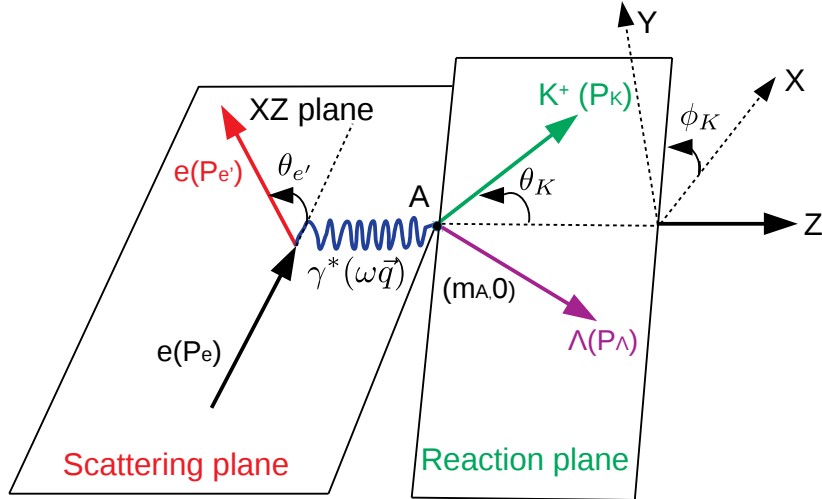


Figure 1.7. Schematic drawing for the kinematics of the $(e, e' K^+)$ reaction.

scattering plane in which the incident electron scattered off a target nucleon with a defined angle $\theta_{e'}$. In this plane the initial and the final electron four momenta are defined as:

$$P_e = (E_e, \vec{p}_e), \quad (1.5.2)$$

$$P_{e'} = (E_{e'}, \vec{p}_{e'}). \quad (1.5.3)$$

During this process a virtual photon (γ^*) is created in the electron scattering plane with a four momentum $Q = (\omega, \vec{q})$. The energy and the momentum of the virtual photon are:

$$\omega = E_e - E_{e'}, \quad (1.5.4)$$

$$\vec{q} = \vec{p}_e - \vec{p}_{e'}. \quad (1.5.5)$$

The virtual photon with energy and momentum given by equations (1.5.4) and (1.5.5) interacts with the target nucleon in the second plane called reaction plane.

This interaction leads to an outgoing K^+ and a recoil hyperon. In the reaction plane the four momenta of K^+ , Y, and nucleon are given by:

$$P_{K^+} = (E_{K^+}, \vec{p}_{K^+}), \quad (1.5.6)$$

$$P_Y = (E_Y, \vec{p}_Y), \quad (1.5.7)$$

$$P_N = (E_N, \vec{p}_N). \quad (1.5.8)$$

The angle between these two plane is called the azimuthal angle and denoted by ϕ_k .

1.6 Hyperon (Y) Nucleon (N) Interaction

The hyperons are the baryons with one or more strange quark. With the new degree of freedom, *strangeness*, the hyperons are distinguishable from the nucleons. The study of hyperon-nucleon (YN) interaction can provide the information on the YN as well as the nucleon-nucleon (NN) interaction. The Λ N interaction is much weaker than the NN interaction. In the NN interaction, one boson (π) exchange is the dominant interaction. However, the Λ posses no isospin ($I = 0$) and nucleon has isospin $I = 1/2$, so that they cannot exchange a single pion ($I = 1$). Therefore, to conserve the isospin one-pion-exchange (OPE) is not allowed in the Λ N interaction. Since the OPE force is not present in the YN interaction, the short range properties of the baryon-baryon interaction becomes extremely important in Λ -hypernuclei. The long range component is due to the two-pion-exchange in the three body Λ NN interaction, which is overshadowed by OPE in the NN force in the ordinary nuclear physics [29]. Therefore, to the first order, the Λ N interaction is mediated either by a two-pion-exchange or a kaon exchange.

In the two-pion-exchange interaction, a Λ is converted into a Σ by emitting a meson (π) and then the Σ goes back to the Λ by emitting another meson (π). Then these two pions interact with the nucleons. Therefore, in the two pion exchange interaction, the Σ is the intermediate state. There is another possible interaction between the Λ and N in which only one kaon is exchanged. Actually, a Λ is converted into a nucleon by emitting a kaon and then the kaon converts a N into a Λ . The two-pion-exchange and a kaon exchange in the ΛN interaction are shown in Fig. 1.8 [15].

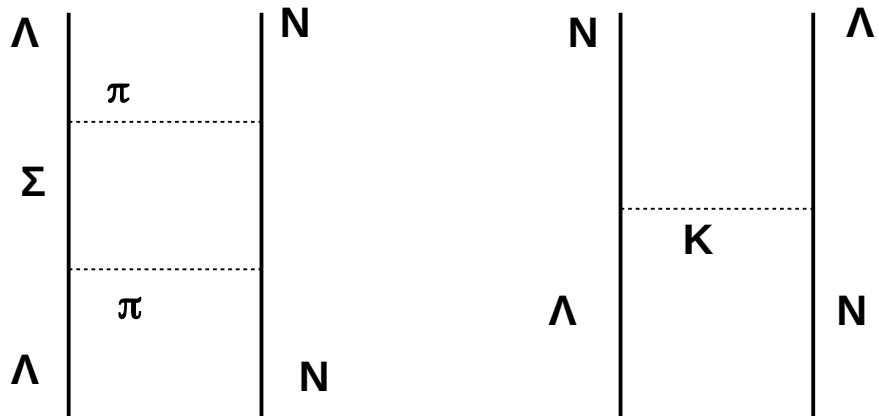


Figure 1.8. Two-pion-exchane and one kaon excahnge in the ΛN interaction.

1.7 The Purpose of the Present Study

1.7.1 Physics Motivation

The YN interaction can provide a platform to understand the baryonic interactions including the strangeness flavour and beyond. The addition of a new degree of freedom, namely *strangeness* to the nuclear medium provides opportunities to study the unknown properties of baryonic interactions in a practical way which is not possible from the investigation of ordinary NN interaction method. So far only limited

data exist for the YN scatterings as the YN and YY scatterings are difficult in comparison to the NN scatterings because of the extremely short lifetime of hyperons. In the case of the Λp interaction, the experimental data exist but was taken more than 50 years ago from a bubble chamber experiment. The data is poor with low statistics and high uncertainty [30]. In order to have a precise knowledge of the Λp interaction, additional Λp scattering data with improved statistics are needed. The Λn scattering data does not exist, therefore, Λn interaction is considered as having the same properties as that of the Λp interaction. To verify this, direct experimental data on the Λn interaction is needed. Recently, a Σp scattering experiment was performed at J-PARC (Experiment J-PARC E40) in 2019 and 2020 aiming to provide the differential cross sections of the $\Sigma^\pm p$ elastic scatterings and the $\Sigma^- p \rightarrow \Lambda n$ conversion [31].

1.7.2 Charge Symmetry Breaking

In nuclear physics, the charge symmetry is the basic property for the NN interaction. It is measured by taking the difference between the nn and pp scattering lengths [32] or the binding energy difference between the ground state of mirror nuclei 3H and 3He [33]. Figure 1.9 (a) represents the $A = 3$ isospin pair of mirror nuclei. After subtracting the Coulomb interaction between the protons in the 3He nucleus, the binding energy difference for $A = 3$ isospin pair was measured to be about 80 keV. Theoretically this much charge symmetry breaking (CSB) is considered small and can be explained either by $\rho^0\omega$ mixing in a one boson exchange model or by considering the two pion-exchange with $N\Delta$ intermediate states [34].

Recently, the binding energy of the 0^+ ground state of 4H [35] and the energy of the γ ray transition between 1^{st} excited state and 0^+ of 4He [36] was measured experimentally (see Fig. 1.9 (b)). From these two independent measurements, the binding energy difference between the 0^+ state of 4H and 4He was found about 270 keV which is more than 3 times larger than that observed in $A = 3$ isospin mirror

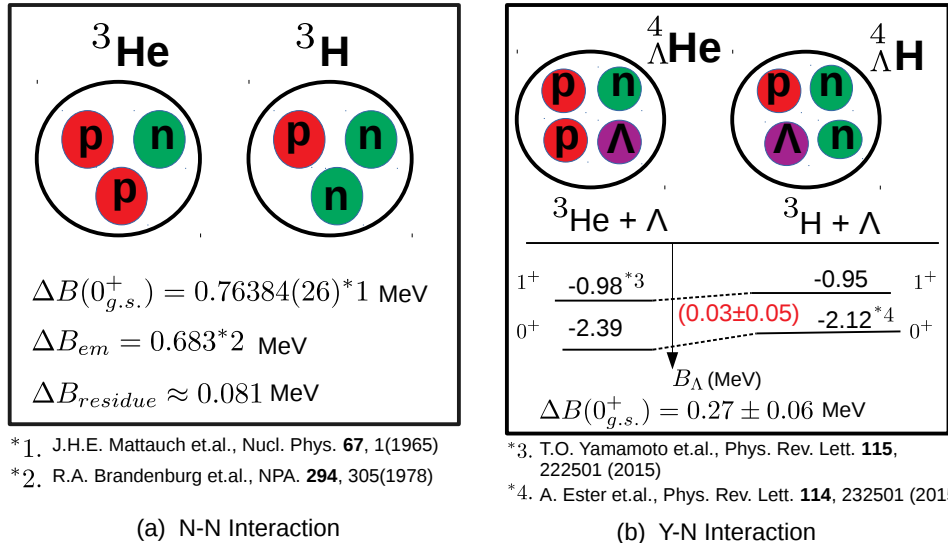


Figure 1.9. Schematic illustration of mirror pair of $A = 3$ nuclei (a) and $A = 4$ isospin mirror pair of Λ hypernuclei (b). A significant CSB can be seen in case of Λ N interaction with an unknown origin.

pair. The origin of such significant CSB in the Λ N interaction is unclear as the Λp and Λn interactions are considered identical. This strongly suggested that the Λn interaction need to be measured experimentally. Only the experimental data on the Λn interaction may shed light into the origin of such significant charge symmetry breaking. In the absence of the Λn data, some theories [32, 37] suggested that there might be $\Lambda \leftrightarrow \Sigma$ coupling producing significant CSB in Λ N interaction.

1.7.3 Approach to Λ N Interaction

Figure 1.10 shows the result of the HypHI [3] experiment at GSI. In this experiment $^3_{\Lambda}\text{H}$ and $^4_{\Lambda}\text{H}$ hypernuclei were produced by bombarding with a ${}^6\text{Li}$ beam with energy of $2A$ GeV on a fixed graphite (${}^{12}\text{C}$) target. The experiment was studying the life time of the hypernuclei ($^3_{\Lambda}\text{H}$ and $^4_{\Lambda}\text{H}$) from their two-body weak decays. However, by reconstructing the missing mass, they found an unexplainable peak which was claimed to be a bound state of three-body neutral Λ system [see Fig. 1.10 (b1) and (b2) in

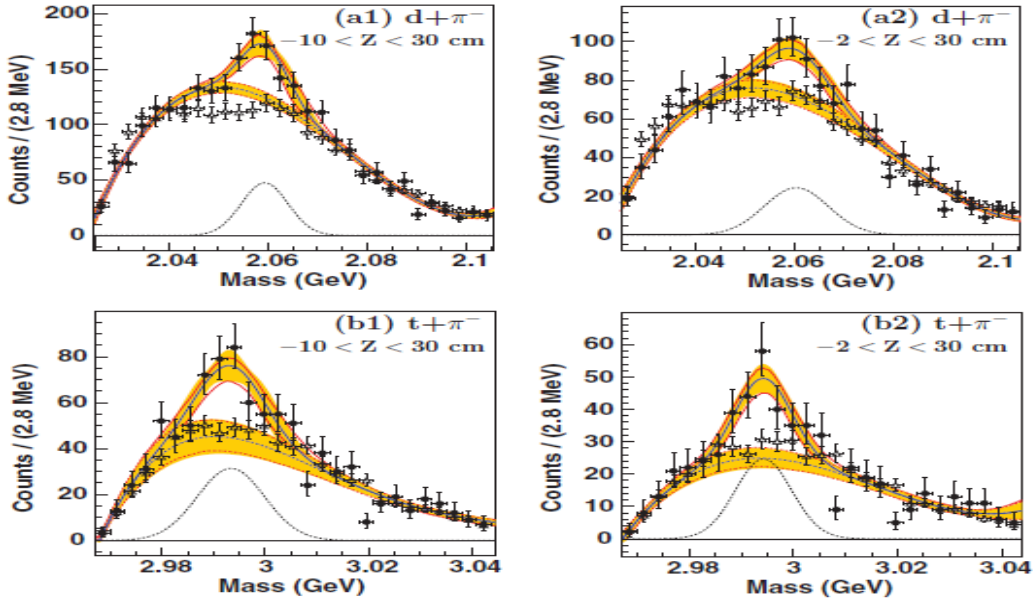


Figure 1.10. Result of the HypHI [3] experiment at GSI. (a1) and (a2) represent the invariant mass distributions from the $d + \pi^-$ decay and (b1) and (b2) represent the same from $t + \pi^-$ decay.

comparison to (a1) and (a2) for an unbound two-body Λn system]. Immediately, many theorists got excited and they made calculations using the current YN interaction models but all ruled out the bound Λnn system. However, some theoretical studies indicated that the Λnn resonance may likely exist and by measuring the binding energy and natural width of such state it is possible to extract the unknown Λn interaction. Therefore, an independent experiment that can verify the existence of either a resonance state or a bound state will be extremely important. As indicated by the theories, if such a physical state exists, it may provide, for the first time, experimental information about the Λnn interaction.

1.7.4 Theoretical Investigation on the Λnn Resonance

Several theoretical studies [38–40] were carried out to investigate the existence of the three body Λnn resonance. For the study in [40], the authors used the pairwise

interactions of rank one, that is, they separated the three body Λnn potential into two body nn and Λn interactions. Four different baryonic potential models (see Fig. 1.11) were used to fit for the effective range parameters of nn and Λp interactions from the existing scattering data. The Λnn Faddeev equation was solved into the second order complex plane to obtain the energy eigenvalue. The Λp and Λn interactions were assumed as identical to begin with and then the Λn strength was increased by 2.5% in each step to obtain the energy eigenvalue spectrum. The x-axis of the spectrum gives the real part, the eigenvalue which corresponds to the binding energy and the y-axis gives the imaginary part which corresponds to the natural width of the system. The study found consistently with all four models that it takes only about 5% increase for a physical resonance to appear and it is well within the fitting uncertainty of the Λp potential. Thus, the study concluded that such a resonance is likely to exist. On the other hand, this study indicates that the unknown Λn interaction can be determined if the binding energy and natural width of this resonance can be measured with good precision.

1.7.5 Available System for the E12-17-003 Experiment

The E12-17-003 experiment was performed in the experimental Hall A in November 2018 aiming to search for the Λnn resonance via the mass spectroscopy using the $(e, e' K^+)$ reaction with a tritium target. Before this experiment, several other tritium experiments were performed in the experimental Hall A, the experimental hall was in the operational mode. Most of the systems including the detector calibration and DAQ system were already optimized by the prior tritium experiments, therefore, this experiment used the optimized Hall A system. All of the required gas target cells were already installed in the target chamber as all of the approved tritium run group experiments used the common gas target cells. The only extra equipment needed was the particle identification detector in the right arm as the existing gas

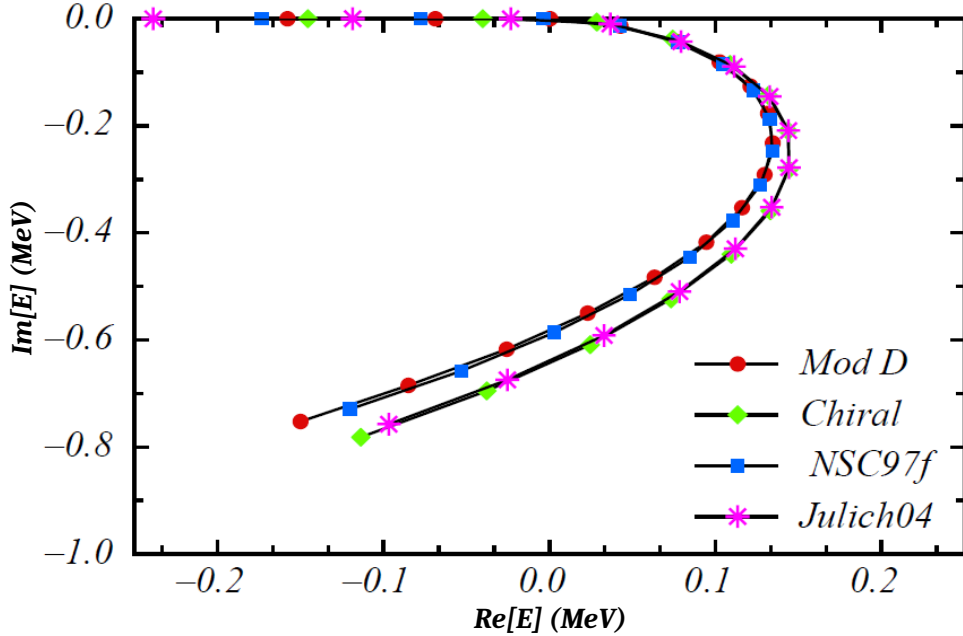


Figure 1.11. The complex energy eigenvalue spectrum. Four different trajectories of the resonance pole with the Λn interaction. These curves were obtained using four different theoretical models (Mod D, Chiral, NSC97f, and Julich04). Each model fitted the effective range parameters of nn and Λp interactions from the existing data.

Cherenkov detector can not detect the hadrons. Therefore, two available low index Aerogel detectors (A1 and A2) were installed in the right arm before the experiment as a K^+ identification detector. The other things that were needed was the relocation of the HRS position and the adjustment of electron beam energy as required by the experiment which were done right before the experiment. The quality CEBAF beam and the existing equipment provided the unique opportunity for this experiment.

CHAPTER 2

THE E12-17-003 APPARATUS

2.1 Overview

A series of tritium experiments were performed in the experimental Hall A, Jefferson Lab, between 2017 and 2018. The E12-17-003 was the last one and the only hypernuclear experiment in the tritium family. The E12-17-003 experiment took the production data during November 2018.

The E12-17-003 is a coincidence type experiment. The beam electron with energy of 4.326 GeV scattered off a target nucleus producing either a Λ or Σ hypernuclei along with the emission of a K^+ . The scattered electrons (e') were detected in the left arm (LHRS) which was kept under the negative polarity while the coincident K^+ were detected in the right arm (RHRS) kept under the positive polarity. The experiment was proposed in 2017 and was approved with remark of high impact. By the time when the experiment got approved the experimental hall was preparing for the previously approved tritium experiments. Therefore, it took the advantage of having the newly designed tritium target along with the high resolution spectrometers, although the existing system was not perfect for kaon experiment.

Initially, the run period for this experiment was allocated from October 30 to November 20, 2018. However, since the beam was not stable during the run time thus the run period extended to November 26, 2018. This $(e, e'K^+)$ experiment was able to collect about 85% of the expected data with the production target (tritium target). In this chapter, the major components of the experiment will be discussed.

2.2 CEBAF

The Continuous Electron Beam Accelerator Facility (CEBAF) at Thomas Jefferson Laboratory provides multi GeV continuous wave (CW) polarized beam for experiments related to nuclear and particle physics interface [41]. It is based on the superconducting radio frequency (SRF) technology which generates high quality of electron beam with high intensity as well as controlled polarization. CEBAF started its operation for physics program in 1995 with a 4 GeV maximum beam energy. In August 2000, it was upgraded to 6 GeV and then in 2017, it was further upgraded to 12 GeV. This upgrade allow to deliver up to 11 GeV electron beam to three experimental Halls A, B, and C and 12 GeV beam to the newly constructed Hall D [42].

The CEBAF consists of two antiparallel superconducting linear accelerators (linacs) linked by nine recirculation beam lines for up to five passes. Each linac is approximately a quarter mile long and is 30 feet underground. The two linacs are joined by circular arcs with magnetic field to bend the electron trajectories. The electron beam passes through both linacs and gains energy on each pass. One unique feature of the accelerator is that while the beam energy grows, the electron velocities all remain nearly identical to the speed of light, so that the multiple beam energies may be simultaneously co-accelerated.

CEBAF machine has a circularly polarized laser light which is allowed to shine on a gallium arsenide (GaAs) photocathode. During this process the photons from the laser excite the electrons from the valence band to the conduction band of the GaAs. A voltage of -100 keV is applied to the photo cathode to extract the electrons from the conduction band. A set of cryomodules accelerate the electrons to 100 MeV at which point they are transmitted to north linac and accelerated through a series of cryomodules and subsequently extracted to four different experimental halls.

2.3 Hall A Overview

The Experimental Hall A is located at the end of the south linac and is the largest hall among all four experimental halls at Jefferson Lab. It is built underground in a circular shape with a diameter of about 53 m and height of about 17 m. Hall A has a beam line which transports the electron beam to the target where the nuclear interactions of interest takes place. The main components of Hall A are two high resolution spectrometers (LHRS and RHRS) which are capable to provide a momentum resolution better than 2×10^{-4} . Each of the spectrometer is provided with a standard detector package and are responsible to detect the transported charged particles such as the scattered electrons (e') and produced hadrons (such as K^+ in our case). The 12 GeV upgrade allow Hall A to receive up to 11 GeV electron beam. A detailed discussion about Hall A and its components will be discussed in the following sections. The schematic diagram of main components of Hall A is shown in Fig. 2.1.

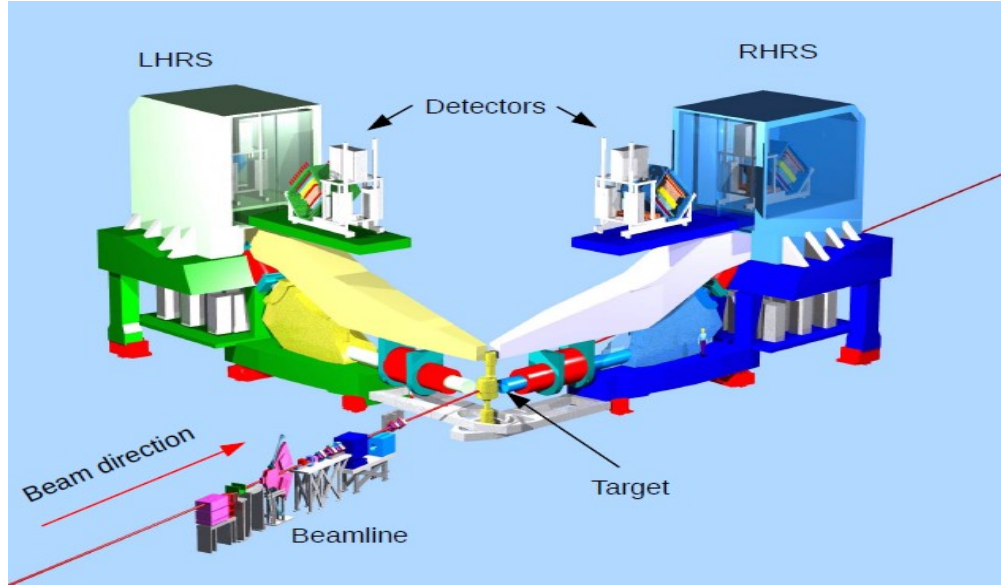


Figure 2.1. Schematic view of the experimental Hall A showing two high resolution spectrometers.

2.4 Kinematic Setting

The kinematics used in the E12-17-003 experiment is presented in Table 2.1. An electron beam with an energy of about 4.326 GeV was scattered off a proton in a target nucleus by exchanging a virtual photon with the nucleus as shown in Fig. 2.2. The scattered electrons (e' s) and produced hadrons (K^+ s) were detected separately in the two high resolution spectrometers LHRS and RHRSS, respectively.

Table 2.1

The basic kinematics used for the E12-17-003 experiment.

| Parameters | H kinematics (calibration data) | T kinematics (production data) |
|--------------------------------|---------------------------------|--------------------------------|
| Beam energy (GeV) | 4.326 | 4.326 |
| LHRS central momentum (GeV/c) | 2.1 | 2.218 |
| RHRS central momentum (GeV/c) | 1.823 | 1.823 |
| LHRS scattering angle (degree) | 13.2 | 13.2 |
| RHRS scattering angle (degree) | 13.2 | 13.2 |

For the production runs (here refers to the T kinematics), the central momenta for the electron and hadron arm were set 2.218 GeV and 1.823 GeV, respectively. During the calibrations runs (refers to the H kinematics) the central momentum of LHRS was lowered to 2.10 GeV while keeping other parameters same, in order to have both Λ and Σ^0 in the acceptance.

For each kinematics, both of the spectrometers were symmetrically positioned at a constant angle 13.2° with respect to the beam direction. In this configuration, the RHRS is approximately aligned to the virtual photon direction. The production data were taken with the tritium target where as the calibration data were collected with the H target. For the H target, data was taken also with the T kinematics so that

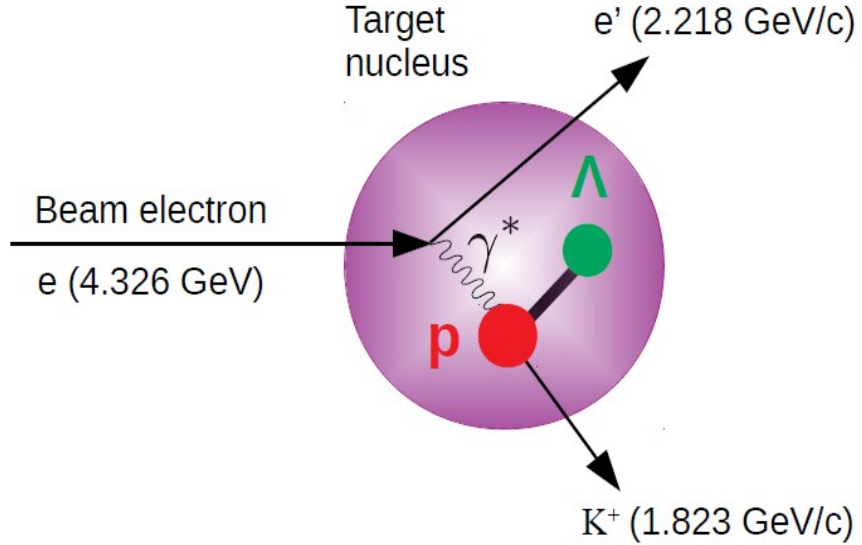


Figure 2.2. Production of hypernuclei via the $(e, e' K^+)$ reaction.

the known mass of Λ can be used to ensure the correct scaling of LHRs between the two kinematics.

2.5 Hall A Beam Line Instrumentation

The experimental Hall A and its scientific equipment provides opportunities to study the electro- and photo-production reactions [43, 44]. Some of the studies, for example $(e, e' K^+)$ reaction study, requires the high precision measurements not only in the spectrometer system but also the high quality of electron beam. In order to measure the beam properties such as the beam energy, beam position, beam charge and beam direction precisely, the beam line instruments were used which are shown in Fig. 2.3.

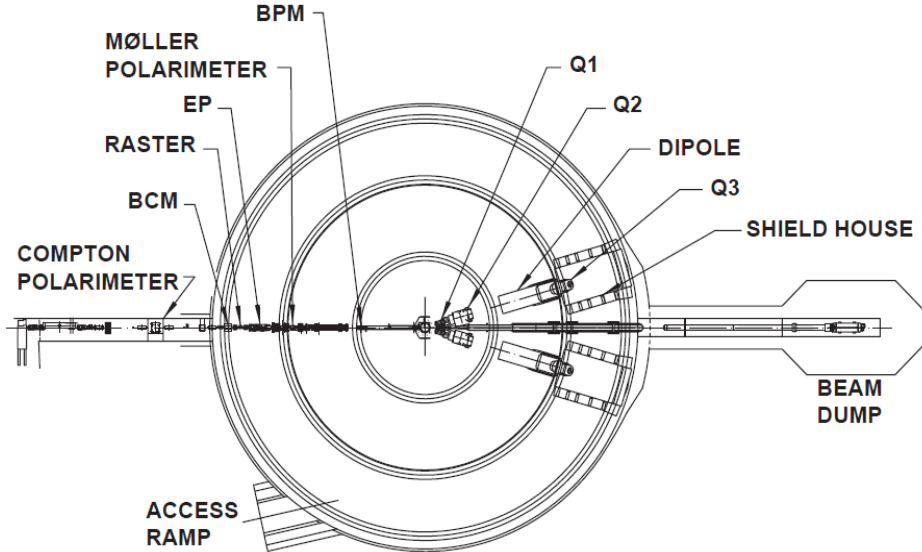


Figure 2.3. A schematic layout of the beam line components [4].

2.5.1 Hall A Arc Energy Measurement

The E12-17-003 is a high precision experiment and knowing the precise value of beam energy in the hall is critically important to control the rest of the kinematics, for example, the HRS angle and momentum in order to extract the meaningful physics from the data. The beam energy was measured by using the arc energy method [45] which is based on the beam transport system. In this method the deflection of the electron beam in the arc region of accelerator was measured.

The Hall A arc consists of 8 identical dipole magnets connected in a series and placed in a vacuum. These dipoles are inaccessible for a field integral. During the beam operation, a 9th reference dipole is used which is both identical and powered in series with other dipoles. This reference dipole is placed outside the beam tunnel in a separate building and is used to measure the field integral.

To measure the field integral a field mapper equipped with two coils mounted on a table is moved through the reference dipole with a known velocity. The bending angle

of the electron beam is measured by using a series of scanners called harp. A pair of harps provides the beam positions in the horizontal (x) and vertical (y) directions. There are two pairs of harps, one is located at the beam entrance and the other is at the beam exit. Each harp consists of three tungsten wires which are placed into the path of the beam by using the stepping motor. When the electron beam hit the wire, an electromagnetic shower is induced from the wire which is read by a photo multiplier tube (PMT) and the position of the beam is determined accurately. The harp scan and the data taking in the hall can not be done simultaneously as the harp scan is a destructive measurement. The nominal bending angle of the beam is 34.3° , (see Fig. 2.4). Finally, with the integrated field of dipoles and the known bending angle, the energy of the electron beam is calculated by:

$$p = k \frac{\int \vec{B} \cdot d\vec{l}}{\theta}, \quad (2.5.1)$$

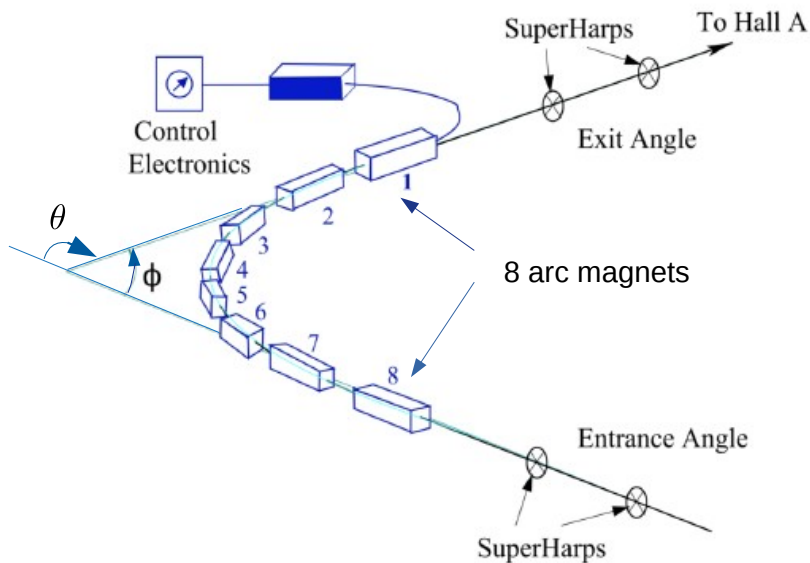


Figure 2.4. Schematic for the Hall A arc energy measurement.

where, k is a constant ($0.299792 \text{ GeV rad } T^{-1}m^{-1}/c$), $\int \vec{B} \cdot d\vec{l}$ is the field integral, and θ is the bending angle due to arc. The arc energy method provides absolute beam energy measurements $\delta E_{beam}/E_{beam} \sim 2 \times 10^{-4}$.

2.5.2 Beam Energy Stability

To deliver the precise value of the beam energy to the target, CEBAF developed two additional systems, the fast feedback system and the synchrotron light interferometer system. The details about each of the systems will be discussed in this section.

Fast Feedback System

The electron beam delivered to the target affected by the undesirable positional and energy fluctuations. The energy fluctuations mainly occur at the power line harmonics in the integral multiple of 60 Hz (60, 120, 180, etc. Hz). The main reason of having such energy fluctuation is electronic noise created by different electronics as well as the electromagnetic field generated by the accelerator electronic equipment. To solve this problem, a system called the fast feedback (FFB) system was developed. The FFB system mainly contains the software and hardware and are installed at the two different locations of the accelerator. Each system consisted of a single VME crate housing an MVME167 CPU, a DAC for driving the actuators, and the specialized modules used for the SEEs [46]. One system provide energy and position feedback for the beam leaving the injector and the other provide the same for the beam after it passes through the first linac. The FFB system reads the beam momentum, makes calculations and tells how much the momentum needs to be corrected. Then it feeds this information to the module very quickly to vary the electric field and read it again. After that the beam energy centroid is locked making sure the statistical mean locked as precise as the experiment required. The FFB system can ensure that the relative

energy stability is controlled below or equal to 10^{-4} (FWHM). Some more details about the FFB system can be found in Ref. [47].

Synchrotron Light Interferometer

Electrons are liberated when the laser light shines on a gallium arsenide photocathode. The quality of the beam electron energy leaving the injector may vary and can have energy spread. In addition, if the laser is not focused and tuned very well, the knockout electrons have a lot of energy spread resulting the dominant energy uncertainty. The inaccurate value of energy may not allow to reach the physics goal of the experiment especially for the high precision experiment. To monitor the intrinsic beam energy spread, two synchrotron light interferometers (SLI) were installed at the center of the Hall A arc region, where the momentum dispersion is the maximum. The complete SLI system consists of the software as well as the hardware. When a relativistic charge particle travels in a curved path, it emits the synchrotron radiation (SR) in the tangential direction resulting the interference patterns. The SLI system measures the interference patterns in every 2 sec. By measuring the dark and bright fringes, the energy spread is calculated. If the beam energy spread measured by SLI system exceeding the experimentally required minimum ($\sigma = 10^{-4}$ FWHM), it starts alarming. The SLI system itself cannot control the quantity (beam energy spread) but notify the shift crews by alarming. In such case, the injector need to be retuned. During the E12-17-003 experiment, the entire interoferometer was always on but never alarmed. Some more details about the SLI system can be found in Ref. [48]. These are essential for this experiment due to the requirement on precision.

2.5.3 Beam Current Monitor

To provide the stable, low noise, and non invasive current to the experimental hall as well as to measure the amount of charge delivered to the target, a system called

beam current monitor (BCM) was designed and installed 25 m upstream from the target in the experimental hall. The BCM mainly consists of a parametric current transfer (PCT) known as Unser monitor, two cylindrical radio frequency (RF) cavities, associated electronics, and a data acquisition (DAQ) system [49]. The Unser monitor is positioned along the beam line and placed between the RF cavities. The cavities and the Unser monitor are enclosed in a box to isolate from the external magnetic field and temperature variations.

The RF cavities are tuned to match the frequency of the beam. In each cavity there are two loop antennas, one of which provide an output signal proportional to beam current. The output RF signal from each cavity is fed into a down converter where it splits into two parts. One part sent to three different amplifiers (x1, x3, and x10). Each of these amplifiers covers different linear region, so that a total of 3 μA to 200 μA linear region of current is covered. Each amplified output signal is then fed into the RMS to DC converter which results an analog DC voltage as an output. This output voltage is then sent to a voltage to frequency (VTOF) converter. The VTOF output signal is sent to a fastbus scaler which is read by a DAQ system. The other part of the RF cavity output is sent to a high precision digital AC converter which produces a digital output as the RMS value of the input signal averaged over one second period. In another word, this output signal is proportional to the beam current over each second and sent to the computer.

The gain and offset of RF cavity is measured with the help of Unser monitor by passing an electron current through the cavity. Then the time accumulated charge is calculated from the scaler as the number of counts measured by the scaler is proportional to the integrated charge. Mathematically,

$$Q = I \cdot t = (\text{gain} \cdot \frac{\text{BCM counts}}{t} + \text{offset}) \cdot t, \quad (2.5.2)$$

$$t = \frac{\text{Clock counts}}{f_0}, \quad (2.5.3)$$

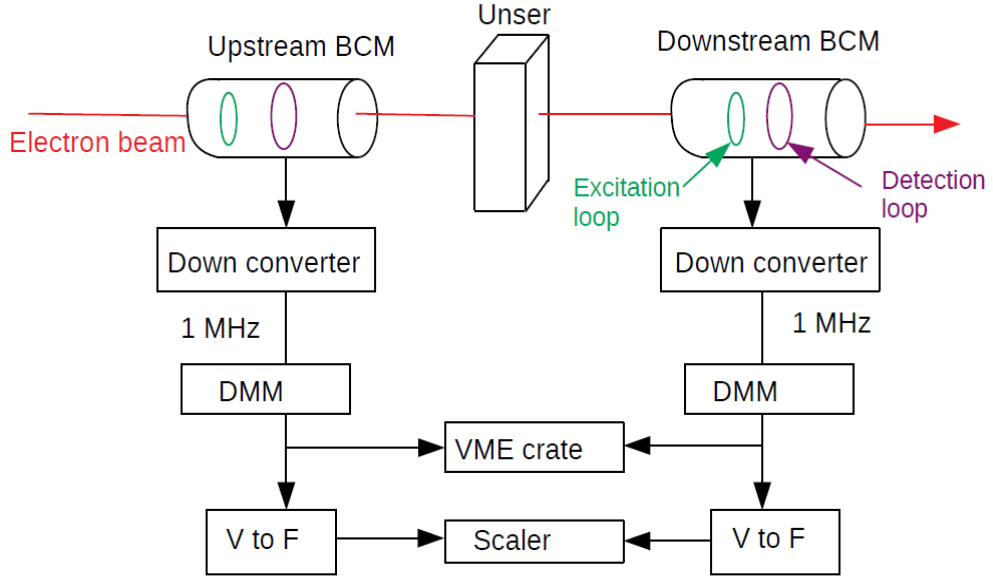


Figure 2.5. Schematic of the Hall A beam current measurement.

where, $f_0 = 103700$ Hz is the clock signal frequency sent to both spectrometers and I is the beam current which is proportional to the BCM rate. Figure 2.5 indicates the layout of each component of BCM system.

2.5.4 Raster

The accelerator delivers an electron beam to the experimental hall with a beam size of about 80 to 200 μm [50]. This small spot size of the beam, depending on the current in use, can cause the extreme fluctuations in the target's temperature and density. To mitigate this effect the electron beam is spread over larger region of target by applying a raster to the beam.

The Hall A raster system is located 23 m upstream of the target and consists of two sets of raster [51]. Each set consists of one pair of steering dipoles in the transverse direction. A triangular wave of frequency about 25 kHz is powered to each of the dipole magnets to spread the beam. The beam position is moved with a time varying magnetic field with the triangular waveform resulting a rectangular

shape beam with size of about $2.2 \text{ mm} \times 2.6 \text{ mm}$. The raster patterns are shown in Fig. 2.6.

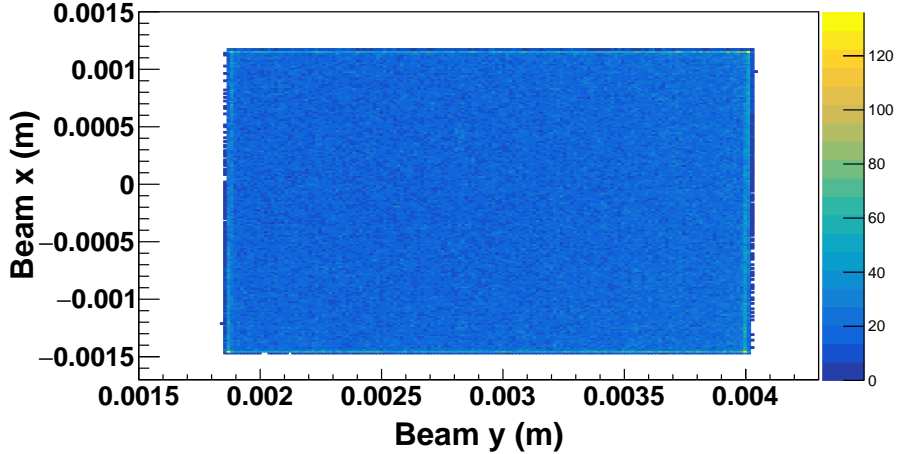


Figure 2.6. Rastered beam y vs beam x.

2.5.5 Beam Position Monitor

Most of the Hall A experiments including the E12-17-003 experiment require the precise measurements of beam position at the target. In order to precisely measure the position and direction of the beam at the target, Hall A uses two beam position monitors (BPMs) which are located 7.524 m (BPMA) and 1.286 (BPMB) upstream of the target, respectively [52].

The main component of the BPM is a 4-wire antenna which is arranged in a cylindrical cavity parallel to the beam axis and surround the beam line equally. The antenna are tuned to the fundamental frequency of 1.497 GHz of the beam [53]. When the electron beam passes through a BPM, a signal is introduced in the wire. This signal is then decoded by an ADC module. By fitting a straight line on the two BPM measurements, the beam position and beam angle for each individual BPM is determined. The BPMs provide a non-invasive method which can measure the relative position of the beam to $100 \mu\text{m}$ with a beam current of greater than $1 \mu\text{A}$.

The BPMs are calibrated by using a set of harps which are located adjacent to the BPMs. The complete diagram of BPM is shown in Fig. 2.7 [54].

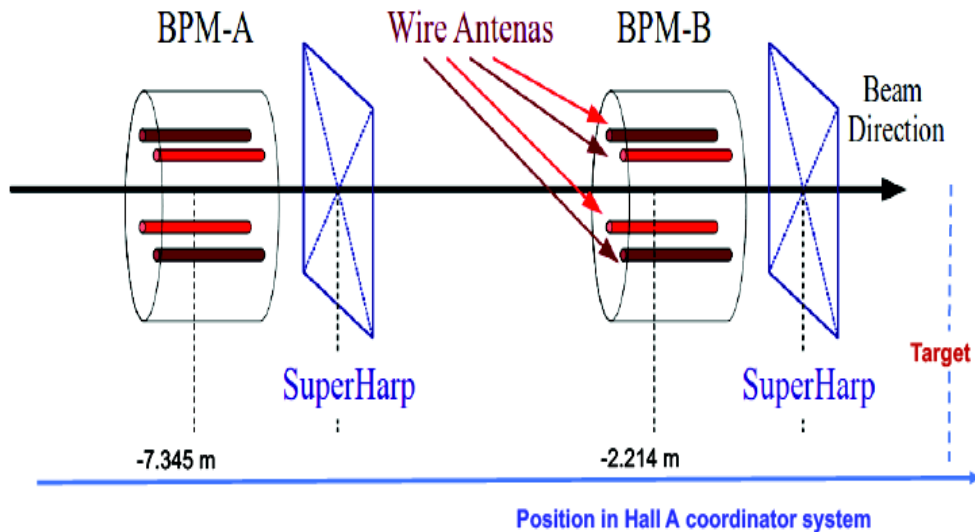


Figure 2.7. Schematic of the Hall A BPMs and harps.

2.6 Target System

2.6.1 Overview

A series of tritium experiments were performed in the experimental Hall A during 2017 and 2018 by using a common tritium target. Since the ${}^3\text{H}$ is the radioactive and rare isotope of H atom, the construction of the target was the central interest. It took several years to reach the final design of the target. The ${}^3\text{H}$ target was designed in such a way that it met the safety standard as well as the physics goal of the experiments. The target cell was filled offsite at Savannah River site Tritium Enterprises (SRTE) and shipped to Jefferson Lab in a special container.

First time it was shipped to JLab during fall of 2017. The E12-10-103 and E12-14-011 experiments took data with this target and then it was shipped back to SRTE

during late spring 2018. For the fall 2018 experiments, SRTE refilled the target cell and shipped to Jefferson Lab again in the beginning of fall 2018.

Besides the tritium target, all of the tritium group experiments took data with other gas targets such as ^1H , ^2H and ^3He . All of these targets used the identical target cell and filled on site at Jefferson Lab. In addition to the gas targets, the $(e, e'K^+)$ experiment took data with some solid targets depending on the physics need of the experiment. The targets and the purpose of their usage is summarized in Table 2.2.

Table 2.2

The list of targets used in the E12-17-003 experiment.

| Target name | Type | Target material | Thickness (mg/cm^2) | purpose |
|---------------|-------|-----------------|---------------------------------------|---------------------------------------|
| Tritium | gas | ^3H | 85.099 ± 0.825 | Production |
| Helium3 | gas | ^3He | 53.3752 ± 0.57 | Calibration |
| Hydrogen | gas | ^1H | 70.8 ± 0.3974 | Calibration |
| Dummy cell | solid | Aluminum 7075 | - | Background study |
| C-Multi foil | solid | Carbon 99.95% | - | Optics |
| C-Single foil | solid | Carbon 99.95% | - | Raster calibration |
| Carbon hole | solid | Carbon 99.95% | - | Raster calibration and beam alignment |

2.6.2 Target Cell Design

The design of the gas target was driven to meet the safety standard of the tritium target as it is radioactive. Some additional details about the tritium target can be found in Ref. [55]. The target system was designed in the following ways:

- The target cell has a modular design (see Fig. 2.8) which allows the tritium cell to be filled offsite Jefferson Lab.
- The gas was filled in a cylinder made of 7075 aluminum alloy. The length of the cylinder is 25 cm with a diameter of 12.7 mm. After the gas was filled in the cylinder it was sealed to prevent the gas leak.

- The target cell has two windows to enter and exit the electron beam. The scattered electrons as well as the produced hadrons had to pass through the cell side walls before they escaped to the spectrometer. Therefore, the inner boundaries of the cell was designed as thin as possible without compromising the safety requirement of the tritium gas. The inner wall thickness varies from 300 μm to 500 μm .
- The maximum beam current allowed for the gas target was limited to 22.5 μA .
- The liquid helium at 15K supplied by the end station refrigerator (ESR) was used to cool down the gas target to a temperature of 40K.
- The design of the gas target is compatible to all of the safety operations under all possible operational phases of tritium target including the beam operation, transportation, installation, and storage.

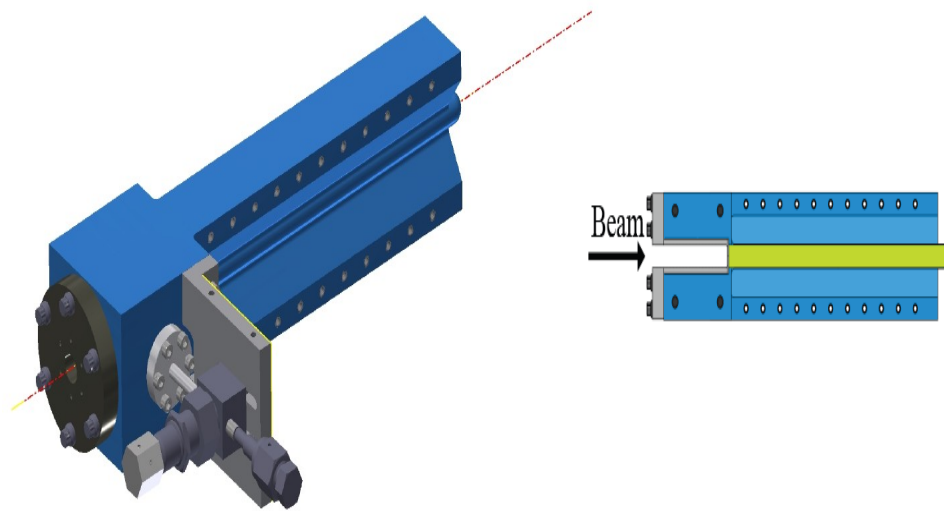


Figure 2.8. Schematic of the gas cell design (left). Side view of the cell where the bright green region represents the gas volume (right).

2.6.3 Tritium Target Safety System

To minimize the safety hazards associated with the tritium target, a special target system with three layers of confinement was designed during the operation.

1. To minimize the tritium material and to mitigate the risk of the leakage of the tritium gas, the target was sealed after it got filled and had a modular design. The target gases were not circulated like typical cells used in Hall A in the past. This sealed target cell is considered as the first layer of confinement.
2. An exhaust system as the second layer of confinement was installed in the target chamber to be able to remove the accidental release of tritium gas in a controlled manner.
3. As the third and final layer, all of the doors of the experimental hall were locked including the truck ramp door.

In addition, a traffic cone was kept in front of Hall A truck ramp door and used as a visual clue to determine if the truck ramp door was up. The camera could not see the door well, so a rope was tied from the door to the cone to help the shift taking people to see if the door is down. The door was malfunctioning and would open for no reason. Unfortunately, the cone did fall down a couple of times during the tritium run time and beam had to stop immediately to close the door.

2.6.4 Target Scattering Chamber

A previously used cryogenic target chamber was refurbished to a new target chamber for all of the tritium run group experiments. This new chamber was compatible to meet the safety standard of the radioactive target. To prevent the beam hitting to the thin side wall of the aluminum cell a 4 inch long and 0.4 inch long inner diameter collimator was installed inside the target chamber upstream of the target ladder. An exhaust system was installed inside the chamber to control the accidental leakage of the tritium gas. The target chamber was kept under vacuum and isolated from upstream beam line by a beryllium window. To hold the gas and solid targets, a target ladder was also installed inside the target chamber. In order to control the tempera-

ture of the target cell, a heat sink with flowing cryogenic was used. The target ladder was motor controlled which can be accessed remotely. The following identical target cells were mounted on the target ladder (see Fig. 2.9):

- Tritium
- Deuterium
- Hydrogen
- Helium-3
- Empty

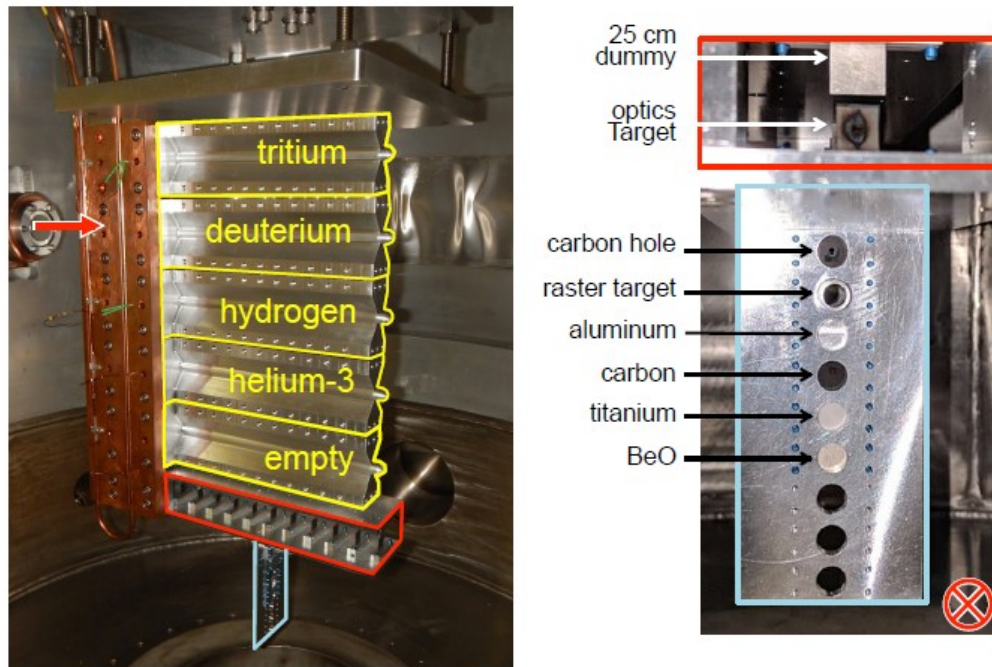


Figure 2.9. (Left) Schematic of the target ladder with the yellow mark shows the gas targets, the red mark shows the carbon multi-foil target, and blue mark shows other solid targets. (Right) Front view of solid targets [5].

The E12-17-003 experiment did not take any data with the deuterium target which was used by other tritium experiments. In addition to these gas target cells, several solid targets were also mounted on the target ladder for other studies:

- Carbon hole, A carbon foil with 2 mm diameter hole in its center.
- Raster target
- Carbon multi-foil target

2.7 Sieve Slit and Collimator

A removable sieve slit (SS) was installed in front of each spectrometer for the optics runs. It was made of 1 inch thick tungsten material and had a rectangular shape. The holes were drilled in the horizontal and vertical directions with the hole diameter 4 mm. There were two big holes with diameter 6 mm [56] and one of them was drilled at the center of the SS plate. The big holes were used to identify the SS geometry and determine the rows and columns. The center of the SS was aligned along the central ray of the spectrometer.

The main reason of installing the SS was that only those scattered particles whose track passes through the SS holes can reach the detector plane while stopping or scattering out of the acceptance all of the other particles by the SS plate. The particles detected at the detector plane are corresponding to specific in- and out-of-plane angles at specific reaction vertex. The SS plate was placed 1.03 m away from the target center at $z = 0$, therefore, 1 mrad corresponds to about 1 mm on the plate. Figure 2.10 shows the schematic of the SS installed at one of the spectrometers.

In the past experiments, Hall A used the collimators for the spectrometer acceptance studies. Later it was found that it worked great for the point like targets, however, for the extended targets it created problems as it could not define the acceptance in the HRS. Therefore, Hall A relies on a software acceptance determination for the extended targets. Therefore, no collimator was used on HRS for all the tritium experiments.

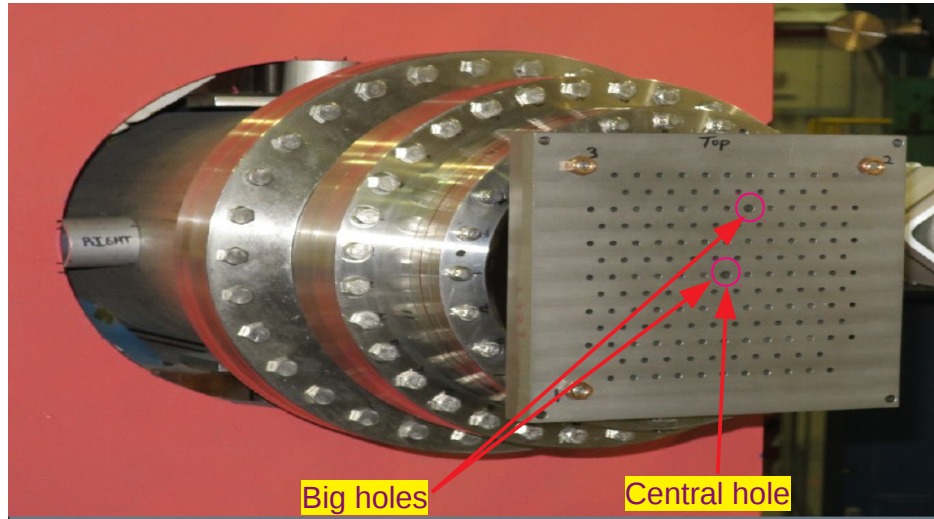


Figure 2.10. Schematic of the SS plate installed in one of the spectrometers.

2.8 Hall A High Resolution Spectrometer System

2.8.1 Overview

The experimental Hall A consists of two nearly identical high resolution spectrometers placed left and right side of the beam direction. These spectrometers are used to transport and detect the charge particles with high degree of precision. Depending on the physics need of the experiments either only one or both of the spectrometers can be operated together at the same time. As a coincidence experiment, the ($e, e' K^+$) experiment used both of the spectrometers for the whole run period. Both of the spectrometers were installed in such a way that they can be controlled remotely and able to rotate independently. The LHR_S can rotate from 12.5° to 150° and RHR_S can go from 12.5° to 130° depending on the experimental requirements. For the E12-17-003 experiment, both of the spectrometers were positioned symmetrically at 13.2° with respect to the beam direction.

Each spectrometer mainly contains three parts, a magnetic particle transport system, a complete detector package, and a data acquisition system. The charge

particles are either scattered or produced at the target by some reactions and then these particles are transported to the detector system by using the magnetic particle transport (spectrometer) system. The magnetic particle transport system is combination of quadrupole (Q) and dipole (D) magnets in the QQDQ sequence. The charge particles are then detected by the detector system. The detector system is the combination of several detectors. Finally, all types of required information such as the particle position, its momentum, flight time, angle information etc. at focal plane are recorded by the DAQ system in the form of the raw data. The basic layout of the HRS detector system is shown in Fig. 2.11.

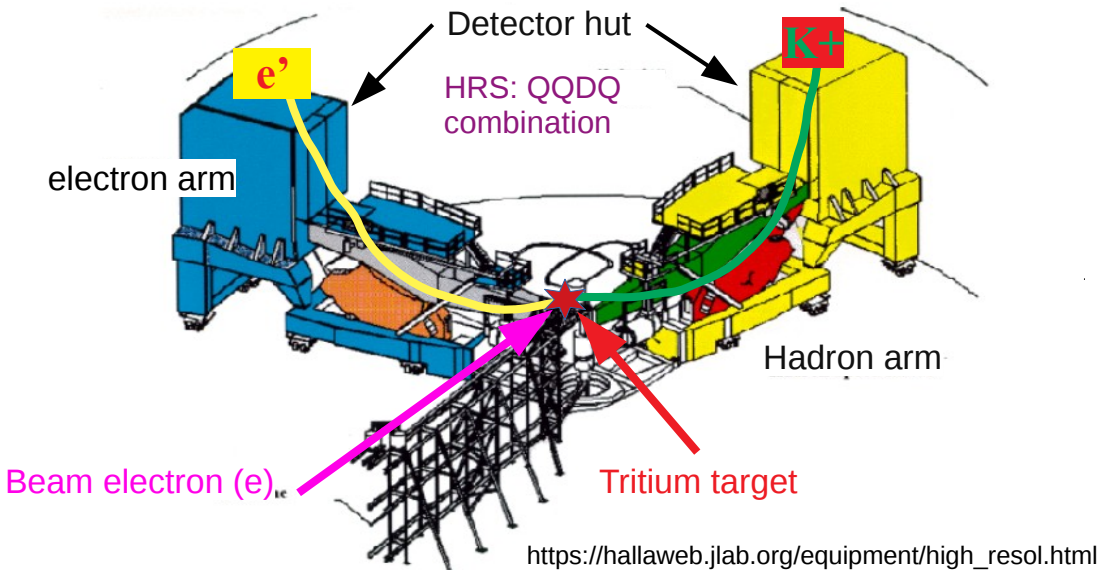


Figure 2.11. Schematic of the Hall A HRS system illustrating the beam electron, LHRS, and RHRS with the corresponding detector huts.

2.8.2 HRS Design and Characteristics

The high resolution spectrometers (LHRS and RHRS) are the main components of the experimental Hall A [57] which can provide high momentum resolution at the level of 10^{-4} over the range from 0.3 to 4.0 GeV/c [58]. Each spectrometer consists of two superconducting quadrupoles (Q) followed by a 6.6 m long dipole. Next to the

dipole magnet, there is another superconducting quadrupole (Q) making a sequence of QQDQ (see Fig. 2.12).

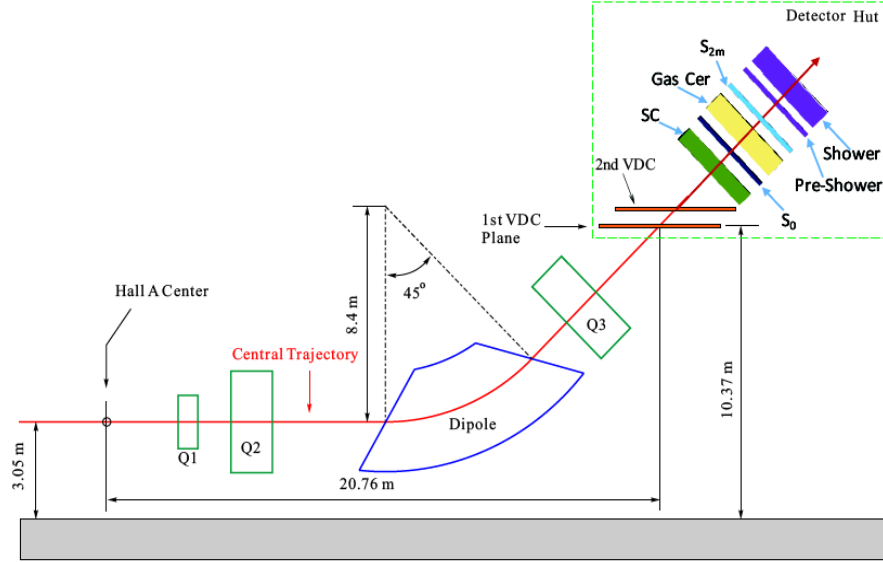


Figure 2.12. Schematic of the Hall A HRS system showing the magnetic particle transport system.

The main function of Q1 is to focus the scattered particles in the vertical direction. That means Q1 converges the scattered charged particles in the dispersive plane. The Q2 and Q3 are identical in design and size and are responsible to provide the focusing in the horizontal (transverse) direction. The upward momentum dispersion is because of the dipole magnet sandwiched between Q2 and Q3. Each of the spectrometer has the following characteristics:

- Each of the spectrometer transports the scattered charged particles to the detector plane.
- The spectrometers can be operated with either polarity.
- The spectrometer central momentum ranges from 0.3 to 4.0 GeV/c .
- The magnetic system of each spectrometer provides a momentum resolution better than $\pm 2.0 \times 10^{-4}$.
- The dipole from each HRS bends the charge particle by 45° towards the detector plane.

- Each HRS has a nominal angular acceptance about ± 30 mrad in the horizontal direction and ± 60 mrad in the vertical direction.
- The central momentum acceptance of each HRS is $\Delta p/p = \pm 4.5\%$.

2.9 HRS Detector Package

2.9.1 Overview

Each of the spectrometers housed in the experimental Hall A equipped with a complete set of detector package for particle tracking, timing, and identification. The particles are originated at the target and transported to the detectors with the help of HRS spectrometers. In addition, the detector system is capable to provide the triggers (signals) and timing information to the DAQ system. A schematic of complete detector package is shown in Fig. 2.13. For the E12-17-003 experiment the main components of the detector package were:

- A pair of vertical drift chambers for particle tracking.
- Two scintillator planes S0 and S2 used for timing as well as triggers.
- Gas Cherenkov and two layers of lead glass (pre-shower and shower) detectors for particle identification.
- Two additional low index Aerogel Cherenkov detectors (in RHRs only) specifically for the K^+ particle identification.

The details about each of the detectors will be discussed in the following sections.

2.9.2 Vertical Drift Chambers

To determine the position and angle of the scattered particles with high precision at the focal plane, a pair of vertical drift chambers (VDCs) were installed in each HRS at the entrance of the detector stack [59]. The two VDCs were separated by a distance of 335 mm from one another. Each VDC contains two wire planes in a standard UV formation and each wire plane contains 368 signal wires called sense

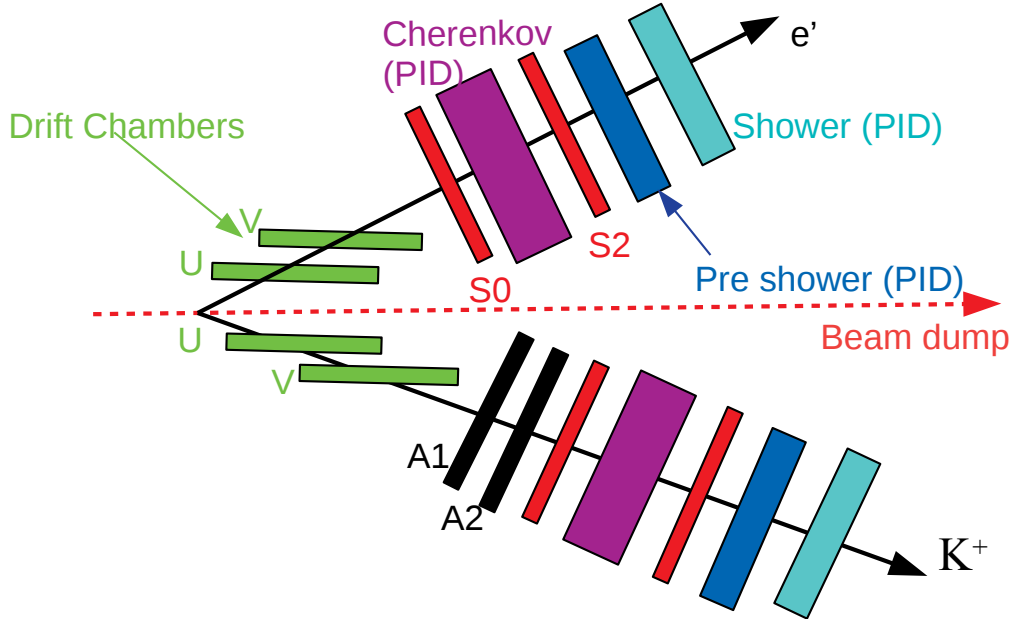


Figure 2.13. Schematic of a complete detector package for the E12-17-003 experiment.

wires. For any individual wire plane, the sense wires are equally spaced with a wire spacing of 4.24 mm. The sense wires are oriented plane by plane either at 45° or -45° with respect to the scattered particle trajectory. The sense wires located in two different planes are orthogonal to each other. Each of the wire plane is sandwiched between a pair of cathode planes which is connected to a high voltage of - 3500 V. A complete VDC has a box shape (see Fig. 2.14) with an active area of 2118 mm by 288 mm.

A gas mixture of argon (62%) and ethane (38%) is supplied to the chamber continuously. In this mixture the argon is the ionizing gas while the ethane is the quenching gas. Their ratio is optimized based on the operational stability and signal size. When a charge particle passes through the chamber, it encounters the gas molecule inside the gas chamber resulting ionization of the gas molecules along its trajectory. The resulting electrons and ions are accelerated by the electric field of the cathode plane producing secondary electrons. This process continues and results a localized cascade

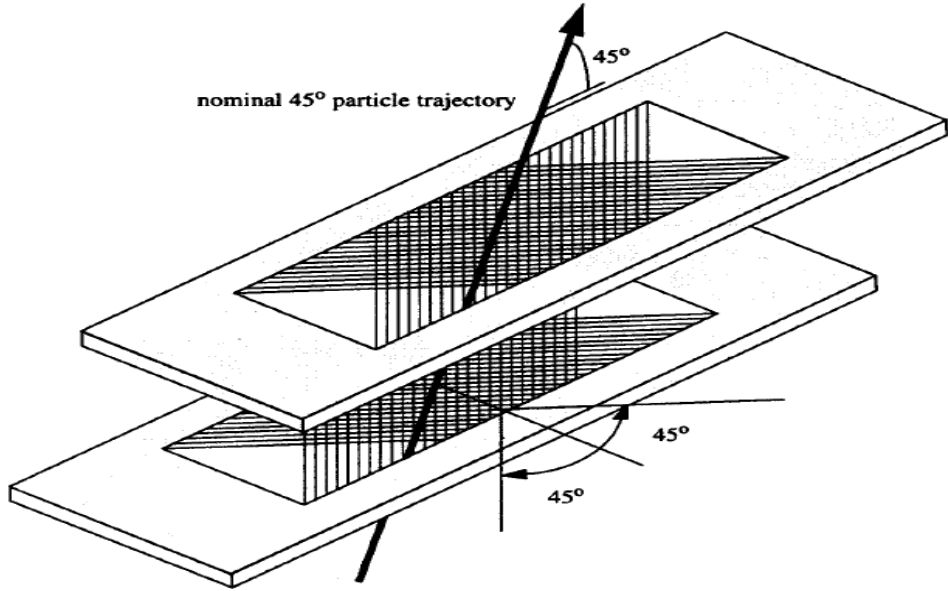


Figure 2.14. Schematic layout of a pair of VDCs used in the Hall A HRS detector package.

of electrons called electron avalanche. The electron avalanche move toward the closest sense wire and an electrical signal is generated in the sense wire.

The sense wire signal is then transmitted to the front end electronics, amplifier and discriminator. The amplifier discriminator cards are mounted on the chamber. Each card process 16 channels and producing output logical signal. Finally, the logical signal is sent to the time to digital converter (TDC) with the help of twist pair of ribbon cables. The TDC measures the timing of the signal which is referenced to the main event trigger. The time is called drift time which is converted to a perpendicular distance from the trajectory of the wire plane (the dot/dashed line in Fig. 2.15). The perpendicular distance is called the drift distance. Then, the local cross-over point Q_i and the local trajectory angle θ_{Qt} of the track is determined for each of the wire plane by performing a linear fit on the drift distances. The cross-over information from all of the wires planes is combined and the position and direction of the trajectory at

the first wire plane (focal plane) is determined. This setup can provide a position resolution of $100 \mu\text{m}$ and angular resolution of 0.5 mrad.

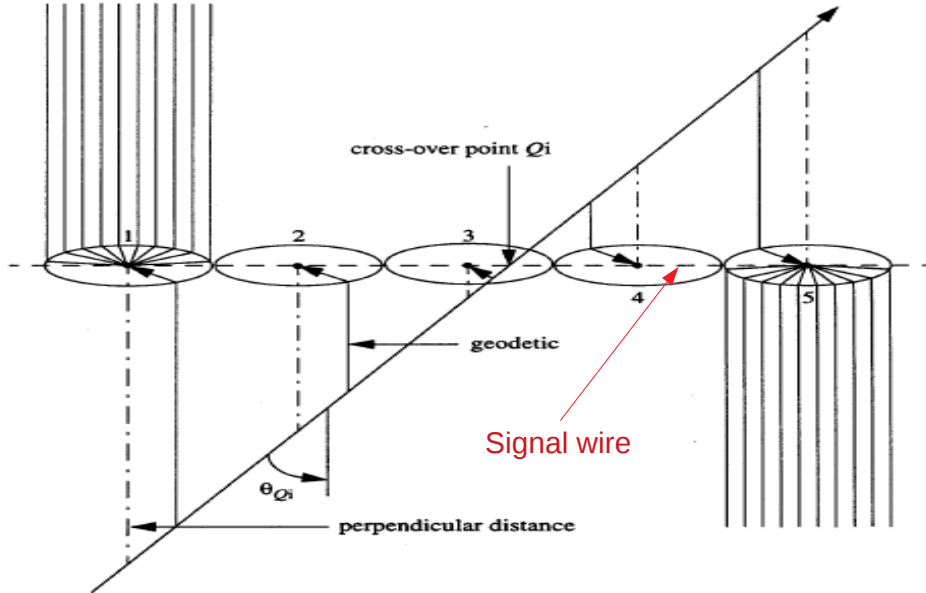


Figure 2.15. Schematic of a typical nominal track in the wire planes.

2.9.3 Scintillation Detectors

To account for the timing and triggering information of the scattered charged particles, two scintillator planes S0 and S2 are utilized in each HRS. For the $(e, e' K^+)$ experiment, the two scintillator planes were separated by about a meter distance and sandwiched a gas Cherenkov detector. The S0 scintillator contains a single paddle with one photo multiplier tube (PMT) at each end and placed along the dispersive plane. The S2 scintillator detector contains 16 isolated scintillator paddles with one PMT at each end of each paddle and placed in the non dispersive direction. In the S2 scintillator plane, each paddle overlaps to its neighbor by about 0.5 cm. The overlapping helps when the scintillator timing is aligned by considering one scintillator time as the reference. The layout of the two scintillators S0 and S2 is shown in Fig. 2.16.

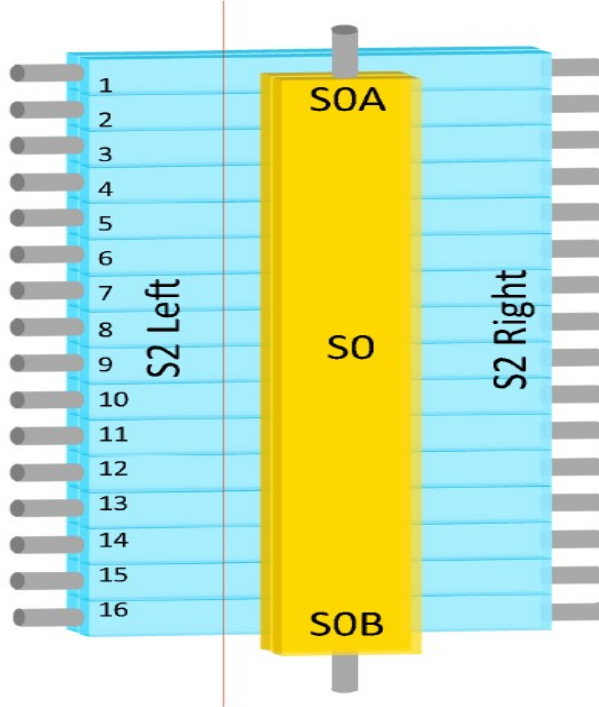


Figure 2.16. Schematic of the two scintillator planes S0 and S2 [6].

As discussed in the above section, each scintillation detector contains two parts, the plastic scintillator and two photo multiplier tubes, one mounted on each end. The PMTs are made of evacuated glass housing with a photo cathode, several electrodes called dynodes, and an anode. When an external charge particle passes through the scintillating material, it collides with the material of the medium and transmits energy to the medium. The material medium converts the absorbed energy into low energy photons. The more absorbed energy from the scattered charged particle, the larger the number of photons emitted. The emitted photons then travel through the material to the PMTs on each end and are detected by the PMTs which work on the principle of photoelectric effect. When a photon reaches to the PMT, it knocks out the electrons from the surface of the photo cathode. These electrons are the primary photo electrons which are accelerated through high voltage dynodes (focusing electrodes). As the electrons hit the surface of each dynode, the number of the electrons are multiplied by the process of secondary emission. Finally, the

number of electrons increases exponentially as they reach to the anode after sequence of dynodes and a signal is created in the form of electric pulse which can be read. The entire process is very fast and allowing the scintillator signals to be used for setting the time of events.

The signals from each PMT are processed by a discriminator which removes noise background signals by a voltage threshold. It generates standard logical signals from the PMT signals above the threshold. These logical signals from the scintillators are used to analyze timing of events through TDC measurements and form online event trigger based on the trigger logic combining needed signals from other detectors. The analog PMT signals are also analyzed by ADCs to correct the timing variations due to signal size and position variation.

2.9.4 Gas Cherenkov Detector

When high energy electron beam hits the target material, a number of different charge particles are produced and are scattered to the detector planes. The negatively charged particles travel towards the LHRs while the positively charged particles move towards the RHRs. However, the $(e, e'K^+)$ experiment consider only the electrons in the LHRs and coincidental K^+ s in the RHRs. To identify and separate the scattered electrons from the π^- s in the LHRs, a gas Cherenkov (GC) [60] detector was used in the LHRs. The GC was installed between the two scintillator planes S0 and S2. The same detector was also installed in the RHRs, however, it cannot be fired with the hadrons, therefore, the RHRs GC detector was not used in this experiment.

The GC is a rectangular tank filled with CO_2 gas at the atmospheric pressure. In the LHRs, the path length for a charge particle inside the GC is about 120 cm. When a charged particle like an electron travels inside the CO_2 gas (dielectric medium) with very high velocity, it polarizes and depolarizes the CO_2 molecules along its

trajectory. This process leads to an emission of intense coherent beam of radiation called Cherenkov radiation.

The Cherenkov light is emitted if the velocity (v) of the charged particle in the detector material is greater than a given threshold [61]. Mathematically,

$$v_{th} = c/n, \quad (2.9.1)$$

where, c/n is the velocity of light in the same medium and n is the refractive index of the medium (CO_2). Therefore, the threshold momentum will be:

$$p_{th} = \frac{mv_{th}}{\sqrt{1 - (\frac{v_{th}}{c})^2}}. \quad (2.9.2)$$

Since the refractive index of the CO_2 gas at the atmospheric pressure is 1.00041 which creates a momentum threshold of $0.01784 \text{ GeV}/c$ for electron, $4.873 \text{ GeV}/c$ for pions, and $32.76 \text{ GeV}/c$ for protons.

The GC contains 10 spherical mirrors, each having a focal length of 80 cm. The mirrors focus the Cherenkov light to 10 PMTs placed at the side of the detector box. The signals from the PMTs are then sent to the ADCs and then summed.

None of the hadrons can fire the Cherenkov as the threshold value is too high. Therefore, the GC is considered as the powerful tool for the electron identification with 99% efficiency. Sometime the pions can produce the Cherenkov radiation as they knockout the electrons with momentum higher than threshold and can create a dominant contamination. However, the knockout electrons have to satisfy the trigger conditions that is they should fire both scintillators ($S0$ & $S2$) to produce the Cherenkov light. This limits the contamination to a very small number (10^{-3}). The GC calibration [62] was done during the E12-10-103 (MARATHON) experiment which allow the $(e, e'K^+)$ experiment to use the calibrated detector.

2.9.5 Aerogel Cherenkov Detector

To identify and separate the K^+ s from the huge hadronic background in the RHR_S was a great challenge. To solve this problem, a pair of aerogel diffusion type detectors A1 and A2 were installed in the RHR_S next to the VDCs. These detectors are based on the detection of Cherenkov radiation discussed in the previous section. The A1 and A2 detectors played a role of particle identification (PID) detectors in the RHR_S and helped to select the coincidental K^+ s for offline data analysis. The two Aerogel detectors used in the ($e, e' K^+$) experiment are shown in Fig. 2.17.

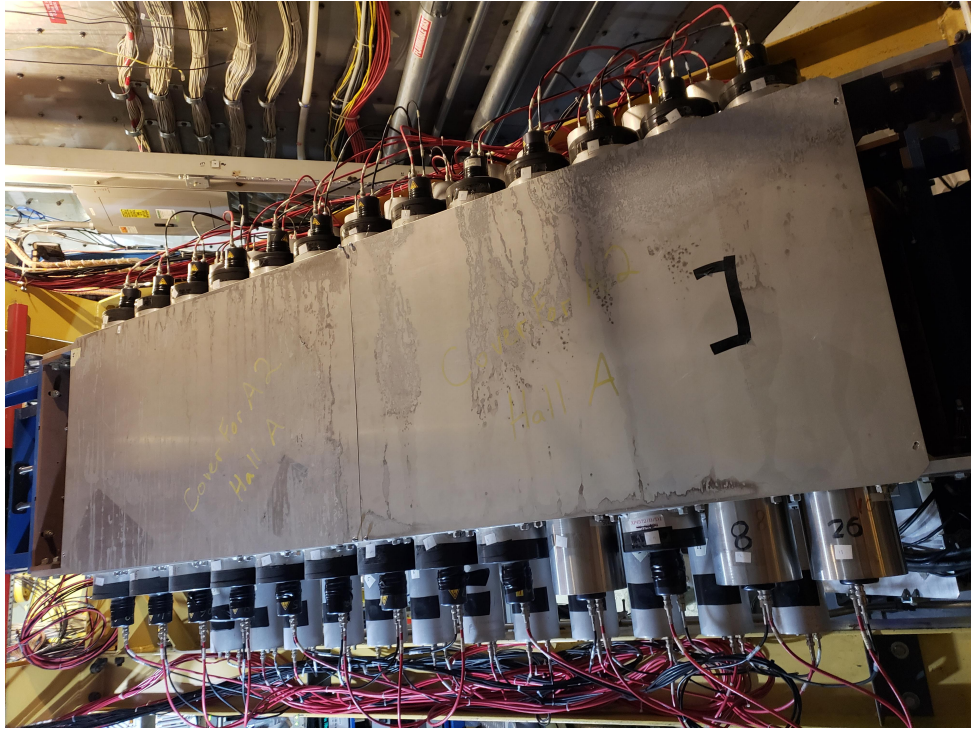


Figure 2.17. Top view of the two Aerogel detectors A1 and A2 in the detector stack.

Each of the detector is made of an aluminum box containing silica aerogel with two rows of PMTs placed on two sides. To minimize the photon loss, most of the internal surface of the detector is covered by reflecting material. To avoid the possible

Table 2.3

The main characteristics of the A1 and A2 detectors with their threshold momentum.

| Detector | Index of refraction | Radiator size [cm ³] | Number of PMTs | β_{th} | pion Gev/c | kaon GeV/c | proton GeV/c |
|----------|---------------------|----------------------------------|----------------|--------------|------------|------------|--------------|
| A1 | 1.015 | 170×32×9 | 24 | 0.985 | 0.8 | 2.8 | 5.4 |
| A2 | 1.055 | 192×30×5 | 26 | 0.948 | 0.4 | 1.5 | 2.8 |

light leakage, an O-ring is inserted between the radiator box and light diffusion box. 24 5" Burle RCA 8854 PMTs are used for the A1 detector while 26 5" Photonics XP4572B PMTs for A2. The index of refraction for A1 and A2 is 1.015 and 1.055, respectively. This creates the K^+ momentum threshold for A1 and A2, 2.8 GeV/c and 1.5 GeV/c, respectively. For the current experiment, the RHRSS momentum was about 1.8 GeV/c, the K^+ s can fire only A2 detector. Additional details about the two Aerogel Cherenkov detectors are summarized in Table 2.3 [63]. The three main hadrons produced in the ($e, e'K^+$) reaction and whether or not they fire the two Aerogel detectors are summarized in Table 2.4.

Table 2.4

The A1 and A2 detector response when hadrons pass through them. Here, 1 means fired and 0 means not fired.

| Hadrons | A1 | A2 |
|---------|----|----|
| π^+ | 1 | 1 |
| K^+ | 0 | 1 |
| proton | 0 | 0 |

2.9.6 Calorimeters

To provide the additional particle identification for the scattered charged particles, two additional PID detectors were installed in each HRS. These are the last detectors in each HRS with which the charged particle interact. These are the lead glass calorimeters called preshower (PS) and shower (SH) detectors. In the LHRs, both of the calorimeters (PS and SH) contains 34 SF-5 lead glass blocks positioned perpendicular to the path of the particles and each block is connected to a PMT. The dimension of LHRs PS and SH are $15 \times 15 \times 30 \text{ cm}^3$ and $15 \times 15 \times 35 \text{ cm}^3$, respectively. The RHRs calorimeter configuration is slightly different than that of the LHRs configuration. In the RHRs, PS contains 48 TF-1 lead glass blocks placed perpendicular to the path of the particle where as SH contains 80 SF-5 lead blocks placed parallel to the path of the particle and each block is connected to a PMT. The dimension of RHRs PS and SH are $10 \times 10 \times 35 \text{ cm}^3$ and $15 \times 15 \times 35 \text{ cm}^3$, respectively. The calorimeters used for the tritium experiments are shown in Fig. 2.18.

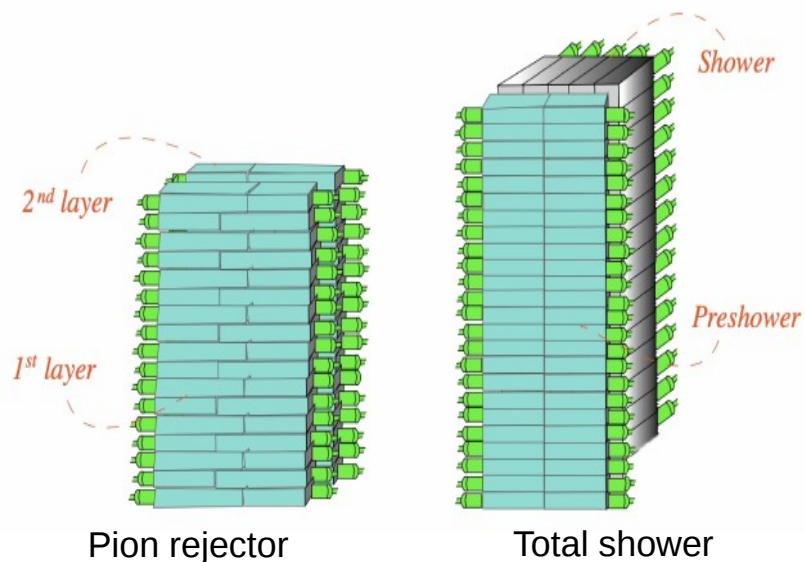


Figure 2.18. Schematic of the calorimeters for LHRs (left) and RHRs (right) [7].

When high energy charged particles like electron hit the lead glass material, the kinetic energy of the charged particle is absorbed by the material. In this process, photons are produced through the Bremsstrahlung process. These photons are converted into electron-positron pairs which further emit the Bremsstrahlung photons. This process continues until the energy of all of the produced electron-positron pairs drops below a threshold of about 15 MeV. During this course, Cherenkov light is produced and is collected by PMTs and then measured by ADCs. The higher the energy of the charged particle, more Cherenkov light will be produced and vice versa. Since the probability of Bremsstrahlung emission is inversely proportional to the square of the particle mass, the light particles (such as electrons and positrons) deposit most of their energy to the calorimeters. However, the heavier particles like pion or muon can deposit only a small fraction of their energy to the calorimeters.

For the PID measurements a measure of E/p is used, where E is energy deposited to the calorimeter and p is the momentum can be obtained by particle tracking. This method provides a reliable particle identification. For light particles like electron, the peak forms around 1, however, for higher mass particles the peak appears at lower region according to the mass of the particle.

2.10 Data Acquisition System

To handle the data collection during the execution of the experiments in a safe and controlled way, Jefferson Lab data acquisition group developed the Hall A data acquisition (DAQ) [64] system called CODA (CEBAF On-line Data Acquisition System). The CODA [65] is the combination of both software and hardware and is capable to monitor the data for online as well as offline analysis. The commercially available electronics used as hardware in the Hall A DAQ system which mainly consists of front-end fastbus and VME digitization devices with ADCs, TDCs, and scalers. Besides that the DAQ hardware is also housed with single-board VME-computers with

Unix and Linux work stations and a mass storage tape Silo (MSS) for data storage. The tape has huge storage and is capable to store all data for online as well as offline analysis.

In addition, the JLab DAQ group developed the central point for DAQ as the Trigger Supervisor (TS) together with Trigger Interface (TI) boards, Trigger Distribution Boards (TD), and Signal Distribution Boards (SD) which can distributes the triggers and synchronous clock source to the front-end electronics. The DAQ system software mainly consists of:

- Readout Controller (ROCs): The ROC runs at the front-end crates and receives triggers from the trigger supervisor, execute the corresponding readout list, structure the information, and finally pass that information to the next CODA component which is Events Builder.
- Events Builder (EB): The EB collects the information from different ROCs via network connection and merge the data into the data stream of the same events.
- Events Recorder (ER): The accepted events are recorded by ER and stored in a local disk and finally transported to the mass storage system.
- Events Transfer (ET): The additional information, for example, the EPICS [66] data and the scaler data are inserted in the data stream in every few seconds with the help of ET.
- The Run Control Process : The run control process allow the user to start and stop the runs and change the parameters as required.

2.11 Triggers

Since E12-17-003 is a coincidence experiment, three main triggers were generated for the data analysis. For the $(e, e'K^+)$ experiment, the calibration data were taken in the single arm trigger mode. The two single arm triggers were generated (one for each HRS) to analyze the single arm trigger data. For the coincidence data analysis, a separate coincidence trigger in the coincidence mode was built. The two scintillator planes S0 and S2 were used to form the triggers. To define a single arm trigger, a possible event must have both S0 and S2 detectors fired. The S0 scintillator has only

one paddle which was viewed by each paddle of S2 plane. The S2 signal is formed by local OR of 16 S2 paddles. Therefore, for the individual arm data analysis, the triggers were formed by logical AND of S0 and S2 (see Fig. 2.19). That is,

$$T1_{LHRS} = (S0 \& S2)_{LHRS}, \quad (2.11.1)$$

$$T4_{RHRS} = (S0 \& S2)_{RHRS}. \quad (2.11.2)$$

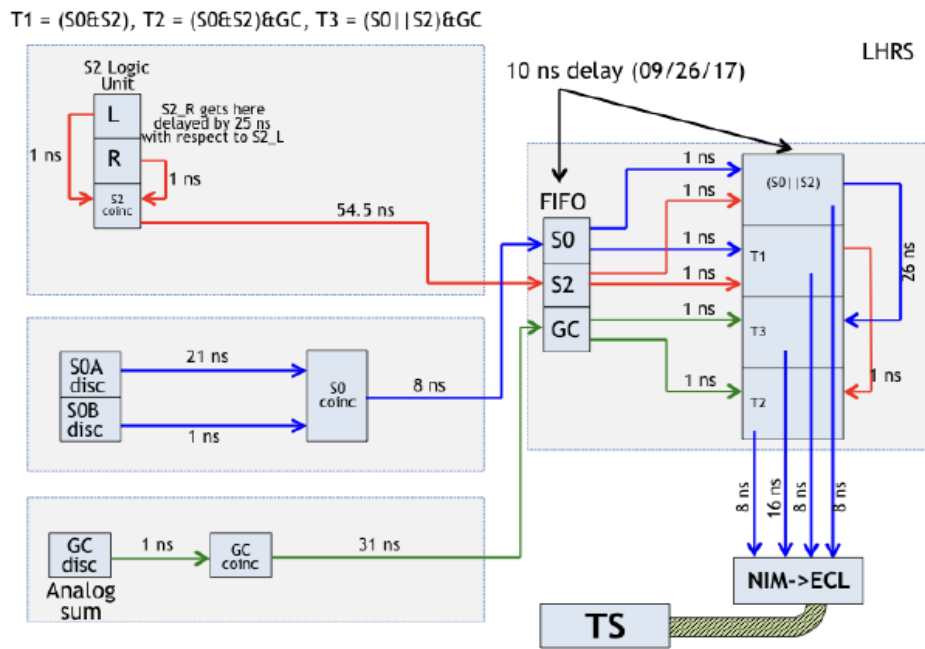


Figure 2.19. Schematic of the single arm (LHRS) trigger setup [8].

The coincidence trigger was formed between the two arms, LHRS and RHRS. That means when an electron is fired on the LHRS it should have a coincidence K^+ on the RHRS. Thus the coincidence trigger was formed by taking the logical AND between the triggers T1 and T4. The mathematical form of coincidence trigger is,

$$T5 = (T1 \& T4) = (S0 \& S2)_{LHRS} \& (S0 \& S2)_{RHRS}. \quad (2.11.3)$$

Some more details about the $(e, e'K^+)$ triggers are summarized in Table 2.5.

Table 2.5

Summary of E12-17-003 triggers. The symbol “&” represents the logical “AND” gate.

| Trigger | Label | Trigger logic |
|-------------|-------|---------------------------|
| LHRS | T1 | $(S_0 \ \& \ S_2)_{LHRS}$ |
| RHRS | T4 | $(S_0 \ \& \ S_2)_{RHRS}$ |
| Coincidence | T5 | $(T1 \ \& \ T4)$ |

The z -vertex and HRS angles matrices were optimized with the single arm trigger (T1 and T4) where as the HRS momentum matrices were optimized with the coincidence trigger (T5). The physics analysis was done with the coincidence trigger as the data were taken under the coincidence trigger mode.

CHAPTER 3

DATA ANALYSIS AND SYSTEM OPTIMIZATION

3.1 Data Collected

The experimental data were collected in November 2018 in the experimental Hall A at Jefferson Lab. Since the experiment was in the coincidence mode, both of the spectrometers were used to collect the experimental data. The LHRS was kept under negative polarity and used to detect the scattered electrons where as the RHRS was kept under positive polarity and used to find the K^+ s.

The E12-17-003 is a high precision experiment, anything that influence the system need to be optimized as much as possible. Therefore, the data were taken with different targets and different kinematic conditions. A lot of calibration data were taken to calibrate the system. The calibration data were taken with the H target and H kinematics (see Table 2.1) where as the production data were taken with the tritium target and tritium kinematics (see Table 2.1). The beam energy was kept fixed at $4.326 \text{ GeV}/c$ during the whole data taking period. The $(e, e'K^+)$ was the last tritium experiment, therefore, most of the detector systems such as BPM, BCM, raster, the gas Cherenkov detector (LHRS), the calorimeters, and the high voltage for all of the detectors were optimized prior to the experiment. In addition, two Aerogel detectors were installed to the right arm as the PID detectors which were optimized prior to the experiment.

3.2 Data Analysis Overview

When charged particles from the target passed through the spectrometer system and the trigger conditions were met, data is generated which is recorded in the form

of raw data that contains various digitized information, such as trigger type, TDC, ADC, and beam related information. The raw data was then decoded by the Hall A analyzer [67] and the TDC and ADC type of information was changed into the physical information. During this part of analysis, the raw data was first decoded and written into a root file which can be read by subsequent analyzers. This originally generated root files had very large size as they contained a lot of information. They occupied large amount of space on the storage disk and also took significant amount of time for carrying out the detailed data analysis. Therefore, the size of the original root files were reduced to small root files by applying some loose cuts which are sufficient to remove most of the obvious “junk”, unphysical, or unnecessary information. The reduced root files were used in the later part of analyses including various optimizations such as tracking, timing, particle identification, and all the needed reconstruction matrices, missing mass calculation for the mass spectroscopy analyses. Figure 3.1 shows the approximate analysis procedure of this experiment.

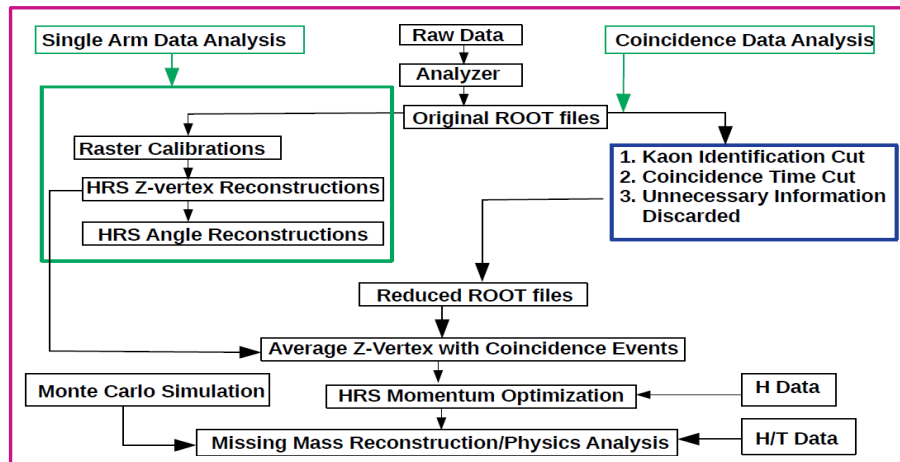


Figure 3.1. Schematic of the flow chart of the E12-17-003 data analysis.

3.3 Coordinate System

To do the various calibrations and to analyze the data in a convenient way, the experimental Hall A has five different coordinate systems. A short overview of each of them is discussed in this chapter. A more detailed description of each of the coordinate system can be found in Ref. [68].

3.3.1 Hall Coordinate System

To make convenient for the operation of beam delivering and monitoring, a coordinate system called Hall Coordinate System (HCS) is defined. The origin of the HCS is the point of intersection between the beam line and the vertical symmetry of target system with \hat{z} along the beam line towards the beam dump and the \hat{y} axis is pointing vertically in the upward direction. This suggested the \hat{x} direction as $\hat{x} = \hat{y} \times \hat{z}$. The HCS is shown in Fig. 3.2.

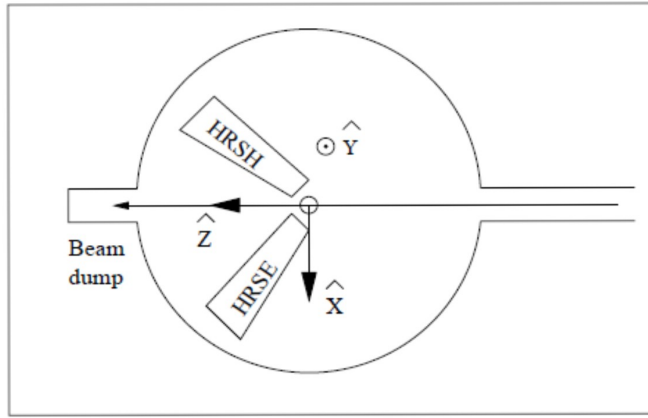


Figure 3.2. Schematic of the Hall Coordinate System (top view).

3.3.2 Target Coordinate System

To make convenient for the momentum and incident angle analyses, each spectrometer defines its own coordinate system known as the Target Coordinate System

(TCS) (see Fig. 3.3) which moves along with the spectrometer. The \hat{z} axis of the TCS is along the central ray of the spectrometer and passing through the mid point of the central sieve slit hole. For the TCS, the \hat{x} axis points vertically downwards crossing the center of the sieve slit plane. Therefore, the \hat{y} direction points in the perpendicular direction of x-z plane, that is $\hat{y} = \hat{z} \times \hat{x}$. With this definition, the out-of-plane angle θ_{tg} and the in-plane angle ϕ_{tg} of the particle trajectory in the TCS are defined as:

$$\tan \theta_{tg} = \frac{dx}{dz}, \quad (3.3.1)$$

$$\tan \phi_{tg} = \frac{dy}{dz}. \quad (3.3.2)$$

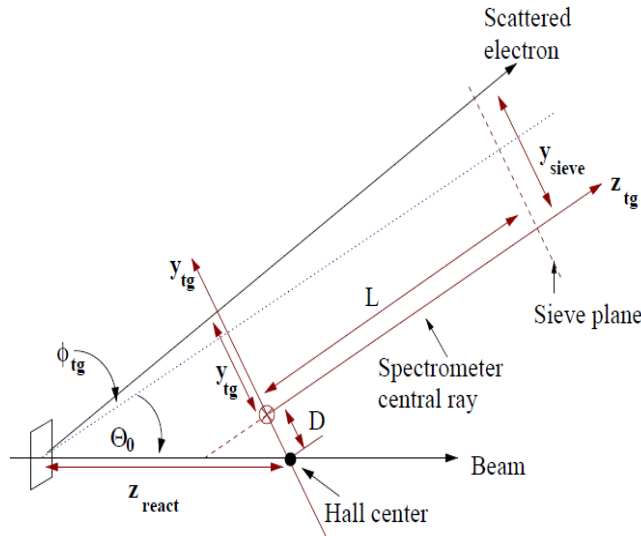


Figure 3.3. Schematic of the Target Coordinate System. L represents the distance from the hall center to the sieve plane. D is the horizontal displacement of the spectrometer axis from the ideal position.

3.3.3 Detector Coordinate System

To define the position and direction of the trajectories at the focal plane, the Detector Coordinate System (DCS) is defined. The origin of this coordinate system is given by the intersection of wire 184 of VDC1 U1 plane and the perpendicular projection of wire 184 in the VDC1 V1 plane on to the VDC1 U1 plane. In this coordinate system, the \hat{z} direction is perpendicular to the VDC plane pointing vertically upward direction, \hat{y} is parallel to the short symmetry axis of the lower VDC (see Fig. 3.4 (a)) and \hat{x} is along the symmetry axis of the lower VDC (see Fig. 3.4 (b)).

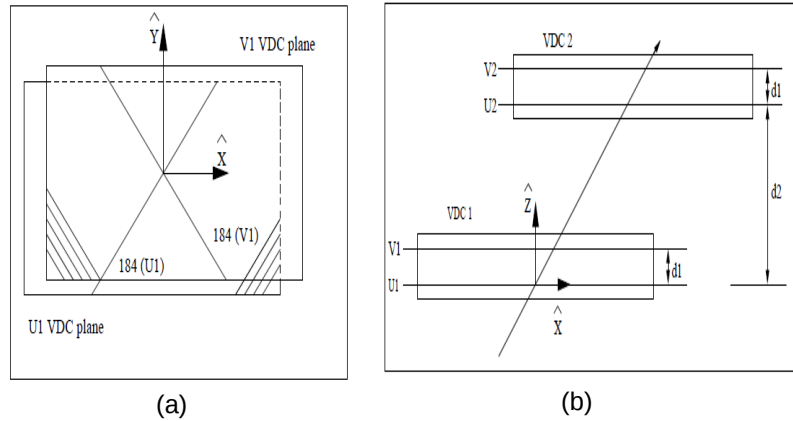


Figure 3.4. Schematic of (a) top view of the Detector Coordinate System and (b) side view of the Detector Coordinate System.

3.3.4 Transport Coordinate System

The Transport Coordinate System (TRCS) at the focal plane is obtained by rotating the DCS clockwise around its \hat{y} axis by 45° . The TRCS is shown in Fig. 3.5.

3.3.5 Focal Plane Coordinate System

The focal plane coordinate system (FCS) is used to transport an event's track information from the DCS to the TCS. To obtain the FCS, the DCS is rotated around

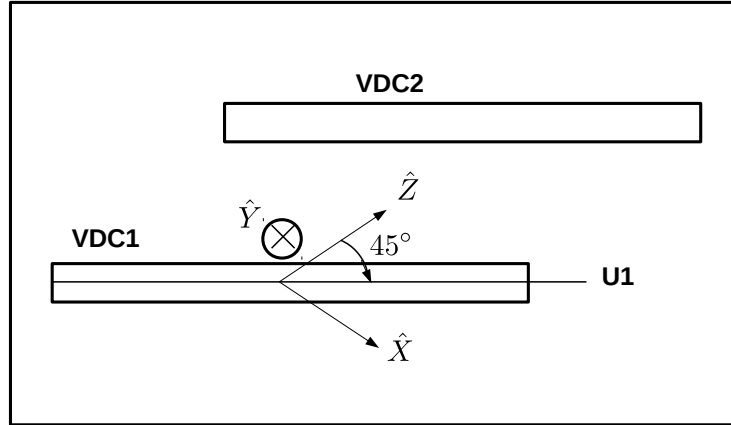


Figure 3.5. Schematic of side view of the Transport Coordinate System.

the \hat{y} axis by an angle ρ , where ρ is the angle between the local central ray and \hat{z} axis of DCS. The local central ray is defined as a ray for which $\theta = \phi = 0$ for the corresponding relative momentum $\frac{\Delta p(\delta)}{p}$. The main feature of the FCS is that the dispersive angle θ is small for all points across the focal plane. Therefore, the expressions for reconstructed vertex converge faster during the optics calibration. The FCS is shown in Fig. 3.6.

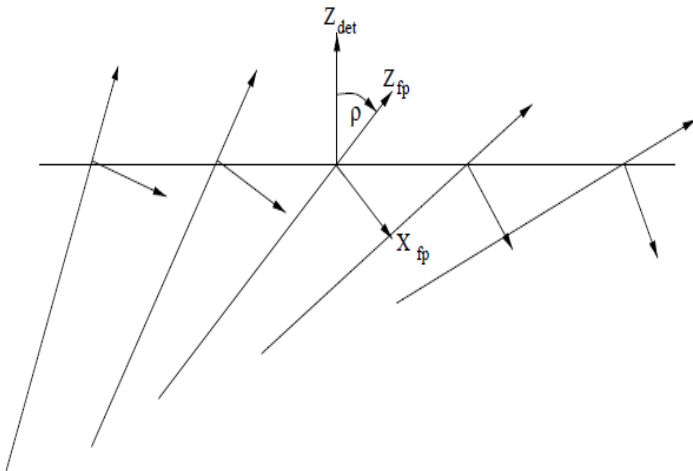


Figure 3.6. Schematic of the focal plane (rotated) coordinate system.

In DCS, the information for x_{det} , y_{det} , θ_{det} , and ϕ_{det} are measured by VDC. These variables are corrected for the detector offsets from the ideal central ray of the spectrometer to obtain x_{fp} , y_{fp} , θ_{fp} , and ϕ_{fp} at FCS by using a transform formula. The transform formula can be found in Ref. [68]. These quantities are used to calculate the x_{tg} , y_{tg} , θ_{tg} , ϕ_{tg} , z_{tg} , and δ in the Target Coordinate System. The θ_{tg} , ϕ_{tg} , and δ are generally represented by $x'(\theta)$, $y'(\phi)$, and p , respectively.

3.4 K^+ Identification

When beam electrons interact with the target nuclei, different hadrons were produced by the $(e, e'K^+)$ reaction. The positively charged hadrons were transported to the RHR_S detector system. These hadrons were protons, π^+ s, and K^+ s. The E12-17-003 experiment strongly required the clean separation of K^+ s by rejecting the rest of the hadrons. To separate the K^+ s from the rest of the hadrons, two low index Aerogel detectors A1 and A2 were installed in the RHR_S detector hut. The details about the Aerogel detector was discussed in the previous chapter (see Section 2.9.5).

Both of the Aerogel detectors were calibrated before the $(e, e'K^+)$ run period. In order to get the best response, each PMT was provided a unique (suitable) high voltage and therefore, each PMT has a unique gain factor. A common reference was given to all PMTs so that each of them has identical gain and all PMTs were adjusted to the common reference. The signals from PMTs were readout by flash ADCs and the number of ADC channel was proportional to the signal size from each PMT. Finally, a sum of ADCs from all the PMTs from each Aerogel detector for each event was made to form the Aerogel Cherenkov sum which was used to identify the hadrons. The ADC sum of each Aerogel detector is shown in Fig. 3.7.

The index of refraction for A1 and A2 is 1.015 and 1.055, respectively. This allows for the given momentum range, A1 can be fired with π^+ s only and A2 can be fired with π^+ s and K^+ s, while, proton cannot fire any of the aerogel detectors.

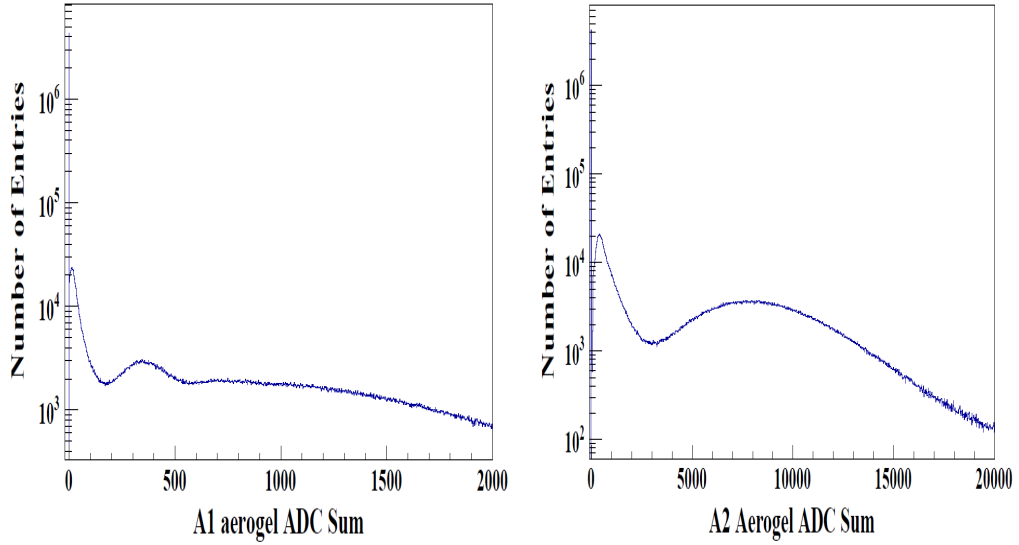


Figure 3.7. Schematic of the Aerogel A1 ADC sum (left) and the Aerogel A2 ADC sum (right).

The ADC sum provided by A1 detector indicated that π^+ s belong to the region approximately above 200. Therefore, by selecting a region below 200 in the A1 ADC sum, the π^+ s are rejected. That means only protons and K^+ s are selected from this region of A1. Similarly, the ADC sum provided by Aerogel A2 indicated that π^+ s and K^+ s belongs to the region approximately above 1500. Thus, by selecting the A2 ADC sum above 1500, the π^+ s and K^+ s are selected. However, the π^+ s were already rejected by A1. Therefore, only K^+ s are selected from this region. Unfortunately, both of the Aerogel detectors were about 20 years old and therefore, none of them can reject 100% of the protons and π^+ s. Therefore, the cut conditions for the ADC sum from A1 and A2 were extensively studied to determine the best ones for maximizing the number of K^+ s, although they did not minimize the background π^+ s and protons. In addition, the correlations between the coincidence time and A1 and A2 ADC sum were plotted (see example for A2 in Fig. 3.8) and studied which also helped to maximize the number of K^+ s.

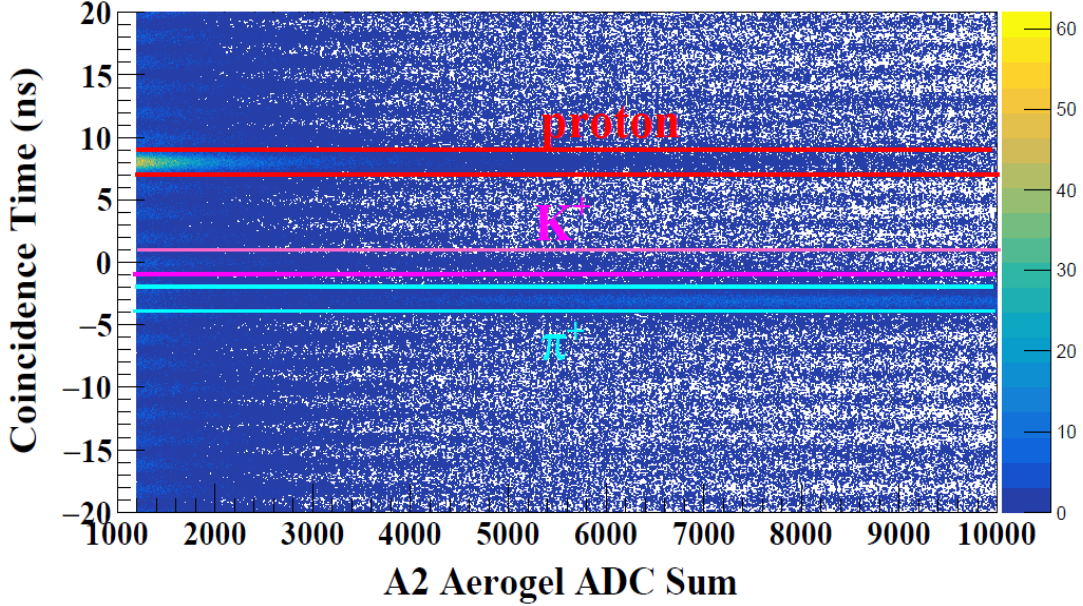


Figure 3.8. Correlation between the coincidence time(ns) and the A2 Aerogel ADC sum. The background is seen because of the inefficiency of the Aerogel detector.

3.5 Electron Identification

The scattered electrons (e') were transported to the LHRS. However, π^- s were also produced and transported to the electron arm. They are the main background to the scattered electrons. A gas Cherenkov detector was installed in the LHRS to select the scattered electrons by rejecting the π^- s. A detailed description of the gas Cherenkov detector was discussed in the previous chapter (see Section 2.9.4).

Before the E12-17-003 experiment, several tritium experiments were performed in the experimental Hall A and all of them used the LHRS to detect the scattered electrons. Therefore, all of the detectors in the LHRS including the gas Cherenkov detector were calibrated very well before the $(e, e' K^+)$ run period. Just like the Aerogel detectors, the calibrated gas Cherenkov detector also used one common ADC reference to all PMTs, so that all of them can be adjusted to the common reference. Again, for all PMTs, a sum of Cherenkov ADC signals for each event was made to

form the Cherenkov ADC sum. The Cherenkov ADC sum is shown in Fig. 3.9 which was used to separate the scattered electrons from the π^- s.

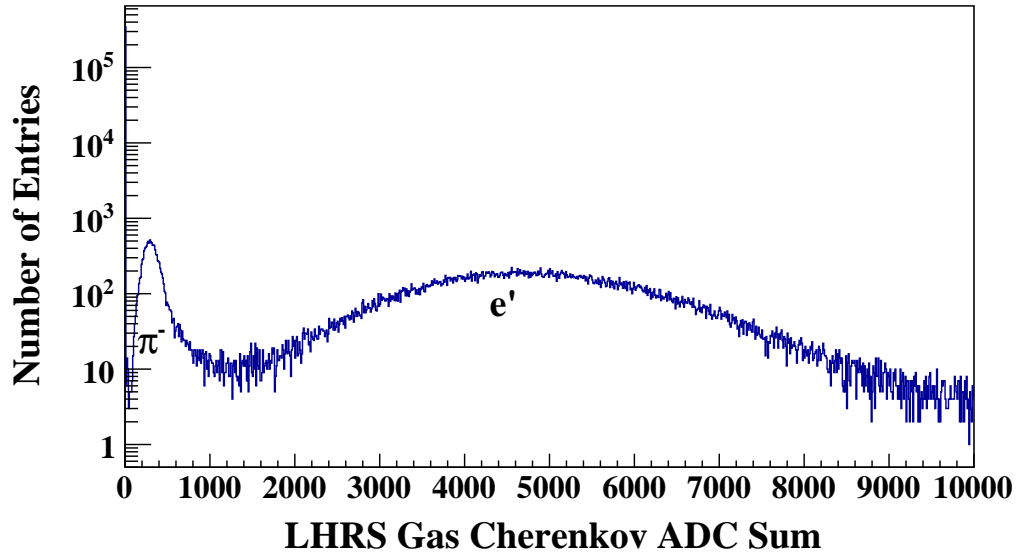


Figure 3.9. The LHR Gas Cherenkov ADC sum.

Since the π^- s cannot fire the gas Cherenkov detector at the momentum of 2.2 GeV/c (the threshold momentum for π^- is 4.8 GeV/c), therefore they belong to the lower region (Cherenkov ADC sum < 500) of the pedestal as shown in Fig. 3.9.

3.6 Coincidence Time

The coincidence time (CT) between the LHR and RHR is defined as the time of flight (TOF) difference between the scattered electrons and K^+ s created at the same reaction vertex. For a perfectly calibrated system, a CT spectrum should show a sharp peak at zero nanosecond (ns). In case of the E12-17-003 experiment, the coincidence time was optimized by assuming the kaon mass in a calculation of particle speed, therefore, the K^+ s peak was formed at 0 ns. Since the coincidence time for different hadron is different, therefore, CT can be used as a powerful tool for particle identification technique to remove the unnecessary hadrons in the RHR. For the $(e, e' K^+)$ experiment, the CT is defined as:

$$\text{Coincidence Time} = (RF - S2L_{mean})_{LHRS} - (RF - S2R_{mean})_{RHRS}, \quad (3.6.1)$$

where, RF is the radio frequency signal provided by MCC which characterizes the beam bunch timing. It was recorded in TDCs relative to the single arm trigger and having structure of sharp peak in every 2 ns. That means each small peak is a beam bunch separated by 2 ns in the CT spectrum. The $(RF - S2L_{mean})_{LHRS}$ and $(RF - S2R_{mean})_{RHRS}$ represent the TOF between the reaction time and arrival time given by the optimized S2 time, with a time offset. For a coincidence event, the time offset is same for both. The coincidence time was optimized by considering the following factors:

- Path length variation from the finite angular acceptance.
- Velocity variation from the momentum acceptance of the RHRs.
- Time variation from S2 influenced by hit position and pulse size variation.
- Time offsets between the segmented S2 detectors due to cable and electronics delay variations.

To obtain the best achievable coincidence time, the $S2L_{mean}$ and $S2R_{mean}$ were calibrated with the K^+ 's time. The S2 detector contains 16 overlapping paddles and each paddle has one PMT at each end. By taking the mean time of the relative timings (to the common trigger time) from the two PMTs on the two ends, the influence of the hit position variation was minimized. Using the correlation with the ADCs, the pulse size variation influence was also minimized. By selecting the events that passed through the overlap region between two adjacent S2 counters, the cable and electronics delay variations were calibrated by referencing to the center paddle. Then with the help of the equation 3.6.1, the coincidence time was obtained. Finally, using the correlations between the coincidence time and focal plane x and x' , the

path length and velocity variations were minimized for K^+ s. As shown in Fig. 3.10, a timing resolution of 355 ps was achieved for the K^+ s. Because of the mass differences, the real coincident π^+ s and protons due to imperfect KID are separated from K^+ s by about 3 ns ahead and 8 ns behind, respectively. The small accidental peaks separated by 2 ns are formed by the accidental coincident events from pions and protons. For the physics data analysis only K^+ s were selected by selecting the ± 1 ns coincidence time window about 0 ns.

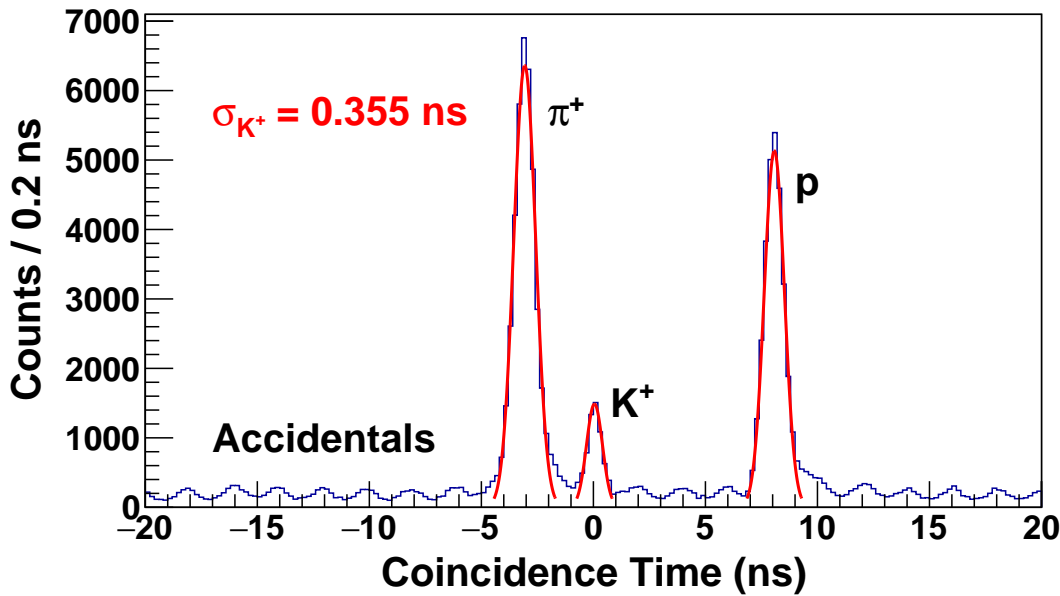


Figure 3.10. The coincidence time between LHRS (e') and RHRs (K^+).

3.7 Background Source

The trigger events generated during the course of reaction other than the reaction under study are considered as the background events. The electromagnetic interactions produce large amount of charged particles (scattered electrons and variety of hadrons predominantly than leptons) in the E12-17-003 configuration. The charged particles produced at the target were transported to the detectors with the help of the spectrometers. Since the LHRS required only the scattered electrons and RHRs

required the coincidental K^+ s, the rest of the hadrons (such as π^+ s and protons from RHRS and π^- s from LHRs) registered by the detector systems provide the background for the $(e, e' K^+)$ data analysis. This is because that the E12-17-003 did not apply PID for the online triggers, due to very low single rates (< 100 Hz) from both the LHRs and RHRS. Since the gas was contained in an aluminum cylinder having the aluminum windows for the beam entrance and exit, the events from the aluminum windows contribute for the background as the analysis required the events from the pure gas region. Since the experiment used an extended target, the coincident triggers contained the spatial accidental background events (i.e. the e' and K^+ were not from the same target position). Finally, since the coincidence time window was set to be about 100 ns wide to make the coincidence trigger, so that there were background events with accidental time coincidence contained in the raw data. These backgrounds were minimized by the following offline analysis processes:

- For the LHRs, ADC cuts were applied to the gas Cherenkov detector and the shower counters to minimize the background from π^- s, as described previously.
- For the RHRS, optimized cuts were applied to Aerogel Cherenkov detectors A1 and A2 to separate K^+ s from the rest of the hadrons (π^+ s and protons), as described previously.
- Single arm timing with respect to RF time by the S2 detector was separately optimized for the LHRs and RHRS. Then coincidence time was optimized to remove the path length and velocity dependences based on the K^+ mass. Then a ± 1 ns cut was applied to reduce the coincidence time window to 2 ns, corresponding to only a single beam pulse. This cut removed the real coincidence background from π^+ s and protons and the accidental background outside the 2 ns coincidence time window. This was discussed previously.
- The z -vertex reconstruction was optimized separately for the LHRs and RHRS. Backgrounds were minimized by applying cuts on their difference and average. This will be discussed in the following.

3.8 The Cuts Related to the Z-Vertex

Various cuts were applied to minimize the background. All of them were discussed previously, except those for the z-vertex which will be discussed here.

Cuts Used for the Z-Vertex Optimization

The z -vertex was optimized with the data taken from the carbon multi-foil target using the single arm triggers. A detailed discussion on the z -vertex optimization procedure will be discussed in the coming section. In addition to the particle identification cuts discussed previously, cuts on the focal plane parameters were also applied and they were:

1. $\text{abs}(x_{fp}) < 2.0$,
2. $\text{abs}(x'_{fp}) < 0.1$,
3. $\text{abs}(y_{fp}) < 0.5$,
4. $\text{abs}(y'_{fp}) < 0.1$,

where, x_{fp} and y_{fp} are the focal plane variables in meter and x'_{fp} and y'_{fp} are the tangent of the track angles θ and ϕ , respectively. These cuts were also used to select the events for the optimization of the angle (θ and ϕ) reconstructions.

Average Z-Vertex Cut

To analyze the coincidence data, the average z -vertex was used to improve the vertex resolution. It was obtained by averaging the two separately reconstructed z 's. That is:

$$z\text{-average} = \frac{z\text{-LHRS} + z\text{-RHRS}}{2}. \quad (3.8.1)$$

For the physics analyses, the averaged z -vertex cut from -10 cm to +10 cm was used. The events within this region were considered to be the events from the gas region.

The Z -Vertex Correlation Cut

The correlation between the reconstructed LHRS z -vertex and RHRS z -vertex is shown in Fig. 3.11. The events contained in the diagonal correlation were spatially coincident events recognized by LHRS and RHRS. The events located outside this correlation were the spatial accidental events, in which the two particles recognized by LHRS and RHRS were not from the same spatial location. The difference of the two independently reconstructed z vertexes was found to be a good tool to remove most of these background events (see Fig. 3.12). The applied cut was:

$$\text{abs}(\text{LHRS } z\text{-vertex} - \text{RHRS } z\text{-vertex}) < 0.053 \text{ m.}$$

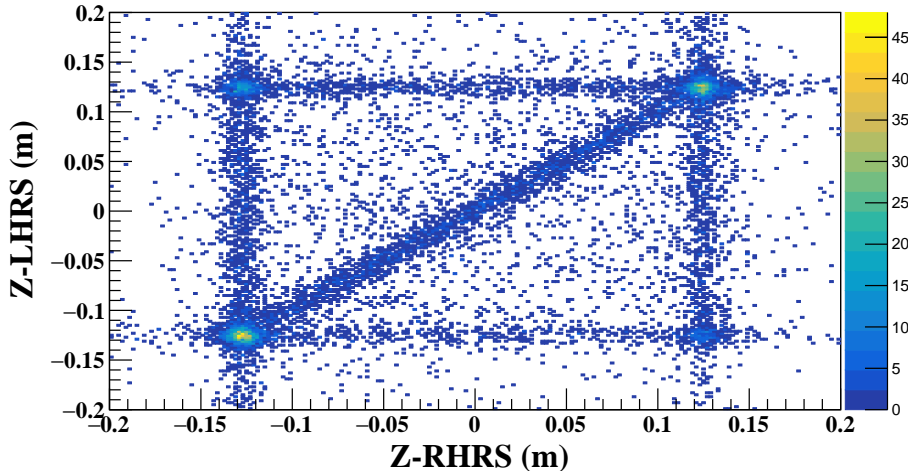


Figure 3.11. The correlation between the LHRS z -vertex and RHRS z -vertex. The events along the diagonal line corresponds to the real events from the gas region.

Aluminum Gate Cuts

In the later part of the momentum calibration, aluminum data was involved in the matrix tune (which will be discussed in the coming section). The aluminum events were selected from the following two regions:

1. Average z -vertex > -0.14 m and average z -vertex < -0.11 m.
2. Average z -vertex > 0.11 m and average z -vertex < 0.14 m.

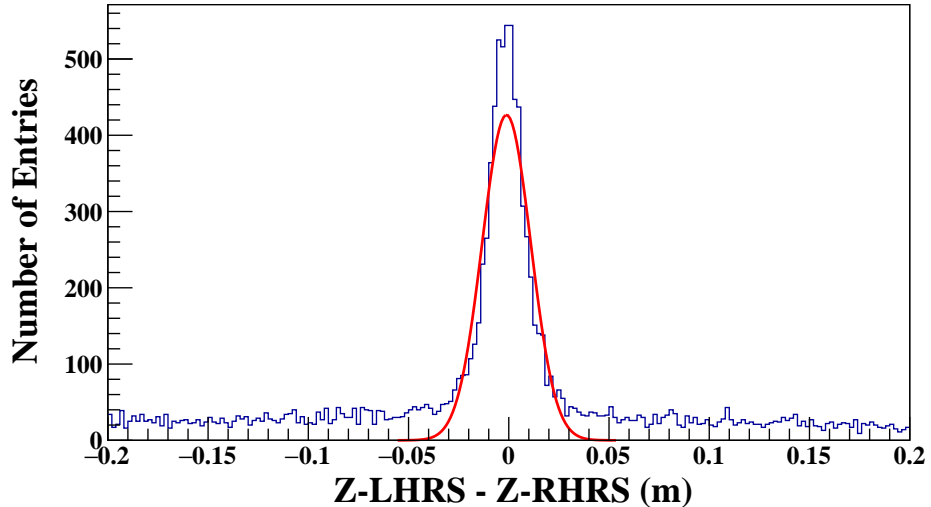


Figure 3.12. The difference between two z -vertexes (z -LHRS and z -RHRS).

Cuts for Estimation of the Accidental Background

The accidental events within the ± 1 ns coincidence time window cannot be identified and removed. These events will form a background distribution in the physical mass spectroscopy (see later discussions). The shape of this background represents the combined kinematic (momentum and angular) acceptance. To make a precise evaluation on the shape of this background, events from 38 accidental peaks were selected to make a missing mass analysis with sufficiently high statistics. Then the precise background distribution could be obtained by divided by 38. The cuts for these 38 accidental peaks were from the two regions in the coincidence time spectrum:

1. CT > -49.39 ns and CT < -9.06 ns,
2. CT > 13.18 ns and CT < 48.6 ns.

3.9 System Optimization

3.9.1 Overview

The main goal of the experiment was to study the mass spectroscopy of three-body YNN system by utilizing the $(e, e' K^+)$ reaction with the best achievable precision. The experimental system needs to be optimized carefully and systematically. Therefore, various calibration data were taken with different targets and different kinematics. In this section, the details about the optimization of various systems will be discussed.

3.9.2 BCM Calibration

To determine the total amount of charge that was delivered to the target, Hall A used the beam current monitor (BCM) system. The BCM was calibrated during the E12-10-103 (MARATHON) experiment and the detail of which can be found in Ref. [62].

3.9.3 BPM Calibration

To measure the position and direction of electron beam at the target, two BPM's were provided along the Hall A beam line. The BPM system was calibrated at the beginning of the MARATHON experiment. The more details of the BPM calibration can be found in Ref. [69].

3.9.4 Raster Calibration

The size of the electron beam was increased in both horizontal and vertical directions to reduce the density fluctuation of the target by local heating (see Fig. 3.13). In order to reconstruct the z -vertex correctly, the raster effect to the beam transverse

size needs to be corrected. The raster system contains two rasters, horizontal and vertical rasters. Since the vertical raster gives no effect to all the reconstructions as it was not used during the experiment, so that only the horizontal raster correction was needed. The matrix elements of the raster correction are:

$$p_{0x}, p_{0y}, p_{1x}, p_{1y}.$$

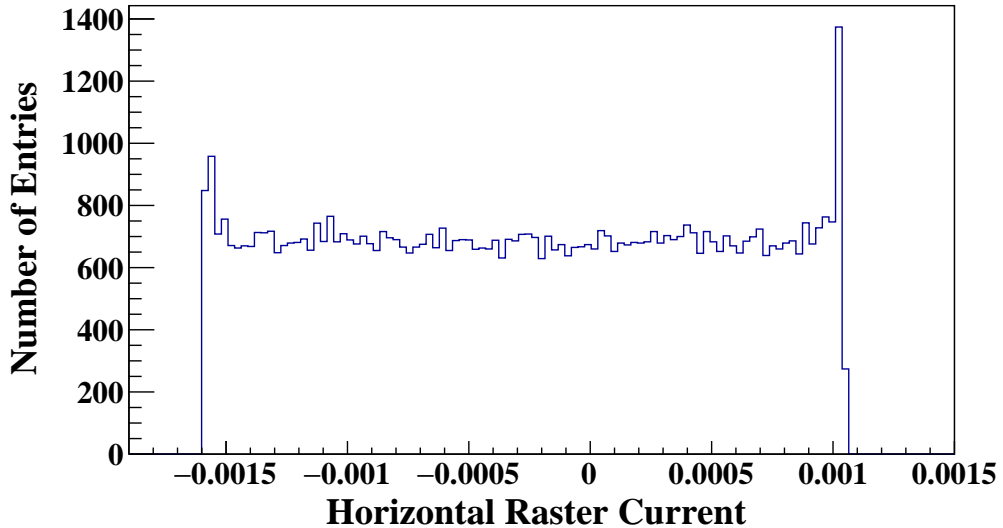


Figure 3.13. The schematic of the raster current along the horizontal direction.

Only the p_{0x} and p_{1x} for the horizontal raster correction were optimized. Since their nominal values were not known, so that their optimization was done with the help of the reconstructed z -vertex.

The z -vertex reconstruction was optimized first (will be discussed in following section) by using the non-rastered beam. Then the optimized z -vertex was plotted with the rastered beam. With the rastered beam the peaks of the carbon multi-foil target were broadened the beam uncertainty. The raster parameters were then optimized with the known nominal values of 11 carbon multi-foil peaks such that the peak locations and width became the same as that obtained from the non-rastered beam. The raster calibration was also done in the E12-10-103 experiment (see Ref. [50]) and both of the calibrations were found consistent.

3.9.5 Z-Vertex Optimization

Backward Transfer Matrix

Since the reaction took place at the target and the events were detected at the focal plane. The measured focal plane parameters (positions and angles) form the focal plane coordinate matrix. The target- z can be calculated by the focal plane coordinate matrix using a backward transfer matrix, M^{R2T} , as expressed by the equation:

$$Z_{tgt} = M^{R2T} \begin{bmatrix} x \\ x' \\ y \\ y' \end{bmatrix}_{fp}, \quad (3.9.1)$$

a third order matrix with 35 parameters was used to optimize the Z_{tgt} reconstruction matrix. More explicitly:

$$Z_{tgt} = \sum_{i+j+k+l=0}^n T_z(i, j, k, l) (x_{fp})^i (x'_{fp})^j (y_{fp})^k (y'_{fp})^l. \quad (3.9.2)$$

In the above equations, the subscript fp labels the parameters measured in FCS, tgt represents the reconstructed parameters at target. x and y are the positions and x' and y' are the tangents along the dispersive and non-dispersive planes, respectively. M^{R2T} is the backward transfer matrix and $T_z(i, j, k, l)$ are the matrix elements to be optimized.

Backward Transfer Matrix Optimization

To optimize the backward transformation matrix for the z -vertex, data were taken with the carbon multi-foil target under the single arm trigger condition. For the first loop, the z -vertex was produced by the initial backward transfer matrix and the events for tuning process were selected by placing a cut condition (eg. $|target z| < 1.5\sigma$),

where *target z* is the reconstructed *z*-vertex with the initial matrix and σ is the peak width with the same matrix. Then by using the least χ^2 method, the initial matrix elements were tuned by minimizing the χ^2 and a new matrix was generated. The new matrix would be closer to the real matrix. The χ^2 is defined as:

$$\chi^2 = \sum_{i=0}^N \frac{(X_{recons}^i - X_{ref}^i)^2}{\sigma \cdot N}, \quad (3.9.3)$$

where, N is the total number of events that take part in the tuning process, X_{recons}^i represents the reconstructed value, X_{ref}^i is the nominal value, and σ is the standard deviation. The tuning was iterated by multiple cycles and each cycle generated new matrix for the next cycle. As the peak width decreases continuously after each cycle of tunes, the events selection gate width was increased slightly to include more real events than background events. The iteration continued until the χ^2 was saturated or minimized. More detailed information about the optimization procedure can be found in Ref. [2]. A flow chart of optimization of the backward transformation matrix is presented in Fig. 3.14.

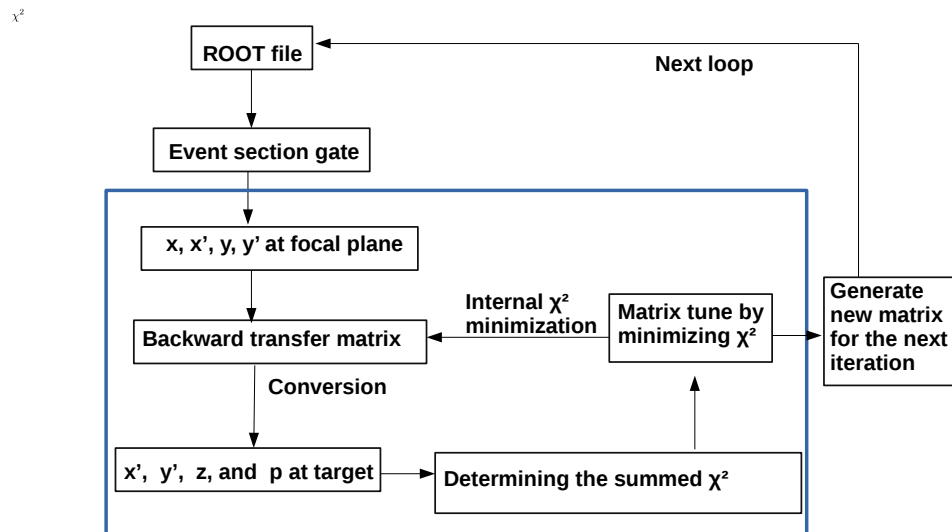


Figure 3.14. Schematic of flow chart of the backward matrix optimization process.

Z-Vertex with the Optimized Matrix

Since the z -vertex optimization was the single arm data analysis, therefore, each z -vertex was optimized separately. The optimized z -vertex reconstruction by LHR_S is shown in Fig. 3.15.

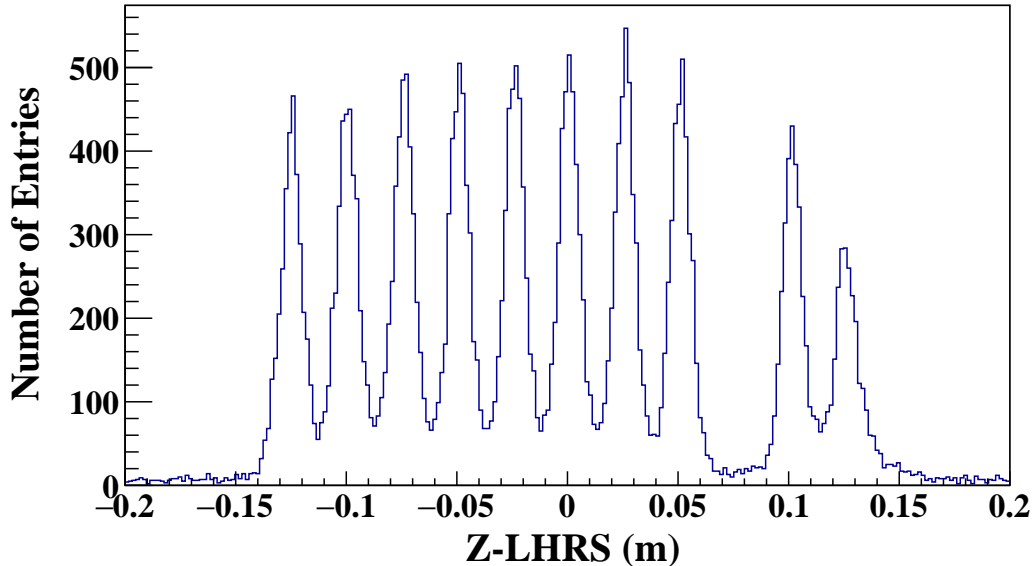


Figure 3.15. The LHR_S optimized z -vertex with the carbon multi-foil target.

Each peak in the spectrum represents a corresponding carbon foil. One foil was physically missing during the experiment and the gap represents the missing foil. Same quality was achieved for the RHRS z -vertex reconstruction. For the coincidence data analysis, the average of the two separately reconstructed z 's from LHR_S and RHRS was used as target z . The averaged z -vertex with the H target is shown in Fig. 3.16.

The two sharp peaks approximately at ± 12.5 cm were formed by the interaction of the beam electrons with the beam entrance and exit aluminum end caps. A z -vertex resolution of about $\sigma_z = 4.5$ mm was achieved.

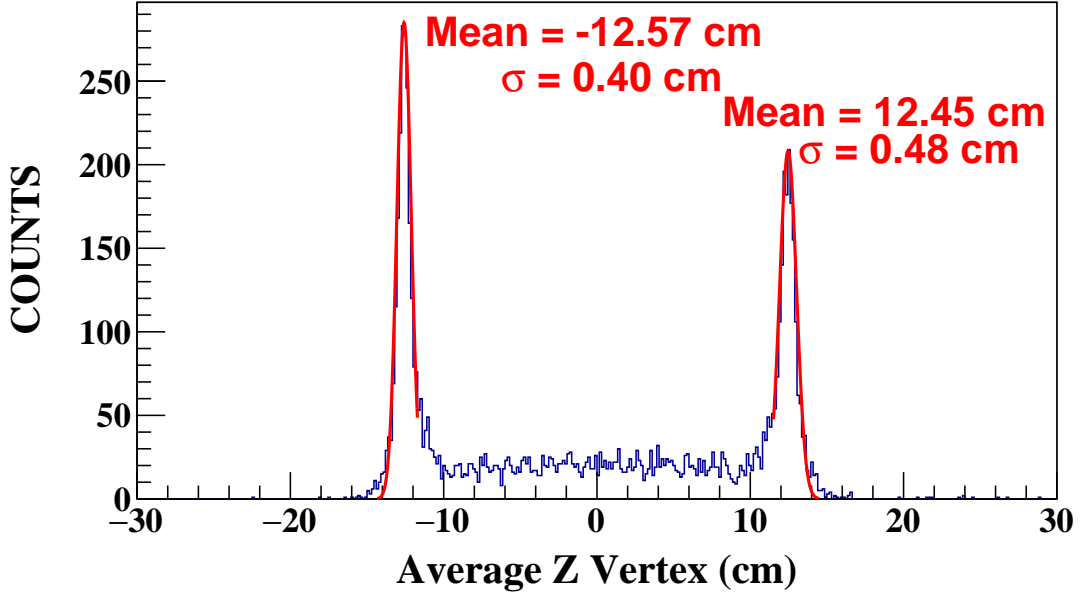


Figure 3.16. Average z -vertex with the H target which was obtained by taking the average of two separately reconstructed z 's from LHRs and RHRs.

3.9.6 Transformation Matrices for HRS Angle and Momentum

Since the angles and momentum at target are affected by the target z due to the extended length of the target, a z dependence was built in the HRS angle and momentum reconstruction matrices. Thus extra terms, the z dependence elements, were added into the angle and momentum reconstruction matrices. The general matrix equation then took the following form:

$$\begin{bmatrix} x' \\ y' \\ p \end{bmatrix}_{tgt} = M^{R2T} \begin{bmatrix} x \\ x' \\ y \\ y' \\ Z_T \end{bmatrix}_{fp}, \quad (3.9.4)$$

where, Z_T is the reconstructed z -vertex with the optimized z matrix described previously. The reconstructions can be expressed explicitly:

$$x' = \sum_{i+j+k+l+m=0}^n T_x(i, j, k, l, m) (x_{fp})^i (x'_{fp})^j (y_{fp})^k (y'_{fp})^l (Z_{tgt})^m, \quad (3.9.5)$$

$$y' = \sum_{i+j+k+l+m=0}^n T_y(i, j, k, l, m) (x_{fp})^i (x'_{fp})^j (y_{fp})^k (y'_{fp})^l (Z_{tgt})^m, \quad (3.9.6)$$

$$p = \sum_{i+j+k+l+m=0}^n T_p(i, j, k, l, m) (x_{fp})^i (x'_{fp})^j (y_{fp})^k (y'_{fp})^l (Z_{tgt})^m. \quad (3.9.7)$$

The matrix elements T 's in the above equations need to be optimized using the corresponding calibration data.

3.9.7 HRS Angle Optimization

The HRS angle matrix optimization was also a single arm data analysis. The calibration data were taken from the carbon multi-foil target with the sieve slit (SS) in place. The details about the SS plate was discussed in Section 2.7.

The angle matrices were optimized separately with known focal plane angle and position coordinates. A 4th order matrix with 126 parameters was used for the reconstruction of the HRS angles. The optimization procedure is the same as that of the z -vertex optimization (see Section 3.9.5). The χ^2 is defined by the equation 3.9.3. With the known target z separated from each of the carbon foil, each SS hole provided a unique set of nominal values for θ and ϕ angles. These nominal values were used as X_{ref}^i defined in Eq. 3.9.3 for the events passed through the corresponding holes. Events were separated for each SS hole and their reconstructed angle values were the X_{recons}^i in the χ^2 definition. The angle matrices for θ and ϕ were then optimized separately as described previously for the target z matrix optimization. The

reconstructed θ and ϕ correlation for the LHRs and RHRs optimized angle matrices in terms of SS hole location is plotted in Fig. 3.17 and Fig. 3.18, respectively.

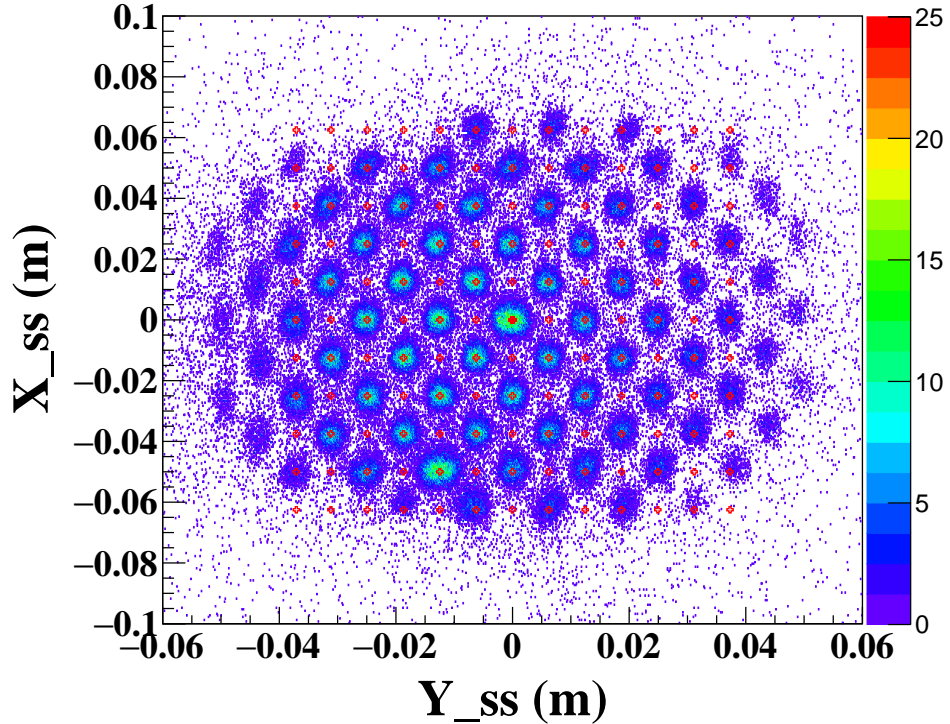


Figure 3.17. The LHRs θ and ϕ correlation in terms of the sieve slit hole locations.

For the LHRs which was in negative polarity, scattered electrons were the dominant particles. Since the energy loss and multiple scattering effects are much stronger for the scattered electrons with light mass, so that the thickness of the SS plate was sufficient to prevent the electrons that did not pass through SS holes to reach the focal plane. Therefore, in the LHRs θ and ϕ correlation, the SS hole pattern is clear. However, for the RHRs, the positively charged hadrons (predominately the pions) with masses much heavier than positrons were dominant. The thickness of the existing SS plate did not give sufficient energy loss and multiple scatterings. Thus, a large amount of particles that punched through the plate could reach the focal plane and they caused a severe background seen between the SS holes in the RHRs and correlation. In other words, a significant amount of background mixed in the selected

events for the particles that passed through SS holes. Thus, the event cleaning took extra effort in the matrix optimization operation.

With the optimized HRS matrices, the angular resolution of about 3.2 mrad for θ and 1.1 mrad for ϕ was achieved.

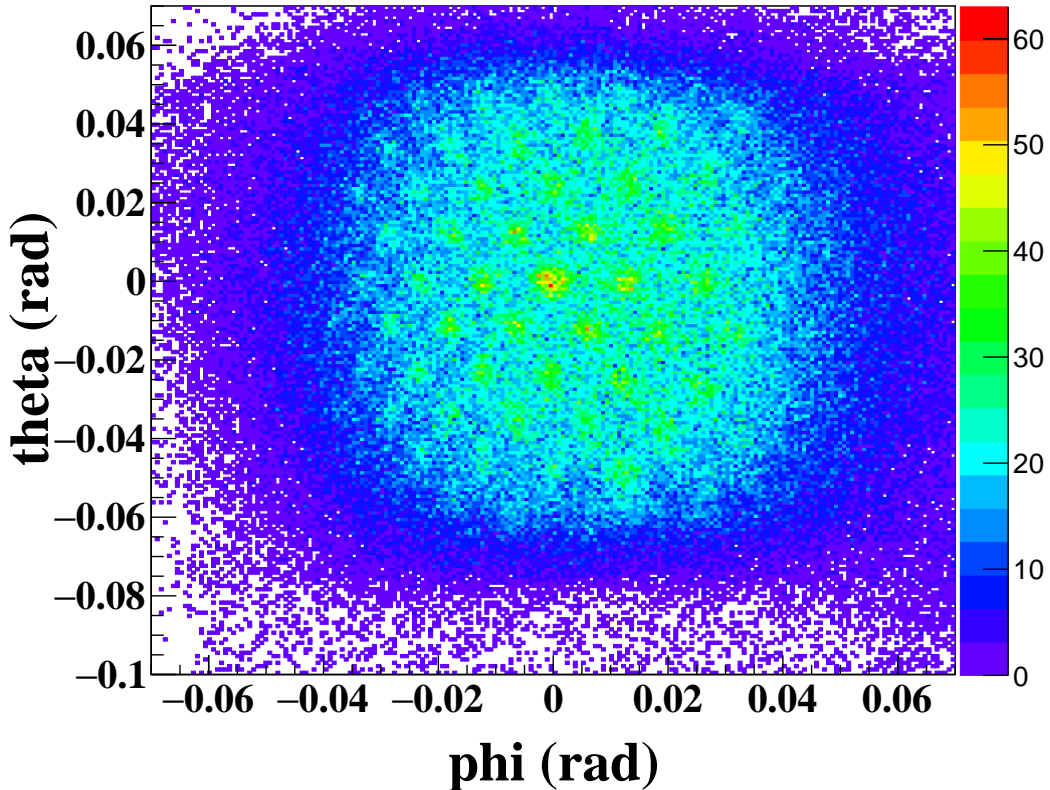


Figure 3.18. The RHRS θ and ϕ correlation. Each spot represents a SS hole.

3.9.8 Missing Mass

The electroproduction of Λ (Σ^0) from a proton target (discussed in Sec. 1.5) is expressed as:

$$e + p = e' + \Lambda + K^+. \quad (3.9.8)$$

The scattered electron (e') and the K^+ produced associatively with Λ can be detected by the two different spectrometers. However, the Λ cannot be measured directly

because it is a neutral particle with very short lifetime. Therefore, to measure the Λ particle an indirect method called the missing mass method is used. For e' and K^+ , their focal plane measured information (positions and angles) are converted into the momentum vectors at the target by using the backward transfer matrices [70] representing the optical system for LHRs and RHRs. Then the missing mass can be calculated by the following equations [25],

$$e + t = e' + K^+ + Hyp, \quad (3.9.9)$$

where, t is the target proton or nucleus at rest and Hyp is the hyperon or hypernuclei. From the energy conservation principle,

$$E_e + M_t = E_{e'} + E_{K^+} + E_{Hyp}. \quad (3.9.10)$$

Here, E is the energy of particle and M is the rest mass of the particle. Then:

$$E_{Hyp} = E_e + M_t - E_{e'} - E_{K^+}. \quad (3.9.11)$$

The momentum conservation principle requires that,

$$\vec{p}_{Hyp} = \vec{p}_e - \vec{p}_{e'} - \vec{p}_{K^+}. \quad (3.9.12)$$

From the energy momentum relation, the invariant mass square is:

$$(M_{Hyp})^2 = (E_{Hyp})^2 - (\vec{p}_{Hyp})^2. \quad (3.9.13)$$

After solving the energy and momentum conservation equations, the missing mass (mass of hyperon or hypernucleus) will be:

$$\begin{aligned}
M_{Hyp} = & [(E_e + M_t - E_{e'} - E_{K^+})^2 \\
& - (p_e^2 + p_{e'}^2 + p_{K^+}^2 - 2p_e p_{e'} \cos \theta_{ee'} - 2p_e p_{K^+} \cos \theta_{eK^+} + 2p_{e'} p_{K^+} \cos \theta_{e'K^+})]^{1/2}, \\
\end{aligned} \tag{3.9.14}$$

where,

$$\cos \theta_{e'K^+} = \cos \theta_{ee'} \cos \theta_{eK^+} + \sin \theta_{ee'} \sin \theta_{eK^+} \cos(\phi_e - \phi_{K^+}), \tag{3.9.15}$$

where, θ_{eK^+} , $\theta_{ee'}$, and $\theta_{e'K^+}$ are the angles of the particles in the spherical coordinate system or in the beam geometry. These angles are obtained by the coordinate transformation from the angle reconstructions of x' and y' at target and become known. The beam electron energy is given by:

$$E_e = \sqrt{(M_e)^2 + (\vec{p}_e)^2}. \tag{3.9.16}$$

Here both the electron mass M_e and the beam energy E_e are known quantities. Therefore, to calculate the missing mass, the momentum of scattered electron ($\vec{p}_{e'}$) and K^+ momentum (\vec{p}_{K^+}) need to be determined. These momenta were reconstructed at the target by using the focal plane information with the help of the backward transfer matrices and the data with known rest masses (which will be discussed in a later section). Once the M_{Hyp} is obtained, the Λ binding energy B_Λ can be calculated by [25]:

$$B_\Lambda(^A_\Lambda Z) = M(^{A-1}Z) + M_\Lambda - M_{Hyp}(^A_\Lambda Z). \tag{3.9.17}$$

where, Z represents the proton number, and $M(^{A-1}Z)$ and M_Λ are the rest masses of a core nucleus at the ground state and a Λ .

3.9.9 Energy Loss Correction

The incident and scattered particles lose their energies when they pass through the materials of the target cell walls and the target gas. Therefore, the energies of the incoming and outgoing particles deviate from the given or reconstructed energies. The energy loss depends on the reaction point at the target, the charge particle type, and the thickness of the material through which it passes. The inaccurate energy and momentum information of beam electron (e), scattered electron (e'), and K^+ at the reaction vertex will affect the precision of the absolute missing mass scale and resolution. Therefore, the main goal of the energy loss study is to investigate the energy loss as a function of the target z where the reaction took place and the angular x' which affects the path length in the materials, so that corrections can be made to minimize the contribution from the target energy straggling to the missing mass resolution.

Due to technical challenge in machining the target cell, the wall thickness could not be made perfectly uniform. It varies from 300 to 500 μm (see Ref. [55]).

The target energy straggling was studied by using a GEANT4 simulation with inputs including the full kinematics, reaction coordinate, target geometry, target materials, windows of target chamber and HRS's, and the HRS optics and acceptance. The studies were made for three different cell wall thicknesses, 300 μm , 400 μm , and 500 μm . The final corrections were extracted from the simulation result with the average thickness of 400 μm .

For the beam electron, the contribution to the energy loss from the target gas was found to be negligibly small compared to that from the entrance aluminum window. It can be considered having no z -dependence. Therefore, the correction for the beam energy is simply the most probable value (MPV) obtained by fitting a Landau function over the momentum loss distribution. That is, $\Delta p = \text{MPV}$. To take the energy

straggling into account, the following correction is applied:

$$p_{beam}^{real} = p_e^{measured} - \Delta p, \quad (3.9.18)$$

where, $p_e^{measured}$ was provided by CEBAF. The MPV values found for the three different thicknesses are listed in Table 3.1. The difference was found to be very small, only about 40 keV. The uncertainty from the wall thickness variation for the beam energy is thus about 5 times smaller than the beam energy resolution ($\sim \pm 0.220$ MeV). Thus a constant correction was made by assuming a thickness of 400 μm .

Table 3.1

The MPV values for the different window thicknesses for the beam electron.

| Thickness (μm) | MPV (MeV) |
|-----------------------------|-----------|
| 300 | 0.148 |
| 400 | 0.1843 |
| 500 | 0.2234 |

Since the two HRS's were set at 13.2° with respect to the beam direction, so that most of the scattered particles that were accepted by the spectrometers passed through the side walls and their energy losses have strong angle dependence. Figure 3.19(a) shows two clusters of correlated distributions from the e' momentum loss vs the target angle x' , and the spectrum (b) is the one-dimensional plot of the momentum loss. When the reaction takes place in the shallow region of the target with z -average < 8.0 cm, the scattered charged particles have to travel much longer path in the side aluminum wall before they completely exit the target cell. In such case, the particles lose more energy since aluminum is much denser than the gas and have strong x' dependence. These events form the larger peak in Fig. 3.19(b). On the other hand, when the reaction takes place near the beam exit end that is when z -average

> 8.0 cm, the particles pass through the exit cell wall with much smaller x' dependence to their path lengths in the aluminum wall (see the lower correlation cluster in Fig. 3.19(a)). In this case, these events form the smaller peak in Fig. 3.19(b).

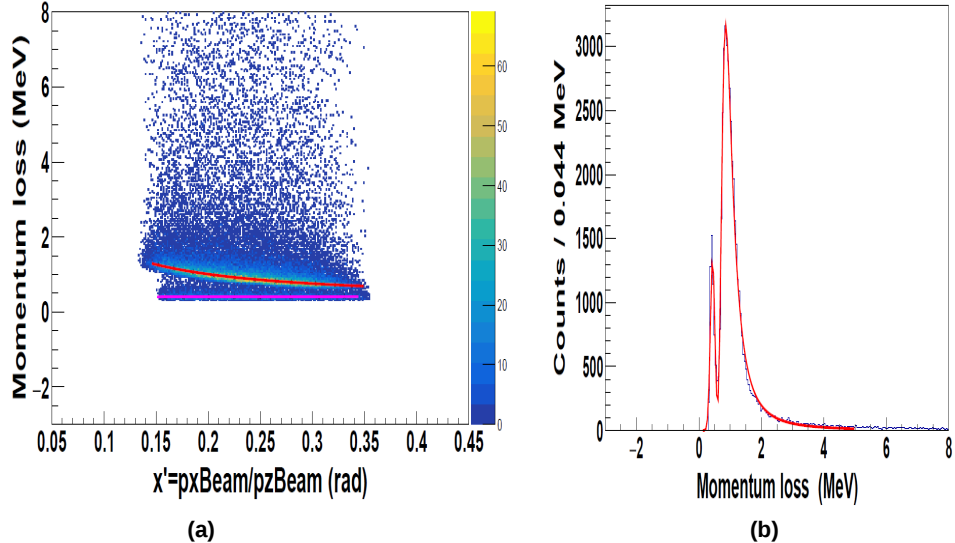


Figure 3.19. (a) The e' momentum loss vs x' ($= dx/dz$) correlation for the cell thickness of $400 \mu\text{m}$. Here, (b) is the projection of the momentum loss. The upper cluster (or the large peak) corresponds to the region of z -average < 8.0 cm and the lower cluster (or the small peak) corresponds to the region of z -average > 8.0 cm.

To make correction for the target energy loss, the two correlations were fitted separately by polynomial functions for the x' dependence. Then the momentum loss corrections were made as:

$$p_K^{\text{real}} = p_K^{\text{measured}} + \Delta p, \quad (3.9.19)$$

$$p_{e'}^{\text{real}} = p_{e'}^{\text{measured}} + \Delta p, \quad (3.9.20)$$

where, $p_{e'}^{\text{measured}}$ and p_K^{measured} were reconstructed momentum at the target.

The correction function for the particles having the z -average < 8.0 cm was fitted by,

$$\Delta p = [p0'] \times \sin([p1'] \times x') + [p2'], \quad (3.9.21)$$

while those with the z -average > 8.0 cm was simply:

$$\Delta p = [p0] \times x' + [p1]. \quad (3.9.22)$$

The momentum loss for the K^+ s have the similar characters. Therefore, the same polynomial function fits to the two correlations were applied. The parameters $p0$, $p1$, $p0'$, $p1'$, and $p2'$ for the K^+ s momentum correction for the different thicknesses are summarized in Table 3.2.

Table 3.2

The Δp parameters for different cell thicknesses for the K^+ s momentum loss correction.

| Thickness (μm) | z -average (cm) | $p0$ ($p0'$) | $p1$ ($p1'$) | $p2'$ |
|-----------------------------|----------------------|-------------------|------------------|---------|
| 300 | z -average > 8.0 | $2.55664e^{-02}$ | $3.62363e^{-01}$ | - |
| | z -average < 8.0 | $-9.95197e^{-01}$ | -4.66838 | 1.59176 |
| 400 | z -average > 8.0 | $3.15800e^{-02}$ | $4.05819e^{-01}$ | - |
| | z -average < 8.0 | -1.31749 | -4.61513 | 2.03687 |
| 500 | z -average > 8.0 | $3.12968e^{-02}$ | $4.45588e^{-01}$ | - |
| | z -average < 8.0 | -1.66166 | -4.60416 | 2.50814 |

Similarly, the parameters $p0$, $p1$, $p0'$, $p1'$, and $p2'$ for the e' momentum correction for the different thickness are summarized in table 3.3.

Table 3.3

The Δp parameters for different cell thicknesses for the e 's momentum loss correction.

| Thickness (μm) | z -average (cm) | $p0$ ($p0'$) | $p1$ ($p1'$) | $p2'$ |
|-----------------------------|----------------------|------------------|-------------------|---------|
| 300 | z -average > 8.0 | $2.48517e^{-02}$ | $3.66697e^{-01}$ | - |
| | z -average < 8.0 | -1.00683 | -4.58662 | 1.60889 |
| 400 | z -average > 8.0 | $6.23409e^{-03}$ | $4.03363e^{-01}$ | - |
| | z -average < 8.0 | -1.35758 | -4.59571 | 2.09093 |
| 500 | z -average > 8.0 | $3.83021e^{-02}$ | $4.455542e^{-01}$ | - |
| | z -average < 8.0 | -1.71785 | -4.59446 | 2.58234 |

Figure 3.20 illustrates the energy loss by the scattered e' 's after the angular dependence part was corrected. The σ width of the peak in Fig. 3.20 (b) shows that there is a contribution of about $\pm 40 - 50$ keV to the overall missing mass resolution, much smaller than those from the uncertainties of the beam energy and HRS momentum reconstructions.

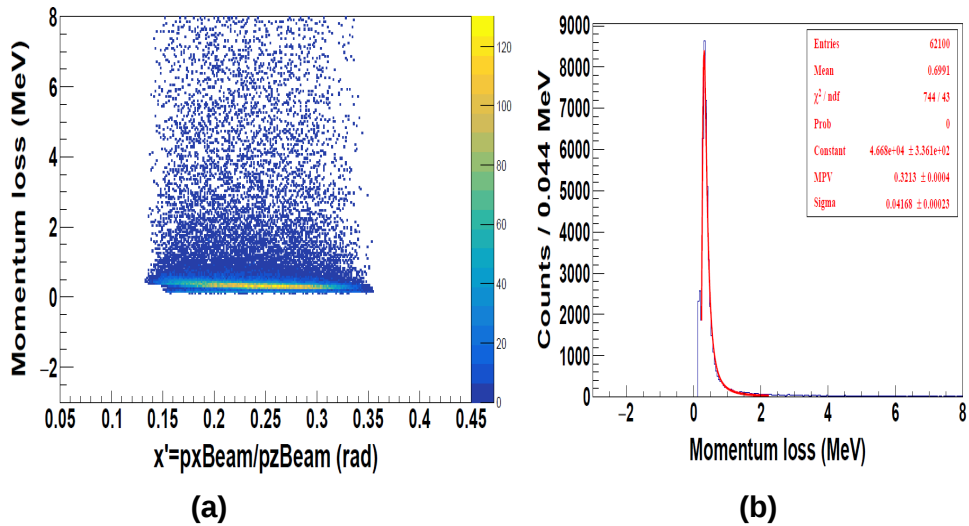


Figure 3.20. (a) The e' momentum loss vs x' ($= dx/dz$) correlation with the angular dependence corrected. Here, (b) is the projection of the momentum loss.

3.9.10 Kinematic Space for the $(e, e'K^+)$ Experiment

With known beam energy and scattering angles, the missing mass of a recoil system from the $(e, e'K^+)$ reaction is uniquely correlated in the kinematics space defined by the two dimensional correlation of the e' momentum vs the K^+ momentum. For this experiment, to maximize the acceptance in search for the Ann resonance around the threshold region, the tritium kinematics was defined by maximizing the correlation for the Ann threshold mass, see the line illustrated in Fig. 3.21. Here the

label (T/T) stands for the tritium data taken under the tritium kinematics, while (H/T) and (H/H) are for the H data taken under T and H kinematics, respectively.

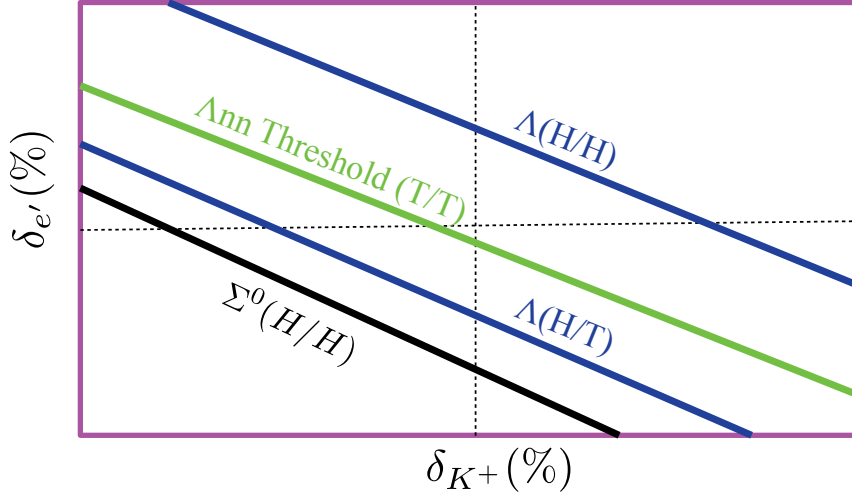


Figure 3.21. Illustration of the kinematic space for the $(e, e' K^+)$ experiment.

In the T kinematics, the free Λ 's produced from the H target [Λ (H/T)] is less favored, due to the limited kinematics acceptance defined by the two HRSSs. Then the free Σ^0 's from the H target is out of the acceptance under the T kinematics. In order to simultaneously accept both the free Λ 's and Σ^0 's for the purpose of calibrating the absolute missing mass scale as well as optimizing the momentum matrices using these mass correlations, the H data was specifically taken with the H kinematics, labeled as H/H, which had the central momentum of LHRSS lowered from 2.218 GeV/c to 2.10 GeV/c. When the kinematics space is plotted using the relative momenta, δ (%), the location of the mass correlations can be shown in the same plot. The correlation of the free Λ 's for H/H is moved up in the space with reduced yield but allowed the free Σ^0 's (H/H) been accepted with a sufficient yield rate. This was optimized by taking into account the cross section ratio of Λ/Σ^0 .

Utilizing the correlation in the kinematics space to optimize the momentum matrices with both the Λ and Σ^0 not only provide a precision determination of the absolute missing mass scale, but also optimize the quality uniformity in the kinematics space.

Data for the free Λ s were also taken from the H target under the T kinematics (H/T). This was to verify its location in the kinematics space and also to provide the confirmation of the central momentum scaling of the LHRS between the two kinematics. These free Λ 's were also used for the matrix optimization to further improve the uniformation.

3.9.11 Momentum Optimizations

The events from the free Λ and Σ^0 produced by the $(e, e' K^+)$ reaction from the H target were used to optimize the momentum matrices, utilizing their known masses and the correlations in the kinematics space (discussed previously). This has been a standard technique applied successfully for all the previous Hall C hypernuclear spectroscopy experiments [24]. Data from the H target with two different kinematics were both used.

A fifth order matrix with 252 elements was used for the HRS momentum reconstruction in which the z -dependence elements were included, similar to the matrices for the angle reconstructions. The momentum vector was obtained by the focal plane parameters (x, x', y, y') and the reconstructed target z using the backward transfer matrix discussed in Section 3.9.6, Eq. 3.9.7. With the reconstructed angles which were transferred into the spherical beam coordinates and the momenta of the scattered e' and K^+ , the missing mass of the selected event from either the Λ or Σ^0 peak was kinematically calculated according to Eq. 3.9.14 in Section 3.9.8. This reconstructed missing mass was used as the X_{recons}^i defined in Eq. 3.9.3 in Section 3.9.5, while the corresponding known mass of the Λ or Σ^0 served as X_{ref}^i in obtaining the summed χ^2 . Then the HRS momentum matrices were optimized by using the least χ^2 minimization method as discussed in Section 3.9.5. At the beginning with the initial matrices, the peak width of Λ and Σ^0 was found to be about 6 MeV (σ). Thus, the events for the matrix tune were selected from the Λ and Σ^0 peaks within the peak

width of about $\pm 1.5\sigma$. As the peak width of reconstructed missing mass getting narrower after multiple cycles, the events selecting gate width was increased gradually to $\pm 1.85\sigma$. Due to the correlation between the two momenta, the LHRS and RHRs matrices were tuned alternatively one by one with few iterations (up to 3 tune maximum) at a time. After each cycle of tune, the corresponding peak width of Λ and Σ^0 was studied. The tuning process was continued until the χ^2 got saturated. After the peak width of Λ and Σ^0 reached to about 2 MeV in σ which did not yet meet the experimental requirement, further tune appeared not improving the missing mass resolution. Two problems were recognized and they were associated with the time jitter for the RHRs VDC and the dependence on the residual angular uncertainties. These will be discussed in the following sections.

3.9.12 Time Jitter Correction

The coincidence trigger for the E12-17-003 experiment was generated by considering the LHRS time (LHRS S2 scintillator time) as reference. This trigger was used as the TDC common start for the VDCs in both LHRS and RHRs, instead of using the single arm trigger for the local TDC common start. In case for LHRS, the common start was localized equivalently. Therefore, the VDC gave normal tracking precision after the drift velocity calibration. However, since the hadrons in the RHRs had velocity and path length variations relative to the LHRS single arm timing, so that the TDC common start used by the coincidence trigger for the VDC's drift time had a time jitter. This resulted the quality of the RHRs focal plane parameters (x, x', y, y') was worsen by about 3 to 4 times than that of LHRS and affected the quality of the RHRs momentum reconstruction as well as the missing mass resolution.

Figure 3.22 shows a comparison of the RHRs raw TDC spectra with single arm trigger mode used to take calibration data and coincidence trigger mode before such

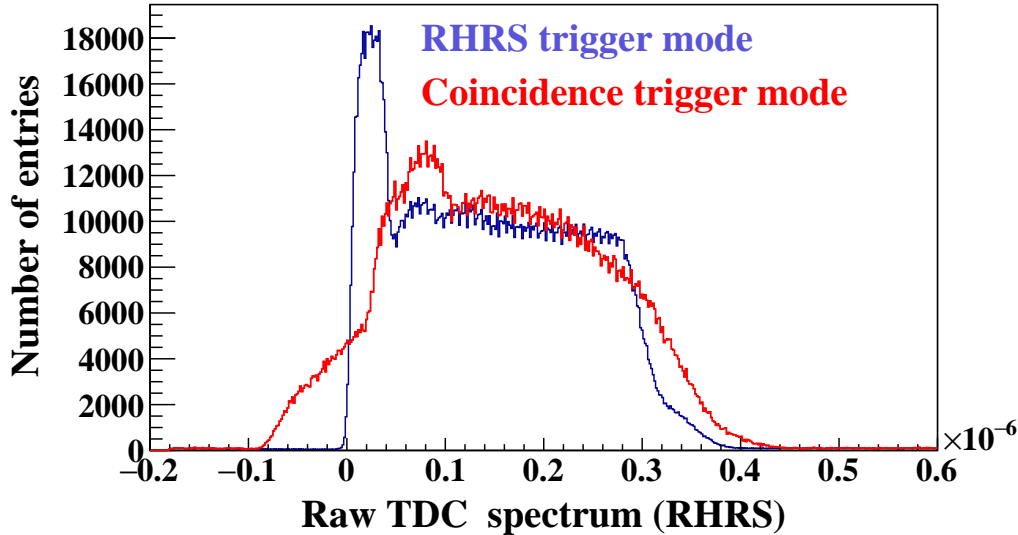


Figure 3.22. RHRHS raw TDC spectrum before the time jitter correction. The blue spectrum represents the RHRHS single arm trigger mode and red spectrum represents the coincidence trigger mode.

time jitter was corrected. A significant smearing and broadening could be clearly seen.

This problem was eventually minimized by applying a software correction on an event-by-event base to the raw TDC data. After the time jitter correction, both of the spectra were in agreement with one another (see Fig. 3.23). The time jitter corrected RHRHS focal plane parameters (x, x', y, y') had then the similar quality as that of the LHRHS and the overall missing mass resolution was improved by about 20%.

3.9.13 Dependence on the Residual Angular Uncertainties

During the momentum optimization, when the Λ and Σ^0 resolution reached about 1.7 MeV (σ), improvement could not be made from further tunes. A Monte Carlo simulation (which will be presented in more detail in the following section) for the missing mass resolution was carried out to study the dependences on the residual energy/moment and angular uncertainties. The study showed that the light mass system (A

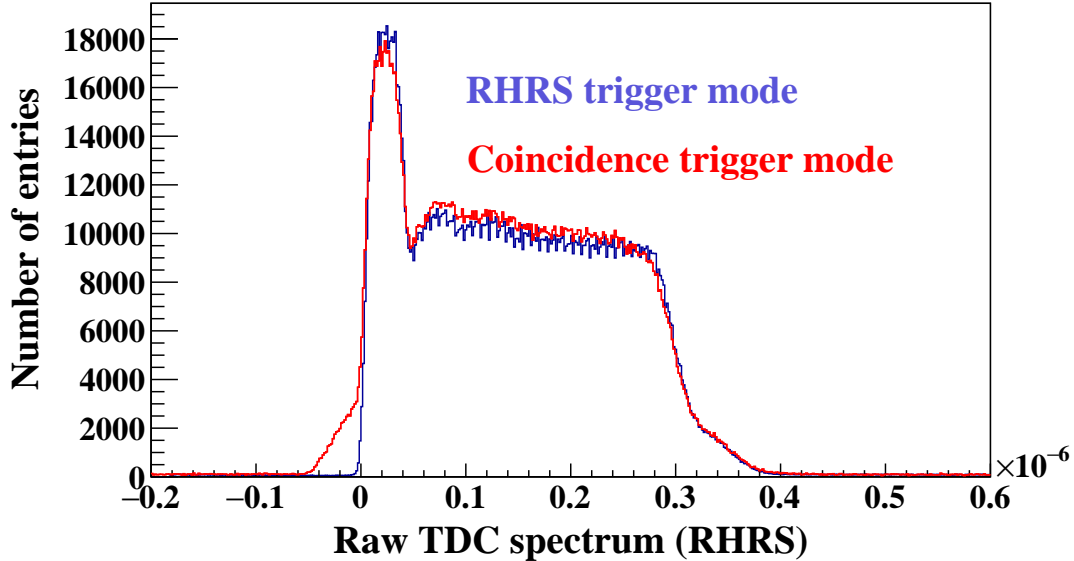


Figure 3.23. RHRs raw TDC spectrum after the time jitter correction. The blue spectrum represents the RHRs single arm trigger mode and red spectrum represents the coincidence trigger mode. The coincidence time spectrum was scaled up by 2.8 to make the comparison.

= 1) has dominant contributions to the mass resolution from the residual angle uncertainties (see Fig. 3.27) while the heavy mass system ($A > 7$) is almost completely dominated by the residual uncertainty contributions from the energy and momentum (see Fig. 3.24). Further tuning the momentum matrices with the Λ and Σ^0 masses, as the contribution from the residual angular uncertainties overshadowed that from the momentum uncertainty, could result in imperfect and incorrect momentum matrices. This suggested that to improve the momentum resolution further, a heavy mass system with negligible angular dependence needs to be involved in the matrix tune along with the Λ and Σ^0 masses which play the role only in locking the correct absolute mass scale.

3.9.14 Monte Carlo Simulation for Missing Mass Resolution

A Monte Carlo (MC) simulation was performed to study the missing mass resolution achievable by this experiment for various nuclear mass A and its sensitivities to various dominant residual uncertainties. The initial goal was to make a prediction to the missing mass resolution for the A = 3 system. However, the result suggested also that a heavy system must be involved in the momentum matrix optimization in order to reach the best achievable resolution under this experimental condition. The simulation investigation had two parts.

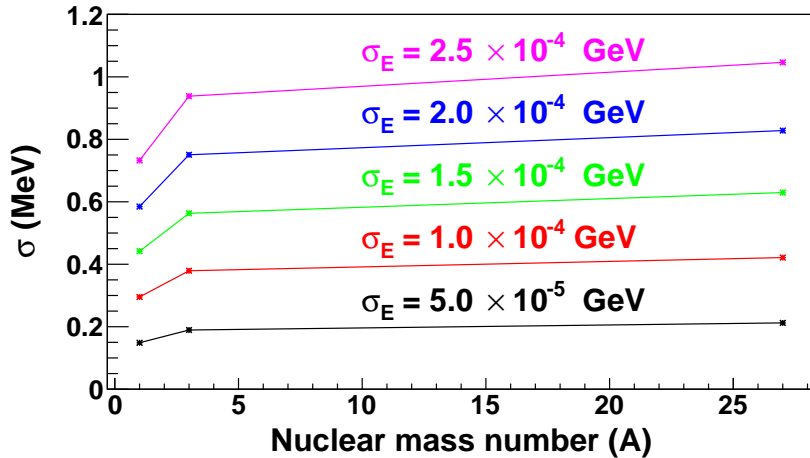


Figure 3.24. The correlation between the resolution and nuclear mass number (A) when the beam energy is smeared at different level of uncertainties.

In the first part, the events were generated randomly according to the experimental conditions by evaluating the real data. A fix beam energy was used. The simulation used the realistic momentum and angular acceptances which were obtained from the analysis of real data. Scattered electron e' was generated randomly for its momentum and angles within the known acceptances. Then the emission angles of K^+ were randomly generated according to the known angular acceptance. The K^+ momentum was then kinematically calculated. A momentum gate was used to remove any K^+ that had momentum outside the acceptance. Therefore, this part of simulation was to generate the events that had ideal kinematic parameters.

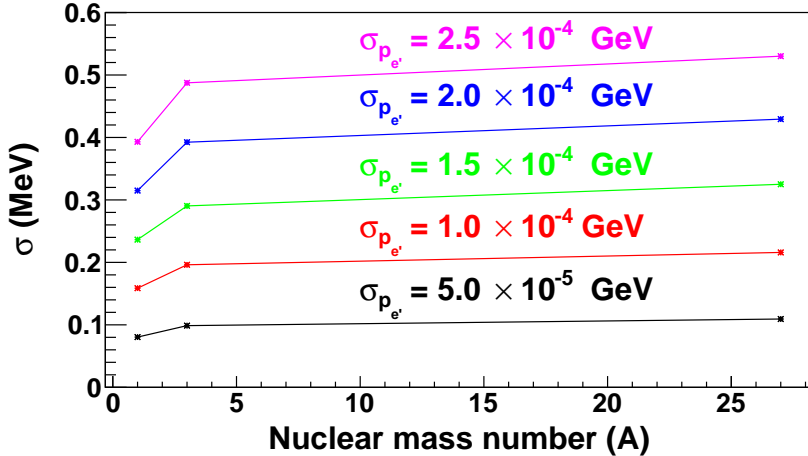


Figure 3.25. The correlation between the resolution and nuclear mass number (A) when the LHRM momentum is smeared at different level of uncertainties.

The second part studied the missing mass resolution by introducing uncertainties from the beam energy, the momentum from LHRM (e') and RHRM (K^+), and the scattering angle (θ) in spherical coordinates for e' and K^+ , and the angle ($\phi - \phi'$) between the scattering and reaction planes. The missing mass resolution as a function of the target mass A, with the recoil mass defined by the threshold mass of the correspondent hyperon or hypernucleus, was studied by introducing one type of uncertainty at time, in order to gain the knowledge on the level of contribution and its sensitivity to the nuclear mass A. The uncertainty for a kinematic parameter was introduced by randomly smearing the given value from the part 1 simulation within $\pm 4\sigma$ according to a Gaussian probability distribution.

Figure 3.24, 3.25, and 3.26 show the missing mass resolution as a function of A due to each of the uncertainties from the beam energy, LHRM momentum, and RHRM momentum, respectively. A common characteristics can be seen in term of the A dependence due to these energy and momentum uncertainties. The uncertainty contributes ($\sim 33\%$) less to the missing mass resolution for the $A = 1$ system (i.e. p to Λ or Σ^0) than to the system with $A = 3$ and above. This means that the resolution for the lightest system is less sensitive than that for the heavier systems. Although

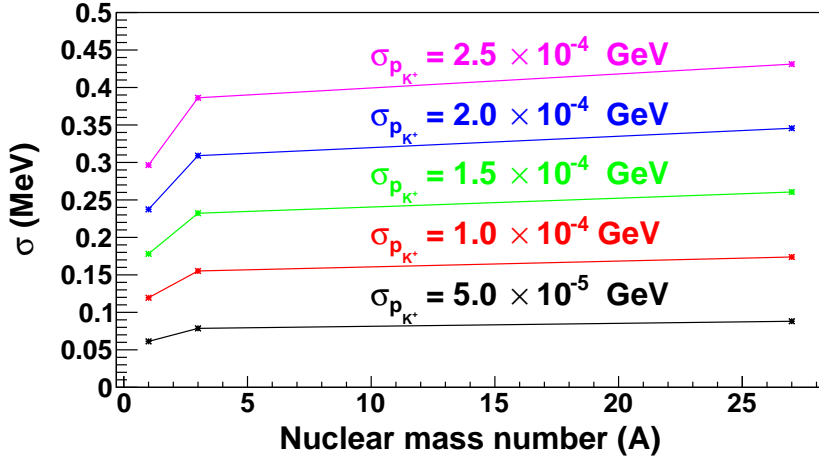


Figure 3.26. The correlation between the resolution and nuclear mass number (A) when the RHRs momentum is smeared at different level of uncertainties.

the contributions are more for the heavier systems ($A \geq 3$) but the sensitivity is rather small, almost a constant. With the same uncertainty level, the beam energy uncertainty appears to contribute the most while that from RHRs (K^+) is the least. This is merely because that the beam energy is 4.326 GeV, while the central momenta of LHRs and RHRs are 2.218 GeV/c and 1.823 GeV/c, respectively. If they are at the same energy/momenta level, the contributions are almost the same. Thus, the beam precision is crucial for high resolution mass spectroscopy.

Figure 3.27, 3.28, and 3.29 show the missing mass resolution as a function of A due to each of the uncertainties from the e' scattering angle, the K^+ reaction angle, and the reaction plane angle, respectively. All of them are in spherical coordinates with the beam direction points along the z-axis. The A dependence for all these three contributions shows a common feature that the light systems are much more sensitive to the angular uncertainty. The sensitivity decreases rapidly after $A = 3$. On the other hand, at the same angular uncertainty level the e' scattering angle uncertainty is obviously dominant, giving more than 4 times larger contributions. This is because that the mass of the scattered electron is much less than that of K^+ .

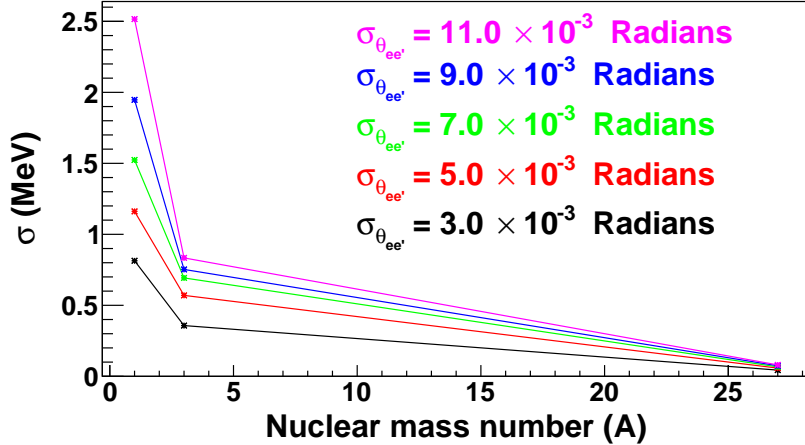


Figure 3.27. The correlation between the resolution and nuclear mass number (A) when the e' scattering angle ($\theta_{ee'}$) is smeared at different level of uncertainties.

To make evaluation and prediction on the achievable missing mass resolution for various of mass A with the experimental conditions from this experiment, the realistic uncertainties for the basic kinematic parameters were estimated. For the beam energy, the relative uncertainty was evaluated by checking the stability of the beam central value which was recorded on a trigger-by-trigger level although the readout was done in 0.5 Hz and the controlled limit of the beam energy spread by the SLI monitor for the acceptable beam. The relative beam energy uncertainty was estimated to be 6.7×10^{-5} , dominated by the energy spread. The relative momentum uncertainty of the HRS spectrometer was assumed to be $\sigma = 1.0 \times 10^{-4}$, which is about 65% worse than the best achievable uncertainty due to taking into account the uncertainties from straggling losses from target and all the vacuum windows. The estimate of the angular uncertainties were obtained from the sieve slit data analyses. The uncertainty for $\theta_{e'}$ and θ_{K^+} is 3.4 mrad (σ) and the uncertainty for $\Delta\phi$ is 4.8 mrad (σ). These uncertainties are listed in Table 3.4.

Figure 3.30 shows the A dependence of the achievable missing mass resolution predicted by the simulation using the estimated uncertainties listed in Table 3.4. The

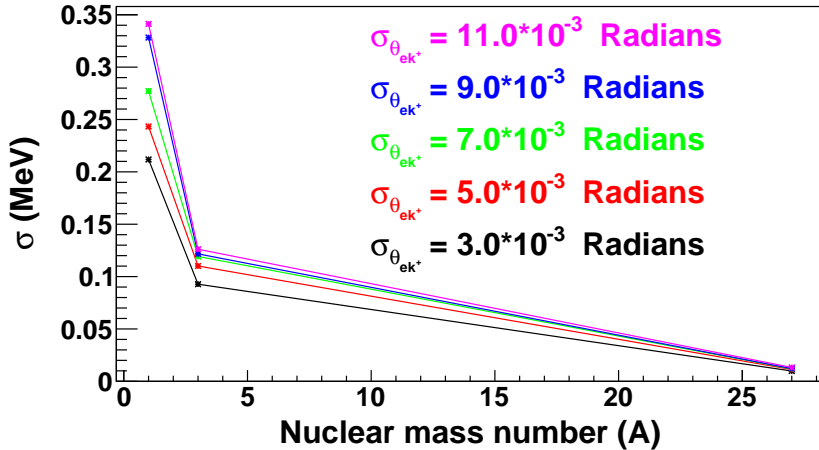


Figure 3.28. The correlation between the resolution and nuclear mass number (A) when the K^+ reaction angle (θ_{eK^+}) is smeared at different level of uncertainties.

Table 3.4

The details about the uncertainties used in the Monte Carlo simulation.

| Parameters | Numerical value |
|---|----------------------|
| Relative beam energy uncertainty (σ) | 6.7×10^{-5} |
| Relative HRS momentum uncertainty (σ) | 1.0×10^{-4} |
| HRS angle (θ) uncertainty (σ) | 3.4 mrad |
| $\Delta\phi$ uncertainty (σ) | 4.8 mrad |

achievable resolutions for the $A = 1$, 3 , and 27 systems are listed in Table 3.5. The $A = 1$ systems correspond to Λ and Σ^0 produced from the H target for the absolute missing mass scale calibration. The $A = 3$ is for the 3-body hypernuclear systems for which this experiment is investigating. Thus, this gave a prediction on the intrinsic mass resolution which should be excluded from the measured width to extract the natural width for a possible peak near the Λ separation threshold. The $A = 27$ system corresponds to aluminum which is the only other material which had the events mixed in the production data.

The resolution decreases dramatically as a function of about $1/A^{1.3} + 0.39$ and reaches almost a constant after $A > 7$. Based on the studies on the individual contri-

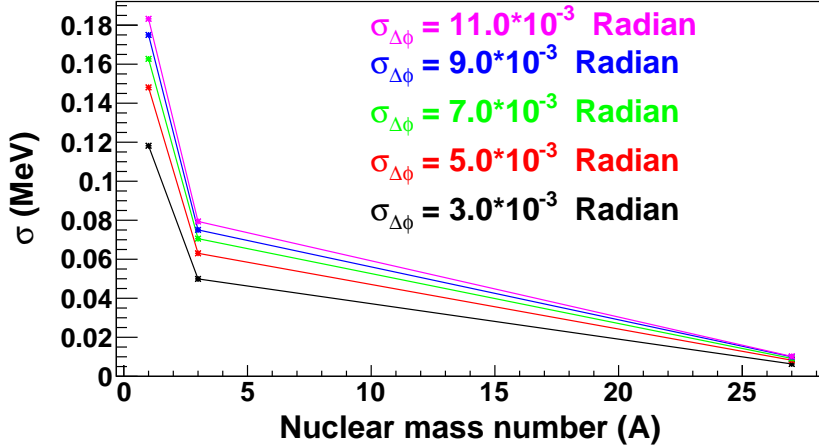


Figure 3.29. The correlation between the resolution and nuclear mass number (A) when the reaction plane angle ($\Delta\phi$) is smeared at different level of uncertainties.

butions it shows obviously that the resolution for the $A = 1$ system is dominated by the angular resolution which is limited by the optical properties of HRS. On the other hand, the resolution of heavier systems ($A > 7$) is rather insensitive to the angular uncertainties and completely dominated by the energy/momenta uncertainties.

This study gave a strong and important suggestion. Although using the known masses of Λ and Σ^0 in the optical optimization is an critical technique to ensure a high precision on the absolute missing mass scale, but they cannot be used alone to make an ultimate optimization of the HRS momentum matrices. A hard forced tune can result an overtuned wrong momentum reconstruction matrix. In other words, they cannot be over used. To optimize the momentum matrices, the experiment must look for additional data from a heavier target for help.

3.9.15 A1 Data Involved in the Matrix Optimization

The analysis needed the involvement of a heavy mass system (at least $A \geq 7$) in the momentum matrix optimization. The only possibility was the end caps of the target cells were made of 7075 aluminum alloy. The alloy contains about 90%

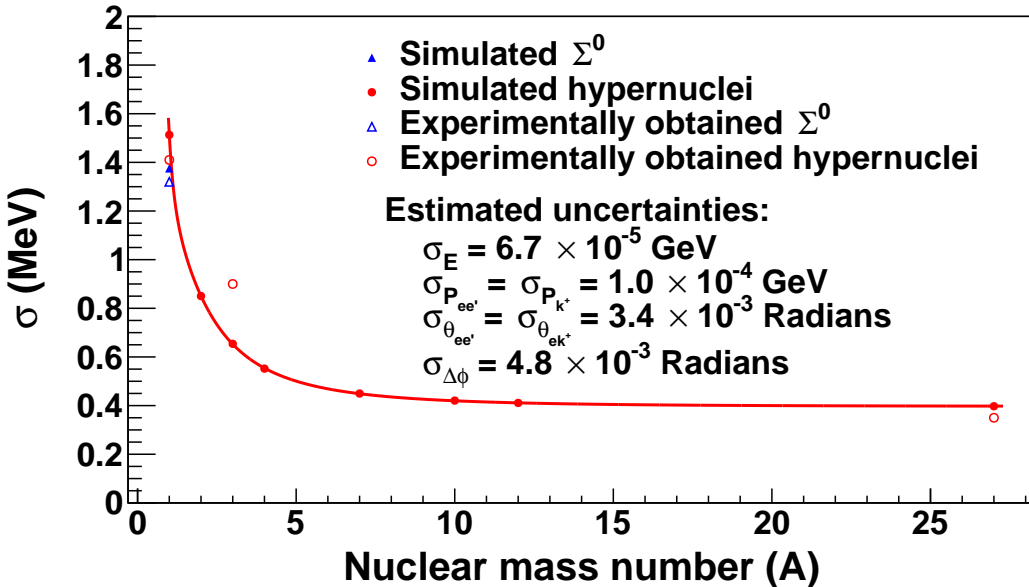


Figure 3.30. The two dimensional correlation between the nuclear mass number (A) and simulated resolution (σ).

Table 3.5

The comparison between the experiment and simulation.

| Nuclear mass number (A) | Resolution in σ [MeV] (experiment) | Resolution in σ [MeV] (simulation) |
|----------------------------------|---|---|
| 1 (Λ) | 1.41 | 1.51 |
| 1 (Σ^0) | 1.32 | 1.37 |
| 3 (Ann) | 0.9 (measured width) | 0.67 |
| 27 ($^{27}_\Lambda \text{Mg}$) | 0.38 | 0.39 |

of aluminum (^{27}Al), 5.6% of zinc, 2.5% of magnesium, 1.6% of copper, and 0.3% of silicon, iron, manganese, titanium, chromium, and other metals. Since the ^{27}Al was the dominant component, so that the alloy (target cell) was considered as the ^{27}Al . The events were selected from the beam entrance ($-0.14 \text{ m} < \text{average } z\text{-vertex} < -0.11 \text{ m}$) and beam exit ($0.11 \text{ m} < \text{average } z\text{-vertex} < 0.14 \text{ m}$) end caps and then combined together to produce the spectroscopy of the $^{27}_\Lambda \text{Mg}$ hypernuclei. The missing mass spectrum of ^{27}Mg before involving events from the aluminum end caps in the momentum matrix tune is shown in Fig. 3.31.

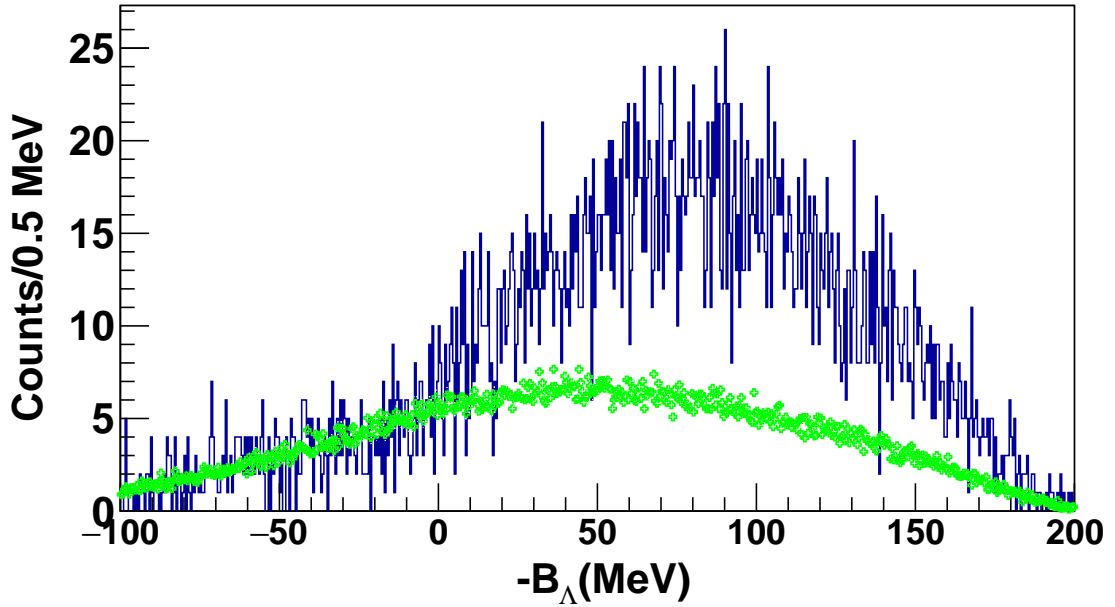


Figure 3.31. The ${}_{\Lambda}^{27}\text{Mg}$ spectrum before the Al data involved in the matrix tune. The events from the beam entrance and beam exit aluminum windows were selected and combined together to produce the ${}_{\Lambda}^{27}\text{Mg}$ hypernuclei. To calculate the missing mass in terms of binding energy (B_{Λ}), the missing mass of the ${}_{\Lambda}^{27}\text{Mg}$ is calculated first and then the rest mass of the ${}_{\Lambda}^{27}\text{Mg}$ is subtracted. The distribution formed by the green crosses represents the accidental background shape. The distribution above the accidental distribution is the quasi-free distribution.

There were several limiting factors. First of all, the Q^2 and 3-momentum transfer to the Λ were $0.5 (\text{GeV}/c)^2$ and $400 \text{ MeV}/c$, respectively, for the E12-17-003 kinematic configuration. The cross sections for all the bound states in such case would be reduced significantly, especially more severe for the ground state which has the Λ at s-shell coupled to the core nucleus ${}^{26}\text{Mg}$ at ground state. Secondly, with the T kinematics the correlation of the ground state missing mass is located above the Λ (H/H) line (see Fig. 3.21) so that it was not favored by the kinematics acceptance. Furthermore, the HRS had smaller solid angle acceptance for the "targets" located at $z = \pm 12.5 \text{ cm}$. Finally, the missing mass resolution at the initial stage was poorer than $1.7 \text{ MeV} (\sigma)$ as the momentum matrices were tuned only using Λ and Σ^0 .

Because of these, no spectroscopy of bound structures could be obviously recognized in the region from $-B_\Lambda = -20$ to 10 MeV.

Therefore, a peak or mass region search test was performed to find the events that were possibly from either a single particle state or from a group of states with their spin-orbital separations significantly smaller than the achievable resolution. Events from such a state should have a well defined mass. Since the selected region did not contain sufficient amount of events above the background, a sufficiently high statistical weight was given to the χ^2 contributed by these selected events for the matrix tune. When such a location was found, the spectroscopy of $^{27}_\Lambda\text{Mg}$ in the threshold region appeared improving at the same time the width of Λ and Σ^0 were also improved further. This is because the contribution from the momentum uncertainty was reduced by the optimization tune with heavy mass involved. Due to the domination of the contribution from the angular uncertainty, such improvement was small ($< 1\%$) as expected. Furthermore, the masses of Λ and Σ^0 remain uncharged from their PDG values (shift $< \sim 0.02$ MeV). In addition, no enhancement effect was seen from the accidental background distribution at the same peak positions. In contrast, no such response could be observed at the location where the gated events were not likely from a single defined mass.

During such searching and pre-optimization procedure, a bound and a few unbound structures showed up in the $^{27}_\Lambda\text{Mg}$ spectrum. Since the bound structure did not have sufficient events, therefore the events were also selected from the unbound structures and involved in the matrix tune along with the Λ and Σ^0 masses. The aluminum events were given a high statistical weight so that they could have a dominant contribution to the χ^2 , whereas the Λ and Σ^0 were given a lowest allowable statistical weights to lock precisely the calibrated missing mass scale. Then the HRS momentum matrices were tuned alternatively and very lightly with only few (up to 3 maximum) iterations at a time. Since their ($^{27}_\Lambda\text{Mg}$ peaks) masses were unknown, the

fitted means were used to be the nominals. These means had to be fitted for each cycle of tune in order to get the nominals for the next cycle of tune. Once the peaks become clear and stable, the initial tuning was stopped.

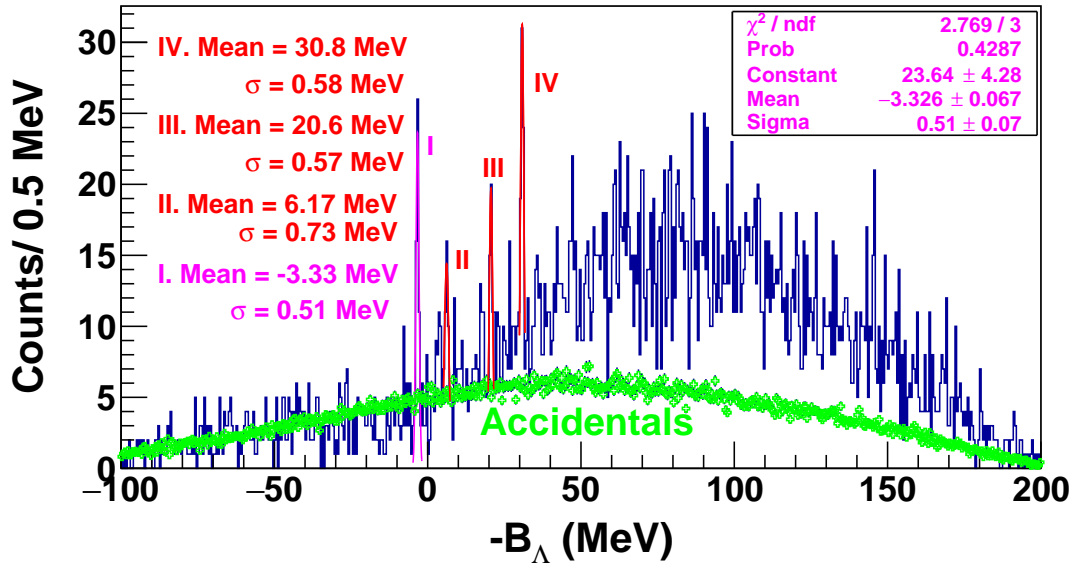


Figure 3.32. The ${}_{\Lambda}^{27}\text{Mg}$ spectrum after the initial tune. Four structures are appeared in the ${}_{\Lambda}^{27}\text{Mg}$ hypernuclei. The three at the higher excitation continuum states are much narrower than expected. The four peaks I, II, III and IV are landed at -3.33 MeV, 6.17 MeV, 20.6 MeV, and 30.8 MeV, respectively. The distribution formed by the green crosses represents the accidental background distribution.

Figure 3.32 shows the result from the initial tune. Although the spectrum shows four peaks, the three peaks at the higher excitation appeared too narrower than expected to be the states in the continuum. As the bound structure become much clear, to avoid the overtune, the further momentum optimization focused only on the bound state without involving the events from the higher excitation continuum states. Therefore, in the later optimization, events from only the bound state were selected. For the final tune, the statistical weight for the aluminum events (bound state only) and Λ and Σ^0 reoptimized and the momentum matrices were tuned until the χ^2 was saturated. Actually, the process of the momentum matrix optimization was completed when the peak width of the bound state was stabilized at the value

in close agreement with the prediction given by the resolution simulation. With the optimized momentum matrices, the width of the Λ and Σ^0 appeared also in a good agreement with the predicted values from the simulation. After the complete optimization, the two structures in the $^{27}\Lambda\text{Mg}$ continuum, the peaks #II and #III in the initially tuned spectrum showing in Fig. 3.32, were significantly smeared. The 4th peak located at the higher excitation continuum state is still alive but is broadened by about 3 times.

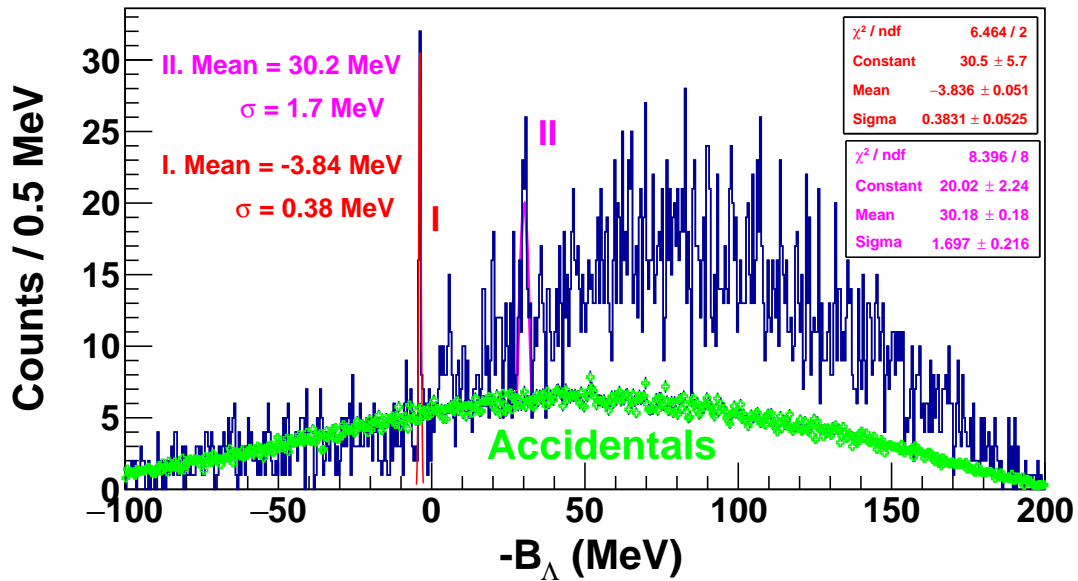


Figure 3.33. $^{27}\Lambda\text{Mg}$ spectrum after involving the Al data in the matrix tune. The missing mass of $^{27}\Lambda\text{Mg}$ is calculate in terms if binding energy. To calculate the binding energy, the missing mass of $^{27}\Lambda\text{Mg}$ is calculated first and then the rest mass of the $^{27}\Lambda\text{Mg}$ is subtracted. Here, I and II are the two peak structures obtained after the momentum optimization. The mean of the peak I and II are landed at - 3.84 MeV and 30.2 MeV, respectively. The distribution formed by the green crosses represents the accidental background shape. The distribution above the accidental background distribution is the quasi-free distribution.

The finalized spectroscopy is shown in Fig. 3.33. After the final tune, only two structures are alive, one is a bound state and another is a high excitation continuum state. The peak means stabilized at $-B_\Lambda = - 3.84 \pm 0.051$ MeV and 30.2 ± 0.18 MeV, respectively. Figure 3.34 gives a closer view of these two structures and their

ittings. The first bound structure has a width of 0.38 ± 0.052 MeV in σ (or 0.89 MeV FWHM). According to the simulation with all the estimated uncertainties, this width or missing mass resolution appeared to correspond to the ultimate HRS momentum resolution. Since the ground state of $^{27}_{\Lambda}\text{Mg}$ is expected to have its binding energy $-B_{\Lambda}$ in the range from -12 to -16 MeV but did not appear in this spectrum, the observed bound structure is likely to be a structure with Λ in p-shell. It may be mixed with couple of spin-orbital states with very small separation energy (< 100 keV). On the other hand, the other clearly seen structure is at quite high excitation with $-B_{\Lambda} = 30.2 \pm 0.18$ MeV with a width of 1.7 ± 0.22 MeV in sigma (or 4.0 MeV FWHM). It is unusual to see a highly excited state with rather narrow width. Thus, its natural is not clear. Nevertheless, the stabilized widths of the bound structure of $^{27}_{\Lambda}\text{Mg}$, the Λ , and Σ^0 , that agreed well with the prediction given by the simulation showed that the HRS momentum resolution had reached to its ultimate level.

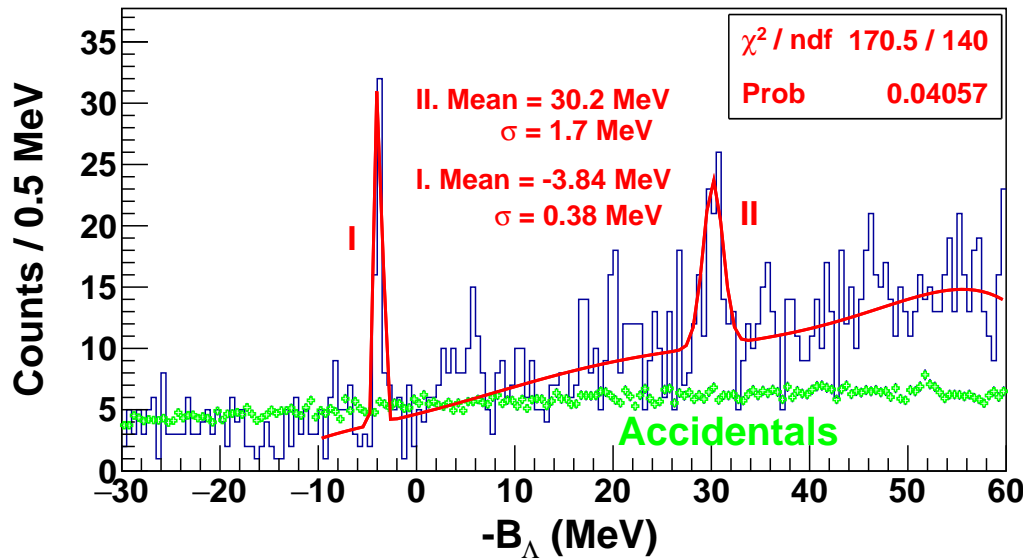


Figure 3.34. To make a clear observation of the observed states, the $^{27}_{\Lambda}\text{Mg}$ is plotted with reduced x-axis plotting range. The missing mass is calculated in terms of binding energy. To calculate the binding energy, the missing mass of $^{27}_{\Lambda}\text{Mg}$ calculated and then the rest ass of the $^{27}_{\Lambda}\text{Mg}$ is subtracted from the calculated missing mass.

CHAPTER 4

RESULT AND DISCUSSION

4.1 Reconstructed Λ and Σ^0 Missing Masses

After complete optimization of the system, the Λ and Σ^0 missing masses obtained by analyzing the H/H data was found to be $1115.68 \pm 0.049 \text{ MeV}/c^2$ and $1192.62 \pm 0.086 \text{ MeV}/c^2$, respectively, with a separation of $76.94 \pm 0.099 \text{ MeV}/c^2$ (see Fig. 4.1). These obtained masses and separation in comparison to their published values [1] are summarized in Table 4.1. The peak width was found to be $\sigma = 1.41 \pm 0.05 \text{ MeV}$ ($\text{FWHM} \approx 3.31 \text{ MeV}$) for Λ and $\sigma = 1.32 \pm 0.076 \text{ MeV}$ ($\text{FWHM} \approx 3.1 \text{ MeV}$) for Σ^0 . These achieved widths agreed with the simulation with the estimated uncertainties within $100 \text{ keV}/c^2$ (see Table 3.5). Therefore, the systematic uncertainties in the absolute binding energy scale are significantly small in comparison to the statistical uncertainty.

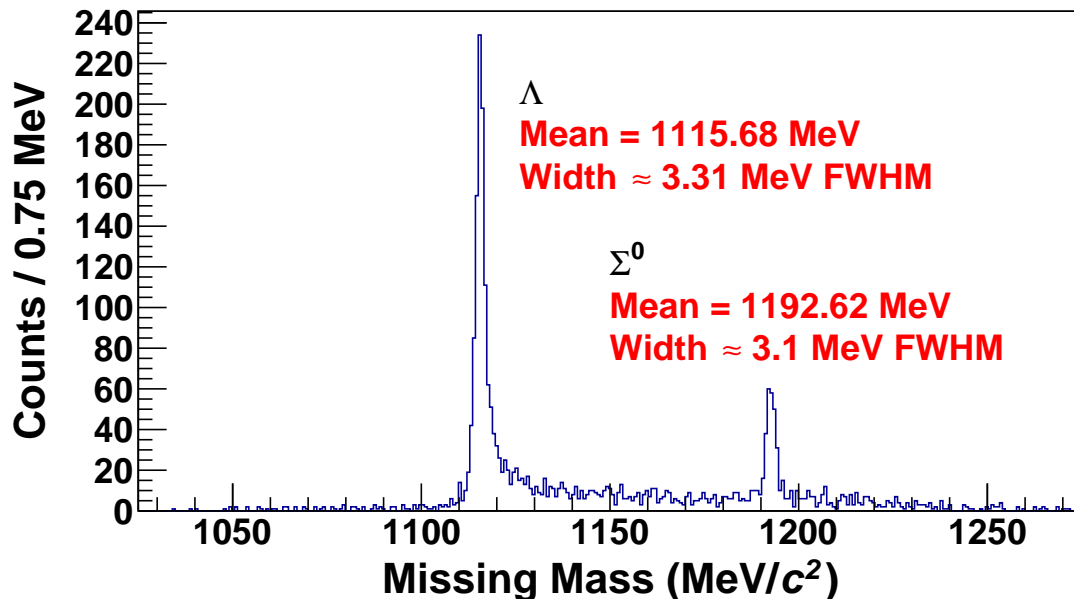


Figure 4.1. The missing mass spectroscopy of the free Λ and Σ^0 obtained by analyzing the H data in the H kinematics.

Table 4.1

Summary of the obtained masses of Λ and Σ^0 , and their separation in comparison to the values from Ref. [1].

| Particle | Obtained [MeV/c^2] | Published [MeV/c^2] |
|------------|------------------------|-------------------------|
| Λ | 1115.68 ± 0.049 | 1115.683 ± 0.006 |
| Σ^0 | 1192.62 ± 0.086 | 1192.642 ± 0.024 |
| ΔM | 76.94 ± 0.099 | 76.959 ± 0.025 |

Figure 4.2 shows the Λ missing mass obtained by analyzing the H data in the tritium kinematics in which the Σ^0 is out of the kinematics acceptance. The Λ from tritium kinematics is also landed at its known mass, $1115.68 \pm 0.077 MeV/c^2$ with a resolution of $\sigma = 1.42 \pm 0.075 MeV$ ($FWHM \approx 3.33 MeV$).

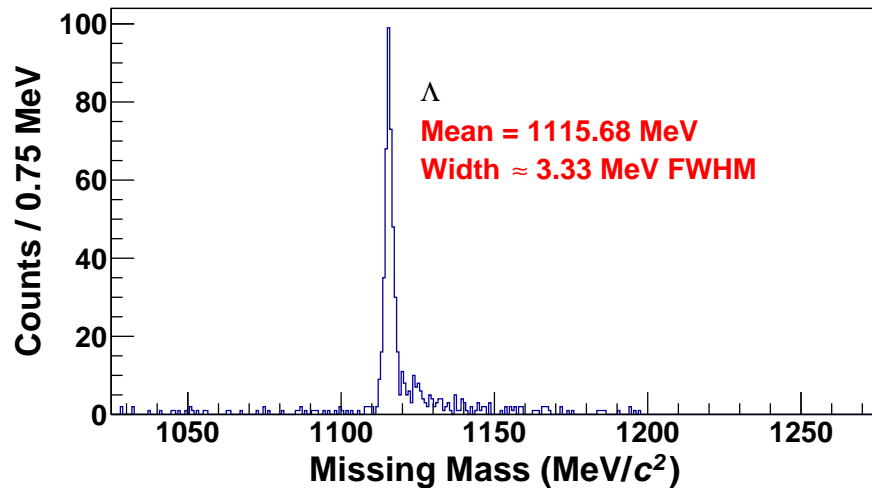


Figure 4.2. The missing mass spectroscopy of the free Λ obtained by analyzing the H data in the T kinematics.

4.2 Systematic Uncertainty

The systematic uncertainty for the binding energy are originated from the following sources.

1. According to the particle data book [1], the masses of Λ and Σ^0 are 1115.683 ± 0.006 MeV and 1192.642 ± 0.024 MeV, respectively. These errors contribute for the systematic uncertainty.
2. The momentum matrices were optimized with the known masses of Λ and Σ^0 . After the optimization, the masses of Λ and Σ^0 were fitted to 1115.68 ± 0.049 MeV and 1192.62 ± 0.086 MeV, respectively. These errors also contribute for the systematic uncertainty.

After combining all of the contributions, the total systematic error is calculated as:

$$\text{Total systematic error} = \sqrt{6^2 + 24^2 + 49^2 + 86^2} \text{ keV} = 102 \text{ keV}. \quad (4.2.1)$$

Therefore, a total systematic error of ~ 100 keV was found.

4.3 H Contamination

As reported by the E12-11-112 experiment, which took the data before the $(e, e' K^+)$ experiment with the same tritium target, there was about 2% of H contamination in the tritium gas. To confirm this the tritium data was then analyzed by assuming proton mass for the target and the Λ mass as the threshold mass. A clear peak appeared at $B_\Lambda = 0$ MeV (i.e. right at the Λ mass) above the 3-body continuum broadened by the wrong kinematics, see Fig. 4.3. Existence of this peak at the Λ mass verified the presence of H in the tritium gas. The overlaid distribution shown by the green crosses represents the accidental background which was fitted using a 6th order polynomial function by a separate background analysis. Then the distribution above the accidental background was fitted (shown by the solid red line) by a 7th order polynomial function for the 3-body continuum combined with a Gaussian with

its mean at $B_\Lambda = 0$ and the width obtained from the Λ peak (shown in Fig. 4.2). The Gaussian shown separately by the blue dashed-line represents the free Λ 's produced by the H contamination in the T gas. The amount of such events was estimated to be about 100 counts, corresponding to about 2% contamination, agreed with that claimed by the other tritium experiment.

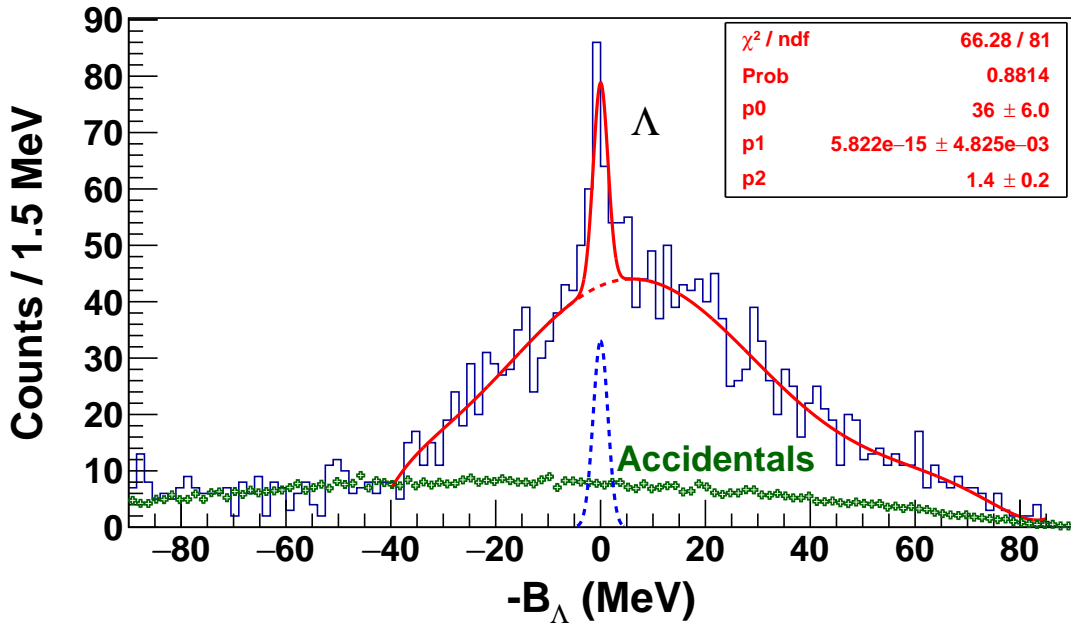


Figure 4.3. Tritium data is analyzed with H kinematics. To calculate the missing mass in terms of binding energy, the missing mass is calculated first by considering the proton as target instead of tritium and then the Λ mass is subtracted from the calculated missing mass. The distribution formed by the green crosses represents the accidental background shape. The distribution above the accidental background distribution is the tritium quasi-free distribution under the wrong kinematics. Because of the wrong target mass, the quasi-free has a broad distribution. The clear peak on the top of the quasi-free distribution (at $B_\Lambda = 0$ MeV) shows the presence of H in the tritium gas. The blue-dashed Gaussian curve gives the free Λ from hydrogen contamination.

Consequently, these 100 free Λ events were expected to appear in the Ann spectrum with a kinematic broadening due to the incorrect tritium target mass assumption. In order to obtain the peak position and the broadened width, the H data taken by the T kinematics (shown by the spectrum in Fig. 4.2) was re-analyzed by assuming the T target mass. The obtained spectrum is shown in Fig. 4.4. The free Λ peak thus

was expected to locate at $B_\Lambda = 48.3$ MeV with a width of 6.4 MeV in σ and total number of counts would be 100 in the Ann spectrum.

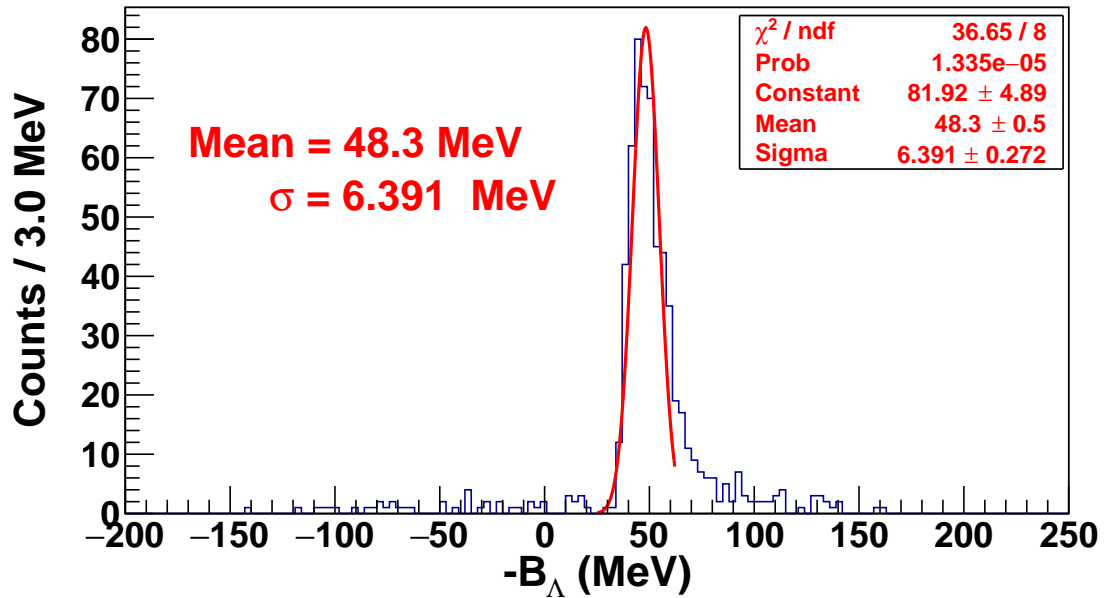


Figure 4.4. The binding energy spectrum obtained by analyzing the H/T data by considering the tritium as target mass and Ann as a recoil mass. To calculate the binding energy, the missing mass is calculated by considering the tritium as target instead of H and then the rest mass of the Ann system is subtracted. Because of the wrong target mass, the spectrum is broadened by about 5 times.

4.4 Mass Spectroscopy Obtained from the T Target

Using all the optimized matrices, a missing mass spectrum represented by the Λ binding energy was produced from the T data analysis. The threshold mass ($B_\Lambda = 2994.814 \text{ MeV}/c^2$) was defined by the rest mass sum from Λ and $2n$. This spectrum is shown in Fig. 4.5.

The distribution formed by the green crosses represents the accidental background contained in the spectrum. A detailed discussion about the accidental background shape can be found in the following section. The distribution above the accidental background is the combination of the quasi-free productions of Λ , Σ^0 , and Σ^- ; the

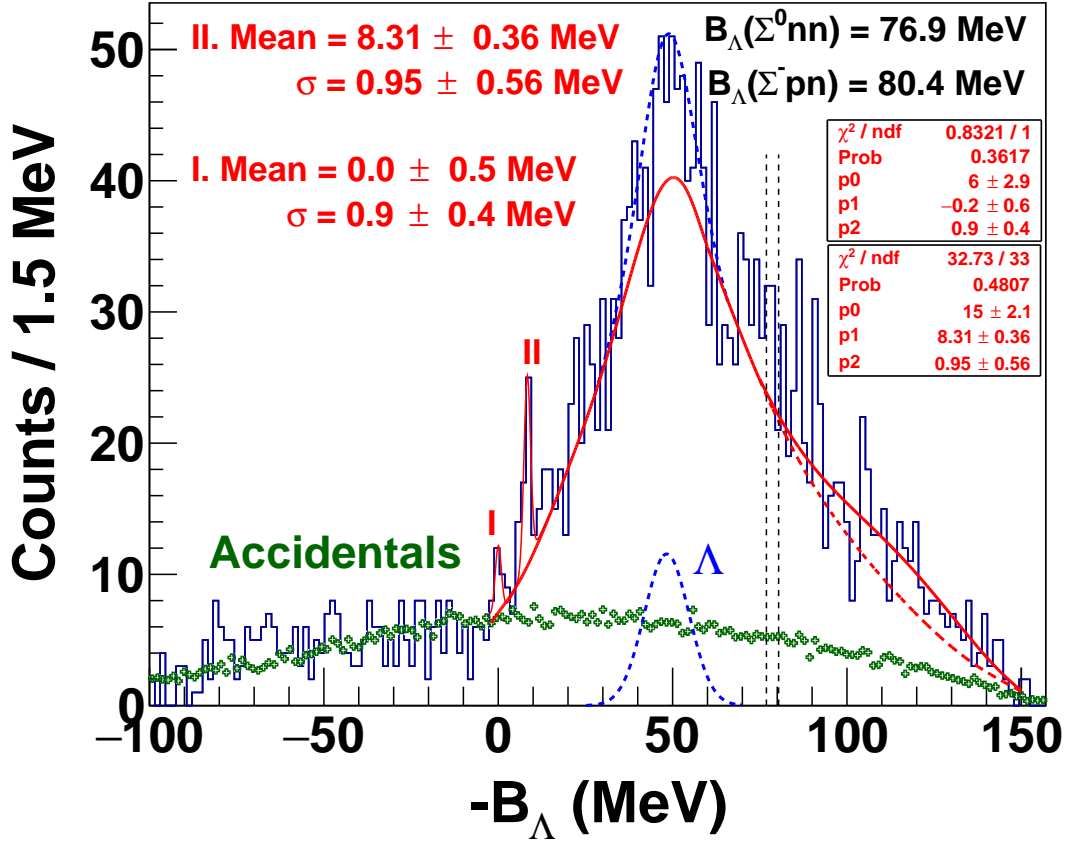


Figure 4.5. The mass spectroscopy of ${}^3_{\Lambda}\text{n}$ hypernuclei in terms of binding energy after involving the aluminum data in the matrix tune. The distribution formed by the green crosses represents the accidental background shape. The red curves give the simulated Λ and Σ quasi-free distributions and blue-dotted curve is the free Λ from H contamination (kinematically broadened). For the first peak (I) the χ^2/NDF is 0.83 and for the second peak (II) it is 0.99.

free Λ production from the H contamination; and of course the possible existence of the structures of Λn and Σnn .

The red solid line above the accidental background distribution represents the combined quasi-free production distributions from Λ , Σ^0 , and Σ^- . The red dashed-line represents the tail of the Λ quasi-free production distribution, above which is the quasi-free production with combined contributions from the $\Sigma^0\text{nn}$ and $\Sigma^-\text{pn}$ channels.

These distributions were simulated using the Hall C SIMC code, with the momentum distribution of a nucleon in the three-body baryonic systems [71], by an early

Hall C (E91-016) ($e, e' K^+$) experiment [72] done in 1996. The studies of that experiment included the ${}^3_{\Lambda}H$ spectroscopy [73]. Since E12-17-003 has the identical Q^2 in the electron scattering process and 3-momentum transfer from the virtual photon to the recoil Λ particle, the characteristic quasi-free distribution should be identical. There are two major differences. Since the three nucleons in T (3H) are pnn compared with ppn in 3He , the yield rate of quasi-free Σ^- channel relative to that of Λnn and $\Sigma^0 nn$ is increased by a factor of two. Secondly, this E12-17-003 experiment has much smaller kinematics acceptance. Such acceptance reduction factor as a function of the binding energy can be extracted from the ratio of the accidental background shapes between the two experiments. For E12-17-003, the Σ quasi-free productions were severely cut off by the limited kinematic acceptance. The red solid line was then obtained scaling the existing simulation which agreed well with the E91-016 data but taking into account the above two factors. In addition, it had to also take into account the accidental background distribution which was precisely fitted by a 6th order polynomial function. Finally, the overall combined quasi-free distribution was normalized up to the limit which allowed to taking into account of the 100 counts of free Λ 's from the 2% H contamination, which is presented by the blue-dashed line.

Accidental Background Analysis

For the physics data analysis, the coincidental K^+ 's were selected within the ± 1 ns coincidence time window (see Fig. 3.10). The accidental events (formed by the accidental coincidence between the π^+ 's and protons) within the ± 1 ns coincidence time window cannot be identified and removed. These accidental events form the accidental background distribution in the physical mass spectroscopy (see Fig. 4.5) which is represented by the green crosses. To minimize the statistical fluctuation in the accidental background distribution, 38 small accidental peaks were selected as a coincidence time gate and then the events were gated from the selected accidental

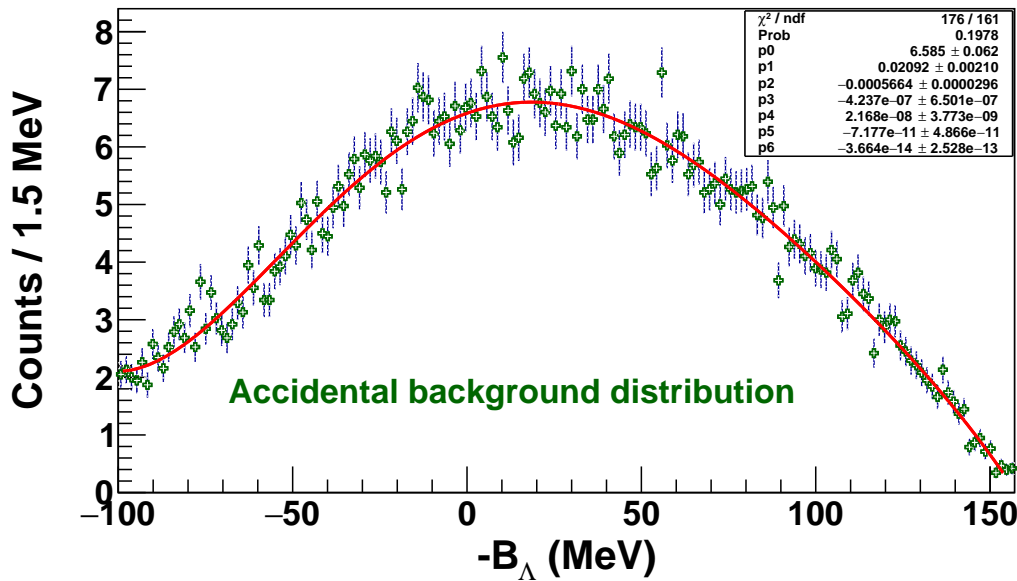


Figure 4.6. The accidental background distribution fitted with a 6th order polynomial. To minimize the statistical fluctuation in the accidental background shape, the events were selected from 38 small accidental peaks from the coincidence time spectrum (see Fig. 3.10) and then the obtained missing mass distribution was scaled down by 38.

peaks. Finally, the obtained missing mass distribution was scaled down by 38. In order to measure the accidental background shape precisely, the accidental background distribution was fitted with the higher order (from 2nd order to 9th order) polynomials. Finally, the best fitting result, with $\chi^2/\text{NDF}=1.09$, was found with the 6th order polynomial (see Fig. 4.6). Therefore, the accidental background shape is well known and precisely measured.

4.5 Possible Observation of the Ann Continuum Structures (Resonances)

The Ann threshold region was the experimentally interested region near which two small peaks were observed. The background simulations with the same statistics showed that they are distinguished from the statistical fluctuations. The first peak appears to be the possible resonance for which the experiment was looking but the

yield rate is 8 to 10 times lower than expected. This resonance corresponds to the pure ($T=1$) $^3\Lambda n$ state, however the statistics is very low. With such low statistics and high background fitting was very difficult because there were not enough bins for the precise fitting. Thus the fitting was done by two different ways. The Gaussian has three parameters and the precise fitting to this spectrum requires the parameters on the background shape as well as on the quasi-free shape. If all of these details were included, there would be no number of degrees of freedom left and fitted value itself has very low confidence level. Therefore, the peak was fitted with the smallest possible bin size over an estimated constant background with the fitting range covered the peak only. The mean of the fitted peak was slightly bound ($-B_\Lambda = -0.2$ MeV) due to underestimate the rising quasi-free distribution. For the second way of fitting, sufficient number of bins were obtained by widening the fitting range from $-B_\Lambda = -1$ to 7 MeV. A 2nd order polynomial function was included in the fitting for the combination of the accidental background and the quasi-free distribution. In this case the fitting was dominated by the background and quasi-free distribution thus the result was slightly unbound ($-B_\Lambda = 0.2$ MeV). Both of the fittings have the similar level of uncertainties. The final result is taking the statistical average over the two independently fitted results and shows that the binding energy of the first peak is $B_\Lambda = 0.0 \pm 0.5$ MeV with a peak width of 0.9 ± 0.4 MeV in σ . Because of the low statistics and high background the uncertainties are large. The simulation of the missing mass resolution as a function of nuclear mass number A , with the estimated uncertainty contributions, predicted that the intrinsic missing mass resolution for the $A = 3$ system should be around $\sigma = 0.67$ MeV. Therefore, the natural width ($\Gamma/2$) of this peak is about 0.6 MeV, if this peak is real. The second peak is slightly more prominent in terms of statistics. It is located at 8.31 ± 0.36 MeV and has peak width of 0.95 ± 0.56 MeV. It appears to be an unbound continuum resonance. However, since unbound di-neutrons system does not exist, thus a Λnn resonance at

such high excitation was not expected and therefore, its origin is unclear. Due to low statistics and high accidental background, neither of the peaks have sufficient significance (discussed later) to make a definite identification.

The statistical significances for the observed two possible resonances were found to be 2.1 and 4.5, respectively (the calculation will be discussed in the later Section 4.7). Obviously, the significance for the first peak is insufficient to make solid claim on its existence. However, it cannot be ruled out either. Therefore, further study with higher statistics is needed. If these continuum states are indeed real, their cross sections were found to be 1.3 and 3.66 nb/sr (see Section 4.8).

4.6 Possible Observation of a Bound Σ NN Hypernuclear State

Another highly interesting observation is around the region of the Σ thresholds. To make a clearer observation by reducing the statistical fluctuation, the spectrum was plotted again with a larger bin size, as shown in Fig. 4.7. The two Sigma thresholds, indicated by the two vertical black dashed-lines, are at $B_\Lambda(\Sigma^0\text{nn}) = 76.9$ MeV and $B_\Lambda(\Sigma^-\text{pn}) = 80.4$ MeV. There is another threshold for Σ^-d located in between these two 3-body threshold but not shown in the figure.

An enhancement, just below the Σ thresholds, is visible. A Gaussian fit was done with the known quasi-free distribution, as shown by the dashed-line in magenta color. It hints a peak at $B_\Lambda = 74.3 \pm 0.4$ MeV or $\sim 2.6 \pm 0.4$ MeV below the $\Sigma^0\text{nn}$ threshold. The peak width is 3.5 ± 0.5 MeV (~ 8.2 MeV FWHM). The statistical significance was found to be 3.1 and the cross section upper limit was 8 nb/sr.

The bound $A = 3$ and 4 Σ hypernuclei were predicted long ago, however only an $A = 4$ Σ hypernuclei (${}^4_\Sigma\text{He}$) was observed by the experiment using the ${}^4\text{He}(K^-, \pi^-)$ reaction at BNL-AGS [74]. At Jefferson Lab both the $A = 3$ and $A = 4$ Σ hypernuclei were also studied by the early ($e, e'K^+$) experiment E19-016 [72, 73] by using the ${}^3\text{He}$ and ${}^4\text{He}$ targets, however, no visible signature was found in the spectra above the

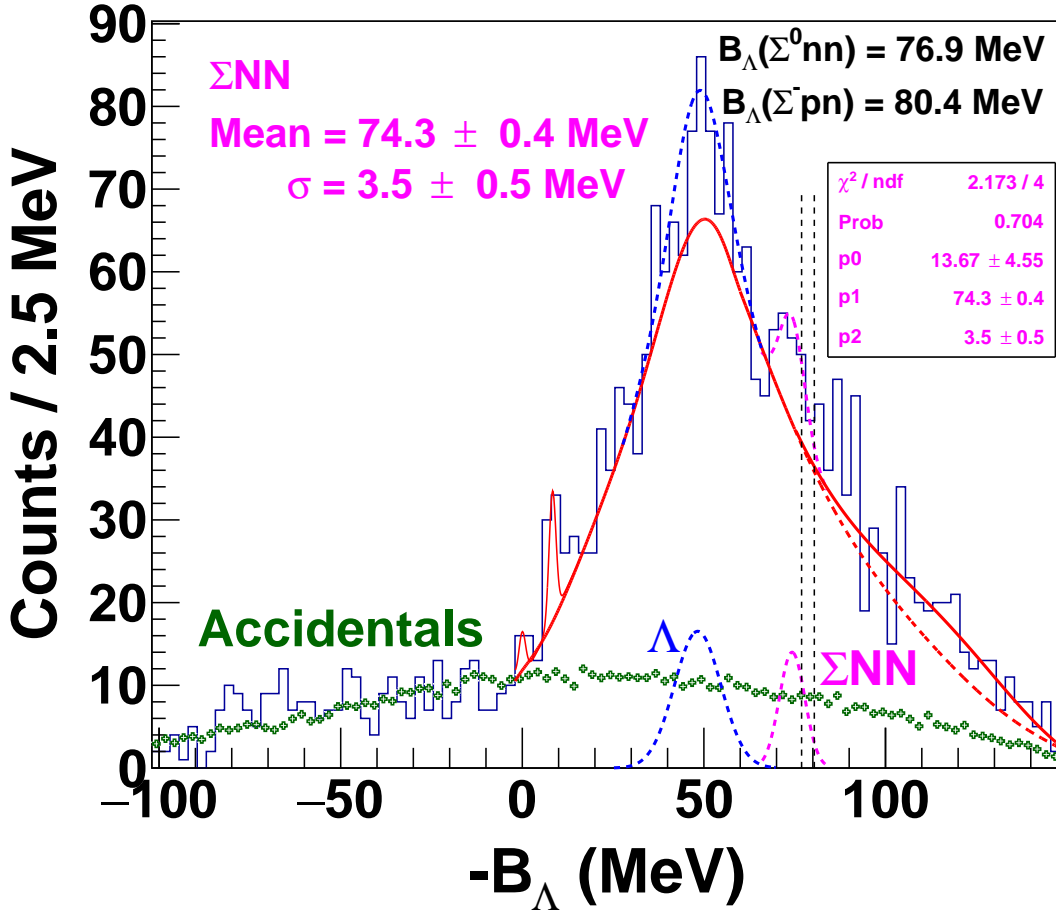


Figure 4.7. The mass spectroscopy of $^3_{\Lambda}n$ hypernuclei plotted with a larger bin size (2.5 MeV/bin) in terms of binding energy B_{Λ} . The spectrum is plotted with the system optimized with involving the aluminum data in the matrix tune. The magenta-dotted curve shows the fit for the bound state of ΣNN hypernucleus. The ΣNN peak is fitted over a known QF shape with $\chi^2/NDF = 0.55$.

quasi-free distribution. For the E12-17-003 experiment, the Σ^0 production threshold is lower which indicates that the observed enhancement may likely be a bound $^3_{\Lambda}n$ hypernuclei, although more statistics are required to make a definite identification. If it can be confirmed, the finding can be quite significant as it can be extremely important in helping to investigate the poorly known Σ -N interaction.

4.7 Statistical Significance

From the data analysis, three peaks are observed. The observed peaks are highly interesting, however the statistics is not sufficient enough to solidly confirm the observed peaks. Therefore, the statistical significance is calculated to see whether the findings are really significant or not. In another words, the statistical significance is a way of mathematically proving that a certain statistic (peak) is reliable. Generally, if the mathematically calculated significance is large enough (> 5), the observed peak can be solidly conformed. The details about the statistical significance can be found in Ref. [1] and [75]. The statistical significance is calculated by using the following mathematical relation:

$$S = \sqrt{2((s + b) \ln(1 + s/b) - s)}, \quad (4.7.1)$$

where, s and b are the number of signal and background events, respectively. As the accidental background distribution is precisely fitted with a 6^{th} order polynomial with $\chi^2/NDF \approx 1$ (see Fig. 4.6), so that the accidental background is measured accurately. The actual number of events for the signal (s) and background (b) are calculated by selecting region of $\pm 2.5\sigma$ from the observed mean with the help of TGraphical cut and then the selected region was integrated. In this way the signal (s) and background (b) events are measured precisely.

Actually, it is the case where the background events (b) are precisely known (with very small error), therefore the formula given by equation 4.7.1 is used to calculate the statistical significance. However, if the data contains errors or statistical fluctuations, the observed significance will be affected. Another widely used formula to calculate the statistical significance is $S = s/\sqrt{b}$, however in this case the $s + b$ should be large enough and $s \ll b$ [75]. Such conditions are not appeared in our case and therefore

the relation ($S = s/\sqrt{b}$) is not used to calculate the statistical significance. Table 4.2 shows the statistical significance for all three observed peaks.

Table 4.2

The statistical significance for all three observed peaks within the region of $\pm 2.5\sigma$ from the mean.

| Peaks | Statistical significance |
|---|--------------------------|
| First peak (with mean ~ 0.0 MeV) | 2.1 |
| Second peak (with mean ~ 8.31 MeV) | 4.5 |
| Third peak (with mean ~ 74.3 MeV) | 3.1 |

The statistical significance is also calculated by another method. In this method, the total number of counts ($n = s + b$) are measured by selecting the same region as before. The error (d_n) on the total events is calculted by taking the square root of the total counts. The total number of background events (b) and error (d_b) are also calculated. Since the accidental background shape is scaled down by a factor of 38, the error on the background events (d_b) is calculated by taking the ratio of \sqrt{b} to $\sqrt{38}$. Finally, the total error (d_s) is obtained by taking the square root of square sum of the two measured errors. The significance is then calculated by taking the ratio of the total signal events (s) to the total error (d_s). The significance obtained by this method is close ($\sim 5\%$) to that obtained by the equation 4.7.1.

4.8 Cross Section

Since there were H data (H/T) taken with the identical T kinematics and target cell structure, the known cross section of the Λ photo-production measured by the early E91-016 experiment (which had the identical Q^2 and 3-momentum transfer) was used to estimate the upper limit of the differential cross section for the experimentally observed peaks. To determine the cross section, the following factors were considered:

1. The total number of events in the Λ peak in the missing mass spectrum obtained from the H target (H/T) data (see Fig. 4.2) was determined by integrating the whole region of the spectrum including the radiative tail. The accidental background events in the Λ spectrum were subtracted.
2. The total number of events in each of the observed peaks (two Λ n peaks and one Σ N peak) was determined after subtracting the accidental background events.
3. The total accumulated beam charge for each set of the data (H/T and T/T) was obtained by a beam charge analyses.
4. Both of the targets (H/T and T/T) were run under the identical conditions. Therefore, the kaon detection efficiency (ϵ_K), the number of virtual photon N_γ per scattered electron, and the solid angle acceptance of the kaon arm ($\Delta\Omega$) were considered the same for both sets of data and thus canceled during the cross section calculation.
5. The cross section for the Λ production was assumed known to be 400 nb/sr obtained from the early Hall C experiment with the same Q^2 and 3-momentum transfer.

The total number of events acquired from the Λ (H/T) spectrum for the whole run period is:

$$N_\Lambda = N_\gamma \times N_{target}(H_2) \times \frac{d\sigma_\gamma}{d\Omega_k}(\Lambda) \times \Delta\Omega_k \times \epsilon_k \times [\text{Beam Charge (coulomb)}] \times 6.25 \times 10^{18} [\# \text{ of electrons/C}], \quad (4.8.1)$$

where, N_γ is the number of virtual photons per electron, $\Delta\Omega_k$ is the solid angle acceptance of the RHRS, ϵ_k is the kaon detection efficiency (including the kaon survival

rate), and $\frac{d\sigma_\gamma}{d\Omega_k}(\Lambda)$ is the cross section of photoproduction of Λ from H and is known to be ~ 400 [nb/sr]. $N_{target}(H_2)$ is the number of scattering centers (protons) per cm^2 which is calculated as,

$$N_{target}(H_2) = \frac{t(H_2)}{A(H_2)} \times N_A \times N_p(H_2), \quad (4.8.2)$$

where, $t(H_2)$ ($= 0.0708 \text{ gm/cm}^2$) is the mass thickness of the H target, $A(H_2)$ ($= 2.0 \text{ gm/mol}$) is the molecular weight per mol of the H_2 target, $N_p(H_2)$ is the number of protons per molecule for the H_2 target and N_A is the Avogadro's number. With these values, the $N_{target}(H_2)$ was found to be,

$$N_{target}(H_2) = 0.0708 \times N_A [\#/cm^2]. \quad (4.8.3)$$

Similarly, the total number of events generated in the Ann peak is:

$$\begin{aligned} N_{\Lambda nn} = N_\gamma \times N_{target}(T_2) \times \frac{d\sigma_\gamma}{d\Omega_k}(\Lambda nn) \times \Delta\Omega_k \times \epsilon_k \times [\text{Beam Charge (coulomb)}] \times \\ 6.25 \times 10^{18} [\# \text{ of electrons/C}], \end{aligned} \quad (4.8.4)$$

$N_{target}(T_2)$ is the number of scattering centers (protons) per cm^2 for the tritium (T_2) target given by,

$$N_{target}(T_2) = \frac{t(T_2)}{A(T_2)} \times N_A \times N_p(T_2), \quad (4.8.5)$$

where, $t(T_2)$ ($= 0.083 \text{ gm/cm}^2$) is the mass thickness of the tritium target, $A(T_2)$ ($= 6 \text{ gm/mol}$) is the molecular weight per mol for the tritium target, and $N_p(T_2)$ ($= 2$) is the number of protons per molecule for the T_2 target. With these values, the value

of $N_{target}(T_2)$ was found to be,

$$N_{target}(T_2) = 0.0277 \times N_A [\#/cm^2]. \quad (4.8.6)$$

The ratio of the number of events in the Λ (H/T) spectrum to the number of events in the Λnn peak was used to calculate the cross section. Therefore, by taking the ratio of Eq. 4.8.1 and 4.8.4 the cross section can be found as:

$$\frac{d\sigma_\gamma}{d\Omega_k}(\Lambda nn) = 400 [nb/sr] \times 2.556 \times \frac{[\text{Beam Charge (H/T runs)}]}{[\text{Beam Charge (T runs)}]} \times \frac{N_{\Lambda nn}}{N_\Lambda}. \quad (4.8.7)$$

Using Eq. 4.8.7, the cross section for each of the observed peaks was calculated and is summarized in Table 4.3. In the cross section calculation, the kinematic acceptance correction was also taken in to account. The uncertainty for the calculated cross section is originated from the systematic uncertainty and statistical uncertainty. From the E91-016 experiment [72], the cross section of photo-production of Λ from H target is known to be 396.9 ± 41.5 nb/sr. Therefore, the systematic uncertainty is simply $41.5/396.9$. For each observed peak, the statistical significance is calculated (see Section 4.7). The statistical uncertainty is calculated by taking the ratio of the cross section of a peak to the corresponding statistical significance. Finally, the square root of the square sum of the systematic and statistical uncertainty gives the total uncertainty. The total uncertainty is dominated by the statistical uncertainty.

Table 4.3

The cross section for the observed peaks. The uncertainty include the systematic and statistical uncertainty.

| Peaks | Cross section [nb/sr] |
|------------------------------------|-----------------------|
| First peak (with mean = 0.0 MeV) | 1.3 ± 0.628 |
| Second peak (with mean = 8.31 MeV) | 3.66 ± 0.82 |
| Third peak (with mean = 74.3 MeV) | 8.03 ± 2.59 |

CHAPTER 5

SUMMARY AND CONCLUSION

The E12-17-003 experiment was carried out successfully at Jefferson Lab by using a common tritium target in November 2018. The experiment aimed to provide the experimental data for the unknown Λn interaction by investigating the Λnn resonance or the bound state as indicated by the HypHI experiment. The experimental data on the Λn interaction was believed to solve the charge symmetry breaking puzzle in the ΛN interaction.

The main analysis of the experiment depends on the optimizations of the various systems, such as the z-vertex optimization, coincidence time optimization, HRS scattering angles optimization, and HRS momentum optimization. Data was taken with different targets and kinematics to optimize the systems and all of the systems were optimized as required by the experiment. For the HRS momentum optimization, the aluminum data was also involved in the matrix tune along with the known masses of Λ and Σ^0 .

With the optimized system, the Λ and Σ^0 missing masses obtained by analyzing the H/H data was fitted to be 1115.68 ± 0.049 MeV/ c^2 and 1192.62 ± 0.086 MeV/ c^2 , respectively, with a separation of 76.94 ± 0.099 MeV/ c^2 . The peak width of Λ and Σ^0 was found $\sigma = 1.41 \pm 0.05$ MeV (FWHM ≈ 3.31 MeV) and $\sigma = 1.32 \pm 0.076$ MeV (FWHM ≈ 3.1 MeV), respectively. The systematic uncertainty for their masses was studied and found about 100 keV. By analyzing the aluminum data, two possible states were observed in the $^{27}_{\Lambda}\text{Mg}$ hypernuclei, one of them is bound and is located at -3.84 ± 0.051 MeV with a resolution of 0.38 ± 0.052 MeV (σ). A simulation was carried out to see the validation of the optimizations as well as the involvement of the Al data in the matrix tune and it was found that the simulations and experimentally obtained resolutions of Λ , Σ^0 , and bound state of $^{27}_{\Lambda}\text{Mg}$ agreed < 100 keV (σ). This

verified that the optimizations reached their limits and the result with the aluminum data involved was correct.

From this experiment, two possible resonance states of $^3_{\Lambda}n$ and a bound state of $^3_{\Sigma}n$ were observed. The fitted result shows that the first $^3_{\Lambda}n$ peak is located at 0.0 ± 0.5 MeV with a width of 0.9 ± 0.4 MeV (σ), for which the experiment was looking for. A simulation predicted the intrinsic missing mass resolution of the peak to be $\sigma = 0.67$ MeV so that it has a natural width of $(\Gamma/2) \sim 0.60$ MeV, if the peak does exist. The statistical significance and the cross section for this peak were found to be 2.1 and 1.3 nb/sr, respectively. At such statistical significance, it is not sufficient to permit a definite identification, nor definitely exclude its existence. The second $^3_{\Lambda}n$ peak is located at 8.31 ± 0.36 MeV with a width of 0.95 ± 0.56 MeV in σ . The statistical significance and cross section for this peak were estimated to be 4.5 and 3.7 nb/sr, respectively. The peak at such higher excitation was not expected, therefore, its origin is unclear. The third peak is located in the ΣNN bound region. The mean and width of this peak are 74.3 ± 0.4 MeV and 3.5 ± 0.5 MeV (σ), respectively. The statistical significance and cross section for this peak are 3.1 and 8 nb/sr, respectively. These possible observed states are extremely interesting, although the obtained statistics is rather poor.

The main reasons of having such low statistics are because of (1) small cross sections and (2) the unoptimized the experimental configuration and conditions under which the experiment was carried out. The available conditions were certainly feasible but not ideal.

5.1 Future Suggestions

For any future experiment, the Hall A system optimization is highly recommended by considering the following conditions which were not favourable to the current experiment.

1. The two high resolution spectrometers (HRS) were symmetrically positioned at 13.2° with respect to the beam direction which was the lowest possible physical angle for the current HRS system. However, the scattering angle was too large for this experiment producing the large value of Q^2 about $0.5 \text{ (GeV}/c)^2$. Since the Q^2 has the inverse relation with the virtual photon flux factor, the large value of Q^2 would give the small value of the virtual photon flux factor resulting in the low production yield.
2. The path length of the hadron arm was $\sim 26\text{m}$ long which was too large as the K^+ has very short life time. With such large path length, most of the K^+ 's decayed before they passed through the detector system. The long hadron path length allows only about 10% of kaon survival rate.
3. For the kinematics, to provide the affordable momentum to the K^+ 's, the three momentum transferred to Λ was very large about $400 \text{ MeV}/c$, much larger than the threshold fermi momentum ($\sim 270 \text{ MeV}/c$). This makes the higher probability of escaping Λ or Σ^0 without sticking to the nucleons, thus much lower cross section.
4. In the right arm two Aerogel detectors were installed as a KID detector. These detectors were more than 20 years old thus their detection efficiencies were not high enough.

The electroproduction with the $(e, e'K^+)$ reaction and the quality CEBAF beam has proven to be a powerful tool and is unique for investigation on the unknown Λ -n interaction via study of the Λ n resonance. With improvements pointed above, an optimized experiment can have significantly higher statistics with 15-20 times more yield rate than the current experiment.

Some difficulties experienced during the E12-17-003 data analysis. The momentum optimization data was taken with the H target. The analysis showed that the

light mass system ($A = 1$) was highly dominated by the uncertainty contributions from the scattering angles. Therefore, by using the Λ and Σ^0 alone in the matrix tune, it is not possible to reach the experimentally required resolution because the χ^2 definition is not directly related to the momentum. The χ^2 depends on the invariant mass and the invariant mass depends on the angle and momentum. Therefore, to obtain the reliable momentum calibration, the only way to do so is to collect the calibration data with a heavy target with known mass. So that the momentum can be optimized with the known masses of Λ , Σ^0 and one heavy mass system. One such possible heavy mass system could be the ^{12}C because it generates the $^{12}_{\Lambda}\text{B}$ hypernuclear spectroscopy which has a well known ground state.

In addition, the HRS angle calibration data was taken by using a sieve slit (SS) plate. In case of the RHRHS, the thickness of the existing SS plate was not sufficient enough to stop the heavy hadrons that did not pass through the SS holes. Therefore, a whole bunch of hadrons punched through the SS plate and could reach to the focal plane. Because of the large hadronic background, the RHRHS angle calibration took a lot of effort and time. For any future experiment, the update on the SS plate is highly recommended. One way to do so is double the thickness of the SS plate to reduce the punch through particles.

REFERENCES

- [1] M. Tanabashi et al. (Particle Data Group), Phys. Rev. D **98**, 030001 (2018).
- [2] T. Gogami. Spectroscopic reasearch of Λ hypernuclei up to medium-heavy mass region with the $(e, e'K^+)$ reaction, Ph.D. Thesis, Tohoku University, Japan (2014).
- [3] C. Rappold et al. Phys. Rev. C **88** 041001(R) (2013).
- [4] J. Alcorn et al. Nucl. Inst. Meth. A**522**, 294 (2004).
- [5] R. C. Torres. Two-Nucleon Short-Range Correlations in Light Nuclei, Ph.D. Thesis, MIT (2020).
- [6] T. T. Kutz. Deep inelastic scattering from $A = 3$ nuclei: Nucleon structure and EMC effect, Ph.D. Thesis, Stony Brook University (2019).
- [7] T. Su. Measurement of F_2^n/F_2^p from Deep Inelastic Electron Scattering Off A=3 Mirror Nuclei at Jefferson Lab, Ph.D. Thesis, Kent State University (2020).
- [8] H. Liu. Measurement of the Ratio of the Neutron to Proton Structure Functions, and the Three-Nucleon EMC Effect in Deep Inelastic Electron Scattering Off Tritium and Helium-3 Mirror Nuclei, Ph.D. Thesis, Columbia University (2020).
- [9] C. Amsler, T. DeGrand, and B. Krusche. Quark Model, Phys. Lett. B **667**, 1 (2008).
- [10] T. Yamada et al. Phys. Rev. C **38**, 854 (1988).
- [11] S. Ajimura et al. Nucl. Phys. A 639, 93c (1998).
- [12] H. C. Bhang et al. Nucl. Phys. A 639, 269c (1998).

- [13] M. Danysz and J. Peniewski. Phil. Mag. 44, 348 (1953).
- [14] D. Kawama. Investogation of High-precision Λ Hypernuclear Spectroscopy via the $(e, e' K^+)$ Reaction, Ph.D. Thesis, Tohoku University (2011).
- [15] P. Bydzovsky and A. Gal J. Mares. Topics in Starngeness Nucleus Physics (2007), Lecture Notes in Physics Vol. 724 (Springer Heidelberg 2007).
- [16] S. Nagao. Deacy Pion Spectroscopy of Electro-produced Hypernuclei, Ph.D. Thesis, Tohoku University (2015).
- [17] P. H. Pile et al. Phys. Rev. Lett. **66**, 2585 (1991).
- [18] T. Hasegawa et al. Phys. Rev. Lett. **74**, 224 (1995).
- [19] H. Hotchi et al. Phys. Rev. C **64**, 044302 (2001).
- [20] T. Miyoshi et al. Phys. Rev. Let. **90**, 232502 (2003).
- [21] L. Yuan et al. Phys. Rev. C **73**, 044607 (2006).
- [22] M. N. Rosenbluth. Phys. Rev. **79**, 615 (1950).
- [23] A. Feliciello and T. Nagae. Rep. Prog. Phys. **78**, 096301 (2015).
- [24] L. Tang et al. Phys. Rev. C **90**, 034320 (2014).
- [25] T. Gogami et al. Nucl. Instrum. Meth. A**900** (2018) 69.
- [26] W. M. Alberico and G. Garbarino. arXiv:nucl-th/0112036v1.
- [27] I. Vidana. arXiv:1803.00504v1 [nucl-th].
- [28] A Pérez-Obiol et al. 2014 J. Phys.: Conf. Ser. **503** 012033 .
- [29] T. Seva. Experimental Study of Hypernuclei Electroproduction by High Precision Spectroscopy, Ph.D. Thesis, University of Zagreb (2009).

- [30] Alexander et al. Phys. Rev. Vol. 173, 5 (1968).
- [31] Σp Scattering Experiment at J-PARC Results of Commissioning Run.
<https://aip.scitation.org/doi/pdf/10.1063/1.5118374>.
- [32] A. Gal. Phys. Lett. B 744 (2015) 352-357.
- [33] G. A. Miller, A. K. Opper, and E. J. Stapperson. Annu. Rev. Nucl. Part. Sci. 56 (2006) 253.
- [34] R. Machleidt and H. Muther. Phys. Rev. C **63** (2001) 034005.
- [35] A. Esser et al. Phys. Rev. Lett. **114**, 232501 (2015).
- [36] T. O. Yamamoto et al. Phys. Rev. Lett. **115**, 222501 (2015).
- [37] D. Gazda and A. Gal. Nucl. Phys. A **954**, 161 (2016).
- [38] H. Kamada et al. EPJ Web Conf. **113** 07004 (2016).
- [39] I. Filikhin, V. Suslov, and B. Vlahovic. EPJ Web Conferences **113** 08006 (2016).
- [40] I. R. Afman and B. F. Gibson. Phys. Rev. C **92**, 054608 (2015).
- [41] C. Leemann, D. Douglas, and G. Krafft. Ann. Rev. Nucl. Part. Sci. **51**, 413 (2001).
- [42] K. de Jager. Nucl. Phys. A **737**, 301 (2004).
- [43] L. Y. Zhu et al. Phys. Rev. C **71**, 044603 (2005).
- [44] F. Garibaldi et al. Phys. Rev. C **99**, 054309 (2019).
- [45] https://hallaweb.jlab.org/equipment/beam/energy/arc_web.html.

- [46] J. Karn et al. Development of Digital Feedback Systems for Beam Position and Energy at the Thomas Jefferson National Accelerator Facility, Conference paper (1997).
- [47] V. Lebedev R. Dickson. Fast digital feedback system for energy and beam position stabilization, Conference paper (1999).
- [48] P. Chevtsov et al. Operational experience with synchrotron light interferometers for CEBAF experimental beam lines.
- [49] Hall A Operational Manual, Jfferson Laboratory.
- [50] T. Hague. Measurement of the EMC Effect of the Helium-3 Nucleus at Jefferson Lab, Ph.D. Thesis, Kent State University (2020).
- [51] Hall A Rasters. <https://hallaweb.jlab.org/wiki/index.php/Raster>.
- [52] W. Barry et al. Basic Noise Considerations for CEBAF Beam Position Monitors, JLAB-TN-91-087 (1991).
- [53] Jefferson Lab Hall A Standard Equipment Manual Version 2017. <https://hallaweb.jlab.org/github/halla-osp/version/Standard-Equipment-Manual.pdf> .
- [54] D. Nguyen. The Isospin Dependence of Short Range Correlations through Inclusive Electron Scattering ^{40}Ca and ^{48}Ca , Ph.D. Thesis, University of Virginia (2018).
- [55] S. N. Santiesteban et al. Nucl. Inst. Meth. A 940 (2019) 351-358.
- [56] Y. Wang. Measurements of Elastic ep Cross Section at $Q^2 = 0.66, 1.10, 1.51$, and 1.65 GeV^2 , Ph.D. Thesis, College of William & Marry (2017).
- [57] J. Alcorn et al. Nucl. Inst. Meth. A522, 294 (2004).

- [58] Hall A HRS. https://hallaweb.jlab.org/equipment/high_resol.html.
- [59] K. G. Fissum et al. Nucl. Instr. and Meth. A **474** (2001).
- [60] M. Iodice et al. Nucl. Instrum. Meth. A**411**, 223 (1998).
- [61] William R. Leo. Techniques for Nuclear and Particle Physics Experiments (Berlin: Springer) Second Revised Edition (1994).
- [62] M. Nycz. Measurement of the EMC effect of the tritium nucleus at Jefferson Lab, Ph.D. Thesis, Kent State University (2020).
- [63] S. Marrone et al. Performance of the Two Aerogel Cherenkov Counters of the JLab Hall A Hadron Spectrometer, Il Nuovo Cimento B, Vol. 124, issue01, 99-114.
- [64] V. Sulkosky. Data Acquisition for the Hall A High Resolution Spectrometers During 12 GeV (2014).
- [65] CODA. <https://coda.jlab.org/drupal/> .
- [66] EPICS. https://www.jlab.org/accel/documents/epics_doc2.html .
- [67] Hall A Analyzer. <https://redmine.jlab.org/projects/podd/wiki>.
- [68] N. Liyanage. Optics calibration of the Hall A high resolution spectrometers using the new optimizer. JLAB-TN-02-012 (2002).
- [69] J. E. Bane. The EMC Effect in A=3 Nuclei, Ph.D. Thesis, The University of Tennessee, Knoxville (2019).
- [70] T. Gogami et al. Phys. Rev C**94**, 021302(R) (2016).
- [71] C. Ciofi degli Atti and S. Simula. Phys. Rev. C**53**, (2016) 1689-1710.

- [72] A. Uzzle. Electroproduction of Kaons on Helium-3 and Helium-4, Ph.D. Thesis, Hampton University, (2002).
- [73] F. Dohrmann, A. Ahmidouch, C. S. Armstrong, J. Arrington, R. Asaturyan, and S. Avery et al. Phys. Rev. Lett. 93, 242501 (2004).
- [74] T. Nagae et al. Phys. Rev. Lett. Vol **80**, No. 8, (1998) 1605-1609.
- [75] G. Cowan et al. Eur. Phys. **J. C71**, 1554 (2011).

VITA

BISHNU DATT PANDEY

email: pandeybishnu25@gmail.com

Education

- Ph.D. (2021), Physics, Hampton University
- M.Sc. (2008), Physics, Tribhuvan University, Kathmandu, Nepal

Professional Experience

- Research Assistant (2014-2021) Hampton University, Hampton, VA
- Physics Lecturer (2008-2014) Higher Education Board of Nepal

Honors and Awards

- Departmental Fellow, full scholarship and stipend, (2014-2021) Hampton University physics Department, Hampton University, Hampton, VA.
- First Place, Oral Presentation, Association of Nepali Physicists in America (ANPA) 2019.

Selected Publications

1. H. Dai et al., Phys. Rev. C 98, 014617 (2018).
2. H. Dai et al., Phys. Rev. C 99, 054608 (2019).
3. M. Murphy et al., Phys. Rev. C 100, 054606 (2019)
4. S. N. Santiesteban et al., Nucl. Instrum. Methods Phys. Res., Sect. A 940, 351 (2019).

5. R. Cruz-Torres et al.(Jefferson Lab Hall A Tritium),Phys. Lett. B797, 134890 (2019), arXiv:1902.06358

Oral presentations

1. Kinematics Calculation on the Feasibility of a Λ -p Scattering Experiment Using Tagged Photon Beam at ELPH, Strangeness Nuclear Physics (SNP) School 2016, Tohoku University, Sendai, Japan, November 18-22, 2016.
2. Status Update on the New HMS Wire Chamber, Hall C Winter Collaboration Meeting, Jefferson Lab, Newport News, January 20-21, 2017.
3. Status Update on the New HMS Wire Chamber, Joint Hall A/C Summer Collaboration Meeting, Jefferson Lab, Newport News, June 22-23, 2017.
4. Determining the Unknown Λn Interaction by Investigating the Λnn Resonance, APS April Meeting, Columbus, Ohio, April 14-17, 2018.
5. Update on the E12-17-003 Experiment, 8th Workshop of the APS Topical Group on Hadronic Physics (GHP), Denver Co, April 10-12, 2019.
6. Update on the E12-17-003 Experiment, APS April Meeting Denver, CO, April 13-16, 2019.
7. Spectrometer Optics Calibration for the E12-17-003 Experiment, International Meeting on Virtual Photon Spectroscopy of Λ Hyper-nuclei, Kyoto University, Kyoto, Japan, May 22-24, 2019.
8. Update on the E12-17-003 Experiment, Hampton University Graduate Studies (HUGS) Summer School, May 28-June 14, 2019.
9. Update on the E12-17-003 Experiment, Jefferson Lab User group organization(JLUO), Jefferson Lab, June 25, 2019.

10. Update on the E12-17-003 Experiment, Hall A/C Summer Collaboration Meeting 2019, CEBAF Center Jefferson Lab, June 27-28, 2019.
11. Update on the E12-17-003 Experiment, Hall A Winter Collaboration Meeting Jefferson Lab, January 30-31, 2020.
12. Update on the E12-17-003 Experiment, Workshop on Electro and Photo Production of Hypernuclei 2020 at Nuclear Physics Institute of the CAS, Řež, Czech Republic, February 15-16, 2020.
13. Update on the E12-17-003 Experiment, Joint Halls A/C Summer Collaboration Meeting, Jefferson Lab, July 16-17, 2020.
14. Analysis updated on the E12-17-003 Experiment, APS (DNP) Meeting, Virtual Presentation, October 30, 2020.

Poster presentations

- (a) SNP school 2016, Tohoku University Japan. November 18-22, 2016.
- (b) 22nd Annual School of Science Research Symposium, Hampton University, April 11, 2016.
- (c) Jefferson Lab User group meeting, Jefferson Lab, June 18, 2018.
- (d) The 13th International Conference on Hypernuclear and Strange Particle Physics, Portsmouth, VA, June 24-29, 2018.
- (e) 24th Annual school of science research symposium, Hampton University, Hampton VA April 17, 2019.
- (f) 14th Annual JSA Virtual Graduate Student Poster Competition, Jefferson Lab (online presentation) on June 23, 2020